Progress in Materials Science 106 (2019) 100578

Contents lists available at ScienceDirect

Progress in Materials Science

journal homepage: www.elsevier.com/locate/pmatsci

3D printing of Aluminium alloys: Additive Manufacturing of Aluminium alloys using selective laser melting

Nesma T. Aboulkhair*, Marco Simonelli, Luke Parry, Ian Ashcroft, Christopher Tuck, Richard Hague

Centre for Additive Manufacturing, Faculty of Engineering, University of Nottingham, Nottingham NG8 1BB, United Kingdom

ARTICLE INFO

Keywords:
Additive manufacture
Aluminium alloys
Selective laser melting
Metallurgy
Heat treatments
Mechanical performance

ABSTRACT

Metal Additive Manufacturing (AM) processes, such as selective laser melting (SLM), enable the fabrication of arbitrary 3D-structures with unprecedented degrees of freedom. Research is rapidly progressing in this field, with promising results opening up a range of possible applications across both scientific and industrial sectors. Many sectors are now benefiting from fabricating complex structures using AM technologies to achieve the objectives of light-weighting, increased functionality, and part number reduction, among others. AM also lends potential in fulfilling demands for reducing the cost and design-to-manufacture time. Aluminium alloys are of the main material systems receiving attention in SLM research, being favoured in many high-value applications. However, processing them is challenging due to the difficulties associated with laser-melting aluminium where parts suffer various defects. A number of studies in recent years have developed approaches to remedy them and reported successful SLM of various Al-alloys and have gone on to explore its potential application in advanced componentry. This paper reports on recent advancements in this area and highlights some key topics requiring attention for further progression. It aims to develop a comprehensive understanding of the interrelation between the various aspects of the subject, as this is essential to demonstrate credibility for industrial needs.

Metal additive manufacturing technologies are developing at a rapid pace to cope with the current industrial needs to utilise the unmatched capabilities that these technologies have to offer. The acceleration in the amount of research undertaken worldwide in this field is remarkable. This review presents the reader with an overview of the metal additive manufacturing technologies that are now commercially-available and receiving attention from researchers and industrialists. The core of the article focusses on the recent advances in processing aluminium alloys using the powder-bed fusion technique selective laser melting, shedding the light on the various aspects of research involved and the challenges that face its uptake by the industry. The number of Al alloys that are now processable by selective laser melting with high fidelity is quite limited. Nevertheless, ongoing studies that aim to widen this range are increasing and the various types of defects and the methods devised to detect or remedy them are presented. Furthermore, the research carried out to characterise the defect-free fully dense parts fabricated by SLM is reviewed. This covers the metallurgy of the materials produced and the mechanical properties of the parts. The last section of this article provides an outlook to highlight the issues that require being addressed in the near future to achieve the utmost efficiency and effectiveness of the state-of-the-art technology.

* Corresponding author.
E-mail address: nesma.aboulkhair@nottingham.ac.uk (N.T. Aboulkhair).

https://doi.org/10.1016/j.pmatsci.2019.100578
Received 9 August 2018; Received in revised form 1 May 2019; Accepted 7 July 2019
Available online 10 July 2019

1. Introduction to additive manufacturing technologies

Additive Manufacturing (AM) processes are sometimes termed Layered Manufacturing in reference to the nature of the process, where a part is fabricated layer-by-layer from three-dimensional (3D) data. Industry is now benefiting from fabricating geometrically-complex structures using a range of available AM technologies. These processes have the potential to fulfil demands for reducing design-to-manufacture time through replacing a series of production processes by a single-step process (followed by a finishing step, as per the ASTM standard "*Removal of the support structure and cleaning may be necessary; however, in this context not considered as a separate process step*" [1]). This also realises the aim of manufacturers in shortening supply chains and lead times. Some AM techniques provide the advantage of potential savings on raw materials since it uses only the material needed to fabricate the part of interest, *i.e.* waste is minimized. It promotes the possibility of producing cost-effective customized products and hybrid materials, achieving properties otherwise unachievable [3]. As the credibility of AM increases, its impact is expected to affect businesses globally where AM parts are already widely used in various fields. Despite its advantages, it cannot be generalized that it would be suitable and/or feasible for businesses regardless of their needs and sizes without considering the complexity, customization, and production volume [4].

Depending on the specific AM approach to be investigated, there are distinct tiered advantages that, particularly, designers can exploit through either the evolutionary design of existing products, or revolutionary approaches, which impart functionality not achievable with conventional manufacturing techniques. With design freedom being the primary rationale for AM implementation, AM offers the capability to drastically improve the efficiency and functionality of existing designs, and the ability to incorporate complexity that is broadly insensitive to cost [5]. This includes the ability to offer design features not achievable conventionally, such as: embedding complex internal structures or channels into designs [6] (such as lattices [7]); enabling light-weighting through topology optimisation [8] and ultimately, the production of multimaterial, multifunctional devices [9]. Another advantage is combining components within assemblies; enabling reduction in the dependency on mechanical fixtures and additional production operations.

The focus of this review article is on selective laser melting, which is one of the metal AM techniques. Metallic AM systems can be classed as: (a) powder-bed fusion, (b) direct energy deposition (DED), and (c) droplet-on-demand systems. Powder-bed fusion (PBF) [1] technologies, such as selective laser melting (SLM) and electron beam melting (EBM), are currently receiving significant attention from both the academic and industrial sectors. These are processes with which complex structures can be fabricated from loose metal powder adopting the powder-bed approach for raw material feed. SLM and EBM are used to fabricate parts with unmatched degrees of freedom from loose powder through full melting [10] and metallurgical joining of individual scan tracks. The levels of achievable complexity are significant; examples include – but are not limited to – complex light-weighting structures (lattice structures either strut- or triply periodic minimal surface TPMS-based) [11] and functionally-graded materials [12]. The parts fabricated by SLM and EBM currently have applications in numerous industrial sectors, such as biomedical (e.g. implants, dental crowns, and tissue engineering scaffolds), aerospace, automotive, nuclear, chemical, and petrochemical [13].

The principle operational sequence in EBM and SLM are similar, where a high energy source is used to melt the pre-laid material selectively. In EBM a high-power electron beam is deployed as the heat source, rather than the laser beam used in SLM. EBM is conducted under high vacuum environments at high temperatures [14], whereas SLM tends to operate in a process chamber flushed with an inert gas at room temperature. Processing under high vacuum means that the process has a cleaner environment and EBM tends to offer advantages in the processing of reactive materials [15].

Direct energy deposition processes use a high energy heat source to melt a feedstock material, either in powder or wire form, as it is being deposited. Similar to the PBF techniques, in DED a 3D part is made from rapidly-solidifying tracks. DED systems can only fabricate near-net-shape parts from scratch on flat substrates or add features to existing parts [16–18]. DED facilitates *in-situ* alloying of various alloys and composites [19] and modifying the chemical composition of an alloy "on-demand" during processing [20]. They are preferred for the production of functionally-graded materials with controlled microstructures, as they have the capability of depositing more than one material in one part. This, however, poses difficulties when recycling the mixed materials. This is a lot more challenging when using PBF, for reasons that will be discussed in Section 4. SLM, however, produces a more homogenous microstructure with smoother surfaces [20].

In the PBF systems, the heat source is moveable in the XY plane whereas the substrate is responsible for motion in the Z-axis. DED systems, in contrast, offer the flexibility to move the deposition head, the substrate, or both simultaneously, with the capability of using robotic arms to extend the degrees of motion to 5 axes.

PBF systems are generally considered as single material per layer AM systems. Other AM approaches to producing metallic parts from multiple materials, concurrently, with high levels of accuracy include droplet-on-demand (DOD) technologies. DOD of pure metals is constrained to low temperature metals because metals solidify at room temperature making them hard to process in this fashion. They promise low wastage as they dispense minute amounts of materials [21]. A typical DOD system consists of a molten metal reservoir and a type of actuation to force the metal out of a nozzle in the form of droplets, such as pneumatic actuators [22], piezo-electric actuators [23], and electromagnetic actuators [24]. Another DOD approach that deposits patterns from micron-sized droplets is Laser Induced Forward Transfer (LIFT) [25], which can process a range of materials including Cr, Au, Ni, W, and Al [26]. However, SLM is the predominant industrially deployed process and is thus the subject of this review.

2. Selective laser melting (SLM)

The basic components of an SLM system are schematically presented in Fig. 1. The process involves a series of steps including powder deposition and laser scanning [16]. It is conducted within an inert controlled-atmosphere chamber of choice to avoid oxidation during processing, *i.e.* melting and solidification [15].

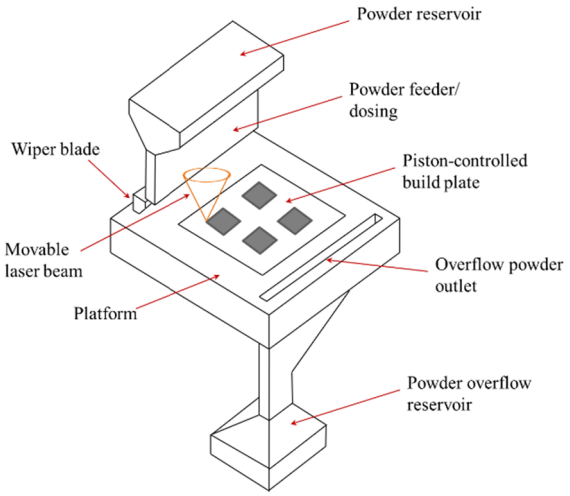

Fig. 1. Simplified schematic presentation of a powder-bed fusion system (selective laser melting).

The SLM operational sequence can be broken down into the following main steps:

I. A 3D computer-aided-design (CAD) model is converted into (normally) an STL file.
II. It is orientated to the optimum build orientation (depending on the height in the Z-axis, the surface finish, and minimisation of the support structures).
III. The support structures are generated, including all the iterations for minimal supports
IV. The file is sliced into layers of equal thickness and transferred to the machine.
V. A build-plate is usually heated to aid in heat dissipation by lowering the thermal gradient [27] to avoid part curling due to non-uniform thermal expansion [28].
VI. A layer of powder of a predefined thickness is spread onto the build-plate.
VII. A focused laser beam is fired onto the layer, moving in the x-y plane to selectively scan and melt the regions of interest.
VIII. The build-plate is then lowered a distance equal to the layer thickness to allow for the deposition of another layer.

Repeating the sequence from VI to VIII fabricates the part layer-by-layer. The time consumed for a build is divided into primary and auxiliary times. The former is that needed to scan the powder, which is process-parameter-dependent, whereas the latter is that required for build-plate lowering and powder deposition [29,30], which is more commonly referred to as “recoating”.

2.1. Points of focus in SLM

In principle, the SLM process appears relatively straightforward. However, there are many aspects which require attention in order to manufacture parts of sufficient structural integrity to enable industrial adoption. These aspects, namely: (i) process-, (ii) design-, and (iii) material-related, will be discussed in the following section.

2.1.1. Process-related

The SLM process can be divided into the three distinct stages shown in Fig. 2. A part is made up of a stack of layers overlapping vertically, *i.e.* along the build direction; each layer is composed of a stack of individual scan tracks overlapping horizontally. These are the primary building blocks of SLM parts; their formation and overlap are governed by a set of process parameters. The number of these parameters is ambiguous [31]; the most influential ones can be found in Fig. 3.

“Material Qualification and Certification Research” [30,33] is essential for a material to be declared as processable by SLM. This is

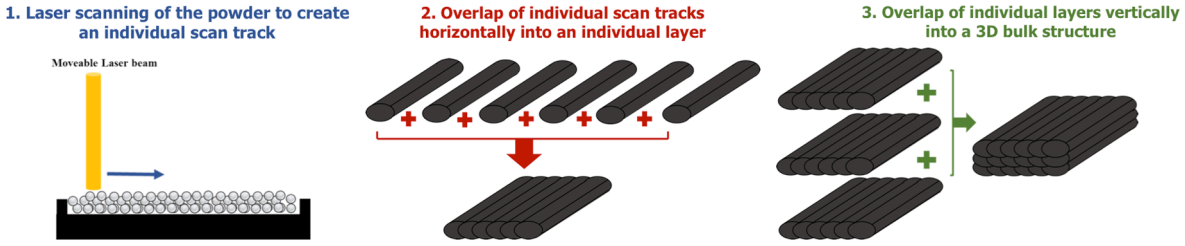

Fig. 2. Schematic presentation showing the operational sequence in SLM demonstrating the overlap of the scan tracks building up a part additively.

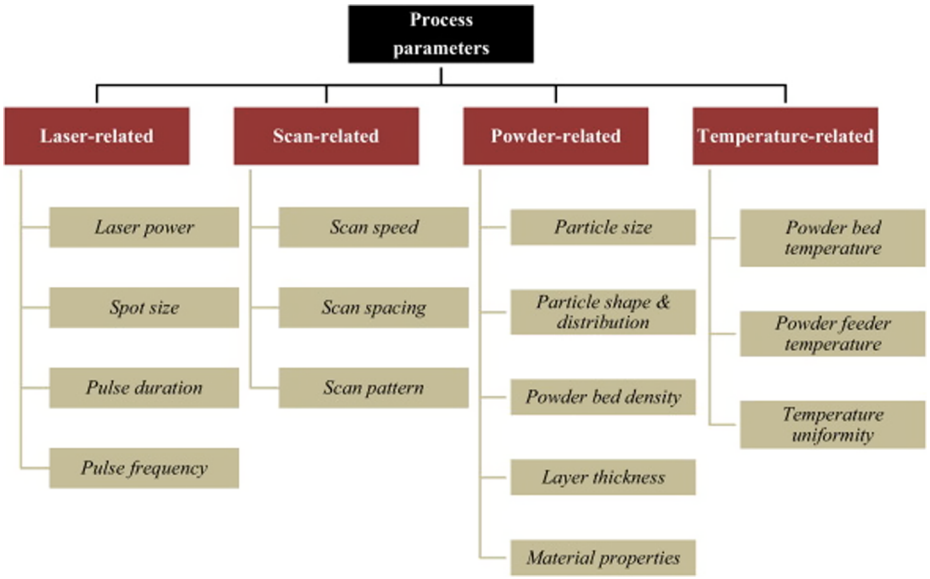

Fig. 3. The most influential process parameters affecting the quality of a part processed by SLM [32].

the practise of conducting parametric studies to optimize the parameters to produce defect-free, fully-dense parts. An inapt combination of parameters leads to defect formation [34,35]. Optimized parameters vary from one machine to another and between materials. The parameters given most attention in the literature are the laser beam and its properties, in terms of, laser power and spot size, hatch spacing, scan speed (defined by the point distance and exposure time), layer thickness, and scan strategy. These parameters are illustrated in Fig. 4.

The laser power controls the amount of energy delivered to the irradiated material. Highly-reflective materials (such as Al alloys [32]) require high power to completely melt [29], otherwise partial melting will lead to incomplete filling of the melt pool space upon solidification, thus introducing defects. In addition to its role in the melting efficiency, the laser power governs the size and continuity of a scan track [35], affecting the structural integrity of the parts.

The hatch spacing should provide an amount of overlap between adjacent tracks for the part to be built through their metallurgical bonding [36]. Too much overlap increases the fabrication time by increasing the primary time. Large hatch spacings impose limitations on the maximum layer thickness [37], *i.e.* increasing the auxiliary time and gaps start to form due to the lack of intra-layer bonding [32]. Similar to the laser power, the scan speed controls the melting and solidification rates. The slower the speed, the longer the irradiated spot is maintained in a molten state, taking longer to solidify and affecting the microstructure as well as controlling the track size.

The layer thickness should be large enough for the part to be manufactured cumulatively. However, larger thicknesses introduce defects [38], such as balling, an inability to adhere to the dimensional accuracy and tolerance, as well as incomplete melting, thus depressing the structural integrity and properties of the part [39].

The scan pattern defines the laser path within a layer; examples of common patterns are unidirectional, meander, and checkerboard [40] (Fig. 4b–d). The scan strategy defines the difference in scan patterns between layers (Fig. 4e), *e.g.* rotating the orientation between layers by a set angle or scanning a layer multiple times. Patterns and strategies are often used to minimise defects and control the microstructure.

One of the metrics commonly used to optimize process parameters is that of *energy density*. This is calculated based on a linear, areal, or a volumetric approach with the volumetric being the most commonly used in the literature. The linear energy density (ED_l, J/mm) is calculated using the formula:

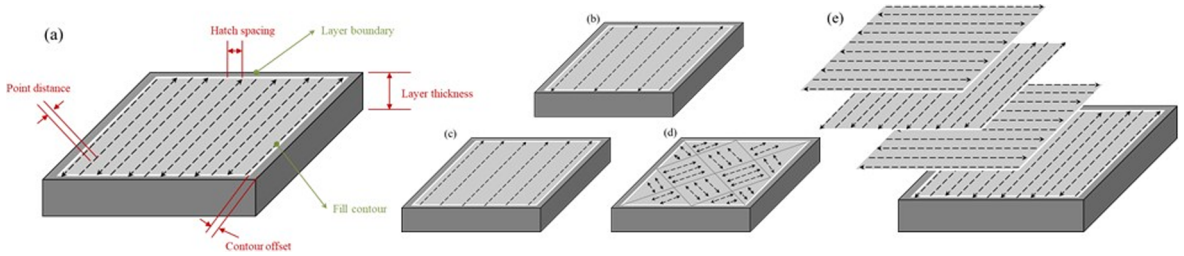

Fig. 4. The geometrical parameters in the SLM process are shown in (a). Examples for the different scan patterns (b) meander, (c) uni-directional, and (d) checkerboard. A schematic presentation for rotating the scan orientation per layer is in (e).

$$ED_l = \frac{P}{v}$$

where P is the laser power (W) and v is the scan speed (mm/s). The areal energy density (ED_a, J/mm^2) further incorporates the hatch spacing (h, mm) in the formula, as follows:

$$ED_a = \frac{P}{v\ h}$$

The most commonly used form of energy density in the literature is the volumetric energy density (ED_v, J/mm^3), which is calculated as follows:

$$ED_v = \frac{P}{v\ h\ t}$$

Where t is the layer thickness (mm). As evident in the formula, the same energy density can be achieved using various combinations of parameters. Some studies in the literature use the laser beam diameter instead of the hatch spacing in this formula [31]. An experimental approach for SLM cooling rates determination proved that the energy density formula is indeed not accurate to reflect the process [41]. Thomas et al. [42] used normalised process diagrams instead of using the energy density values to map the evolution of defects and microstructure of a material with the process parameters. Their formula for normalised ED (ED*) considers both the process parameters and the material properties:

$$ED^* = \left(\frac{AP}{2\ v\ t\ r}\right) * \left(\frac{1}{0.67\rho C_p (T_m - T_0)}\right) * \left(\frac{1}{h^*}\right)$$

where A is the material's absorptivity, r is the laser beam radius, ρ is the material's density, C_p is its specific heat capacity, T_m is the melting point, T_0 is the initial temperature of the powder-bed, and h^* is the dimensionless hatch spacing derived from (h/r). One of the limitations in this formula is the lack of data on the absorptivity of powder materials, which forces researchers to use absorptivity values from the literature, normally measured for polished clean metal plates or rough oxidised surfaces. The absorptivity of a material changes with the process parameters employed during SLM [43]. Matthews et al. [44] investigated the correlation between the process parameters (speed and power) and the absorptivity within the melt pool. The absorptivity of Al was slightly higher than the values in the literature, possibly due to the material's reactivity and the presence of oxides in the melt pools. Furthermore, there was a steep increase in effective absorptivity with the scan speed at high laser powers ($>$ 200 W).

Despite the extensive amount of research optimising the process parameters based mainly on the energy density, it is clear that none of these formulae can reflect the effective energy delivered to the material during processing. For example, these formulas do not consider the scan patterns and hatch styles, the gas flow rate and direction within the process chamber, the scan offset at the corners and boundaries, and the number of times a layer is scanned, if multiple scans are applied. Also, given that each parameter affects the quality of the individual scan tracks, or the bulk structure in general, in its own way, it is difficult to relate the quality of the part to the energy density. Bertoli et al. [31] reported variations in the widths and heights of single tracks fabricated using a range of combinations of speed and powder despite preserving the same energy density. This was further supported by Prashanth et al. [45] who provided experimental evidence for the lack of reliability of using the energy density as a design parameter in SLM by fabricating samples using a range of various laser powers and scan speeds, maintaining the same energy density, showing the different levels of density and mechanical properties produced at each combination of parameters. Bertoli et al. [31] also asserted that the volumetric energy density is a thermodynamic quantity, which is unable to capture the physical phenomena taking place during the process (Marangoni flow, recoil pressure, hydrodynamic instabilities, …, etc.). These factors control the shape of each track and therefore not being captured in the energy density formula retracts from its reliability.

2.1.2. Design-related

In order to fully exploit the design freedoms available in AM, automated design tools are required to assist the designer in creating efficient structures. Fundamentally, this requires a design process involving simulation within an optimisation loop. The families of optimisation techniques employed in engineering applications (in increasing complexity) include: size, shape, and topology optimisation.

Topology optimisation (TO) enables the generation of complex structures not intuitive to the designer. TO defines a process to obtain the most efficient distribution of material within a prescribed volume to maximise a functional performance subject to given constraints, such as the example in Fig. 5. It is prevalent in many physical disciplines, including but not limited to structural, thermal, fluids, acoustics, and electromagnetics [46]. Topology optimisation is a feature of simulation-based design and therefore fundamentally requires the ability to model the governing physics in the underlying application. In theory, solutions from TO are readily manufacturable by SLM. In practice, a variety of further design iterations are required, such as surface smoothing and re-modelling [46–50], post-analysis, and subsequent re-designs which may be needed to account for manufacturing constraints [51,52]. This remains a laborious manual operation, and at present no techniques have been reported to fully automate this procedure. A good overview of the techniques used in TO algorithms can be found in [46].

SLM enables the incorporation of multi-scale hierarchical structures within a part, by the inclusion of lattice structures (examples are presented in Fig. 6) and potentially controlling the microstructure to the advantage of design [54]. A lattice structure consists of a tessellation of a unit cell throughout a specific volume within a part. Lattices are generally difficult to construct using standard

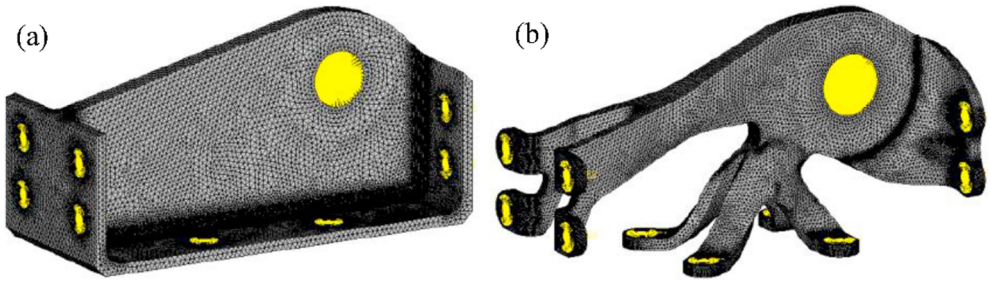

Fig. 5. A demonstration for light-weighting achievable through topology optimisation where a model for the original part to be manufactured by conventional methods is show in (a) and the optimised model to be fabricated by SLM is shown in (b) [53].

available CAD packages and is usually undertaken with dedicated design packages such as Materialise 3-matic [55] and Autodesk Netfabb [56].

The desire to use lattice structures is driven by two motivators: (1) their wide range of applications, including structural light-weighting [12,57–61], impact protection [62,63], thermal management [64], bone implants [65–68], and vibration damping [69–72], (2) the prospect of achieving effective material properties (density, Young's modulus, strength, and thermal conductivity) superior to conventional solids [73]. Significant effort has been directed at determining the density-property relationships required to enable the design of lattice structures with pre-defined performance [12,57,58,67,74–78].

Manufacturing constraints are still resident in SLM, although to a lesser degree compared to traditional manufacturing techniques. These do not necessarily restrict the design but must be considered at some point in the design process [52]. Design for Additive Manufacturing (DFAM) [79–81] is the conscious effort to optimise a multi-variate objective problem (cost, part quality, design performance, production time) whilst accounting for the manufacturing constraints inherent within SLM. These must also consider manufacturing operations downstream, including post-processing, part qualification, and final assembly. Additionally, the designer must specifically have knowledge of the target SLM system and material because designs remain sensitive to their process-ability.

One of the most pertinent issues with design for SLM is the requirement for sacrificial support material to provide mechanical fixturing for the part as it is being built. They are required for large overhang regions – downward facing surfaces or unconnected regions [82]. Critically, they also provide the predominant mitigation strategy against part distortion during manufacture due to the effects of residual stresses caused by the large temperature gradients encountered in the process. This requirement places restrictions on the inclusion and placement of features such as holes and internal channels in design for SLM. Support structures also increase the costs of manufacture due to:

- The manual pre-processing time required for adding supports to design
- The additional time to manufacture support structures
- Post-processing: support removal and surface polishing to remove artefacts
- Irrecoverable material waste from an SLM viewpoint but it can be scrapped and re-melted for other uses

Ideally parts should be adjusted to become self-supporting [82–85]. However, optimising solely towards reducing the use of support structures can impose undesirable penalties on the part's functional performance [86]. Therefore, careful consideration should be taken by the designer to balance the cost of support material and the overall implications on the design.

Designs must also consider the implications of the orientation of the part in the machine as this may affect factors, such as the production time, the support structure requirements, residual stresses, surface roughness, microstructure, and the effects of build anisotropy.

In summary, exploiting the freedoms available in SLM remains a challenging endeavour for the designer, who must at some point account for the various manufacturing constraints. Future research on incorporating SLM manufacturing constraints will help reduce

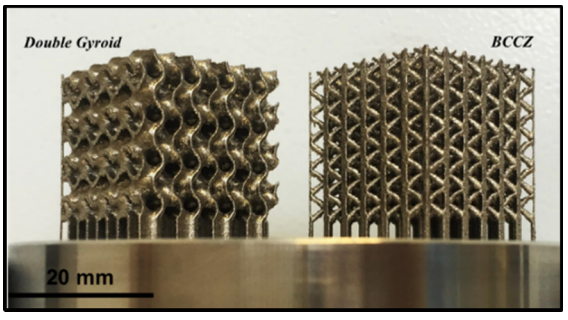

Fig. 6. A double gyroid lattice (TMPS) and a BCCZ lattice (strut-based) fabricated using a Realizer SLM-50 in the Centre for Additive Manufacturing at the University of Nottingham.

the manual intervention required by the designer to minimise the support structure requirements and choose the best orientation to improve part quality and minimise the effects of residual stress. The ability to utilise multi-scale topology optimisation will enable future designs to exploit the multi-scale capabilities of AM to both improve performance and potentially offer multi-functional capability to designs.

2.1.3. Material-related

SLM utilises powder feedstock. To date, the feedstock has mostly been alloys that are commercially-available in powder form and the materials currently known to be reliably processable by SLM are still somewhat limited. For industrial relevance, the focus has mainly been on aluminium alloys [32,86–89], nickel alloys [90–93], steels [35,94–96], and titanium alloys [11,97–99] with some cobalt alloys [100–103], copper alloys [104], magnesium alloys [105], and pure metals receiving some attention [106–110], among others.

Further, the attention has been largely restricted to alloys already serving in industrial applications. An understanding of the basis for material selection when it comes to manufacturing by SLM is still missing. For instance, most of the alloys that are currently undergoing investigation for process-ability by SLM have originally been designed and tailored to suit other manufacturing routes, such as casting.

Currently, the indicators researchers use to assess the process-ability of an alloy by SLM are cast-ability and weld-ability, due to the similarities in the processing conditions. However, there are also significant differences between these processes, for example, the solidification rates associated with SLM are much steeper than those associated with casting. The form of the starting material varies between SLM and welding, as the former uses metal powders instead of bulk or wires that have differing laser absorption behaviours. Furthermore, the repetitive melting and solidification experienced in the material during re-scanning/re-melting in SLM are significantly different to the experiences the same material would face during laser welding. Therefore, it is critical to establish a comprehensive understanding of the particular process needs in order to develop new alloy systems that are well-suited for the process in terms of the desirable physical and chemical properties for processing whilst fulfilling the application requirements.

Martin et al. [111] presented research using the well-known CALPHAD method (Thermo-Calc software [112]) to engineer alloys with controlled solidification. Their approach was to define nano-particles of lattice-matched elements that can electrostatically adhere to pre-alloyed powders to control the material's solidification during processing. Computational methods for alloy design are developing rapidly and proving very beneficial in designing new materials [113]. Another more recent computational method (The Material Project [114] was described in [114], which utilises high-throughput computation to reveal the properties of inorganic materials. It is expected that computational methods will be increasingly used to develop new alloy systems for AM processes in the future. Further discussion of alloy design for SLM can be found in Section 4.

2.2. Inside a selectively laser melted part

During SLM, the irradiated powder melts, creating dynamic melt pools. The stability of these melt pools are affected by the process parameters [104,115] where the laser power and scan speed affect the width and depth of a melt pool, whereas the track's length is governed by the laser power and material's absorptivity [35].

Upon laser irradiation, several phenomena take place, including laser absorption and scattering, heat transfer, phase transformation, chemical reactions, fluid dynamics, and evaporation and emission of material [104]. Solidification of a metal is controlled by its ability to conduct the latent heat away from the solid/liquid interface [116]. When the laser beam impinges on the target material, the material's reflectivity and conductivity dictate the amounts of energy that will be reflected and transmitted. As the energy is transmitted into the material, it's intensity decays, with the rate of decay being governed by the material's absorption coefficient [117].

When a laser beam is directed at a block of metal, depending on the melting mode (conduction or keyhole) a cavity can be created by ablation and plasma formation, which is surrounded by the molten material [118]. The molten material applies forces on the cavity, driven by the surface tension and hydrostatic pressures. As the laser beam proceeds on its assigned path, the material flows into the cavity and solidifies in the characteristic chevron pattern in Fig. 7(a). The cross-sectional view of a scan track is shown in Fig. 7(b). At high scan speeds, fast solidification can occur without completely filling the cavity, leaving a void. A 3D bulk structure is formed during SLM through the overlap and metallurgical bonding of these melt pools.

A material processed by SLM experiences cooling rates of $\sim 10^5$–10^6 K/s [119], solidifying in microstructures that are characteristically different from those achieved via conventional processing with lower cooling rates. The main difference between SLM materials and those conventionally-processed is in the scale of the grain structure. Conventional processing typically yields coarse microstructures, whereas SLM produces substantially finer microstructures [120]; however, this will also depend on the material being processed, based on the response of its constituent elements to laser irradiation.

The mechanical properties of SLM parts can be investigated from two perspectives. The first is the structural integrity where SLM parts can suffer from high residual stresses [121], pores [32], cracks [122], inclusions (e.g. entrapped laser spatter) [123], and surface irregularities [123], among others defects. The presence of such defects can significantly worsen the mechanical performance and a combination of material qualification and post-processing treatments are often needed to remedy such defects, enabling the production of fully-dense defect-free parts.

The second perspective is the metallurgy where the finer microstructures developed in SLM materials can enhance certain mechanical properties for various materials systems [124]. SLM parts can also exhibit anisotropic mechanical behaviour, based on the build orientation and scan strategy used [119]. These aspects will be discussed in the following sections, with a focus on Al alloys.

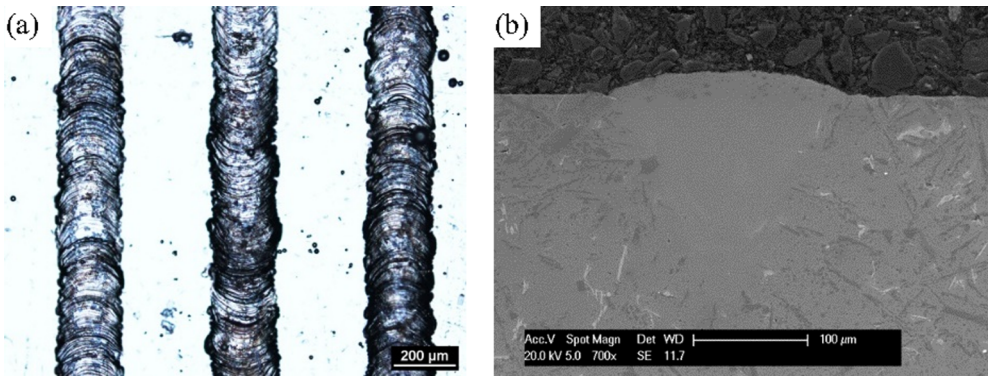

Fig. 7. (a) Characteristic chevron pattern on top of an AlSi10Mg single track processed by SLM on an LM6 as-cast substrate and (b) cross-sectional view of a single melt pool showing evidence of keyhole-mode melting (own work).

3. Aluminium alloys and SLM opportunities

Al alloys are used in a wide range of industries. They offer a good compromise between strength and density, in addition to being relatively inexpensive; positioning themselves to be used in applications where performance and light-weighting are needed concurrently. The family of Al alloys can be classified according to the form and main alloying element, as shown in the map in Fig. 8.

AM Al parts are now being used in consumer, aerospace, and automotive products [129]. SLM can fabricate bulk and open-cell structures. Porous or cellular Al is a light-weight metal with good deformability, hence, it is a strong candidate for crumple zones in automobiles [130]. SLM of Al is also beneficial for hard-to-machine or form Al alloys. For instance, the AA-6xxx series contains a large amount of hard intermetallics that make forming it challenging [131].

Another advantage for SLM processing Al (cast alloys, especially) is the microstructural enhancement. Cast alloys are traditionally strengthened through refining their microstructures during casting by adding chemical modifiers. The high cooling rates associated with SLM lead to microstructural refinement during manufacture [132] without altering the chemical composition - this will be further reviewed in Section 6. As such, SLM processing of castable Al alloys can fulfil the demand for the fabrication of complex structures with refined microstructures.

4. Selective laser melting of aluminium alloys

Al alloys are regarded as challenging when it comes to processing by SLM. Al powders are inherently light-weight, have high reflectivity, high thermal conductivity, and low laser absorptivity in the range of wavelengths (1.06 μm [133]) of the fibre lasers (continuous or modulated) conventionally used in SLM. For detailed descriptions of these challenges, the reader is referred to [134]. The alloys that have returned promising results in terms of process-ability by SLM are generally the cast alloys [88], with AlSi10Mg receiving most attention followed by AlSi12. This is owing to their good cast-ability, alongside low shrinkage due to the large fraction of Al-Si eutectic. Although the Al-Si alloys are beneficial, their tensile strength is modest and their ductility is low ($\sim$4%).

Al alloys widely used in the aerospace and automotive industries include the high strength 2xxx, 5xxx, 6xxx, and 7xxx series, which also offer higher ductility. However, these are still struggling to find their way to being declared as successfully processable by SLM. Given the steep cooling rates associated with the process, these alloys tend to micro-crack during SLM processing, resulting in parts with poor structural integrity [135].

4.1. The feedstock

4.1.1. Pre-alloyed powders

The use of traditional pre-alloyed powder has received most attention from researchers using SLM to process Al; possibly because they are readily available for other manufacturing processes. Further, most of the ongoing research has the objective of using SLM to fabricate a part that is currently being conventionally-made without changing the material. Examples of the commercially-available alloy powders that have been processed by SLM are presented in Table 1. This table also classifies the points of focus for each listed alloy. The amount of work undertaken on AlSi10Mg and AlSi12 massively surpasses that for all other alloys. This is driven by the success in processing these alloys as well as their common use in various industrial sectors.

The development of new bespoke alloys tailored for SLM is also of significant current interest. The Airbus group developed a new Al-Mg-Sc alloy (SCALMALLOY®RP) specifically designed for AM. It is characterized by high corrosion resistance, high specific strength, and exceptional fatigue and toughness properties [136]. The addition of Sc and Zr to the Al-Mg alloy to develop new compositions, such as Addalloy™ [137], refined the microstructure and strengthened the material [138]. Further, Sc improved the weld-ability, reducing the chance of hot cracking [139].

Powder specifications for SLM are considered from the process requirements [200]. The powder should have a spherical morphology to cope with the need for successive deposition of uniform powder layers. This morphology is essential to enhance the flow-

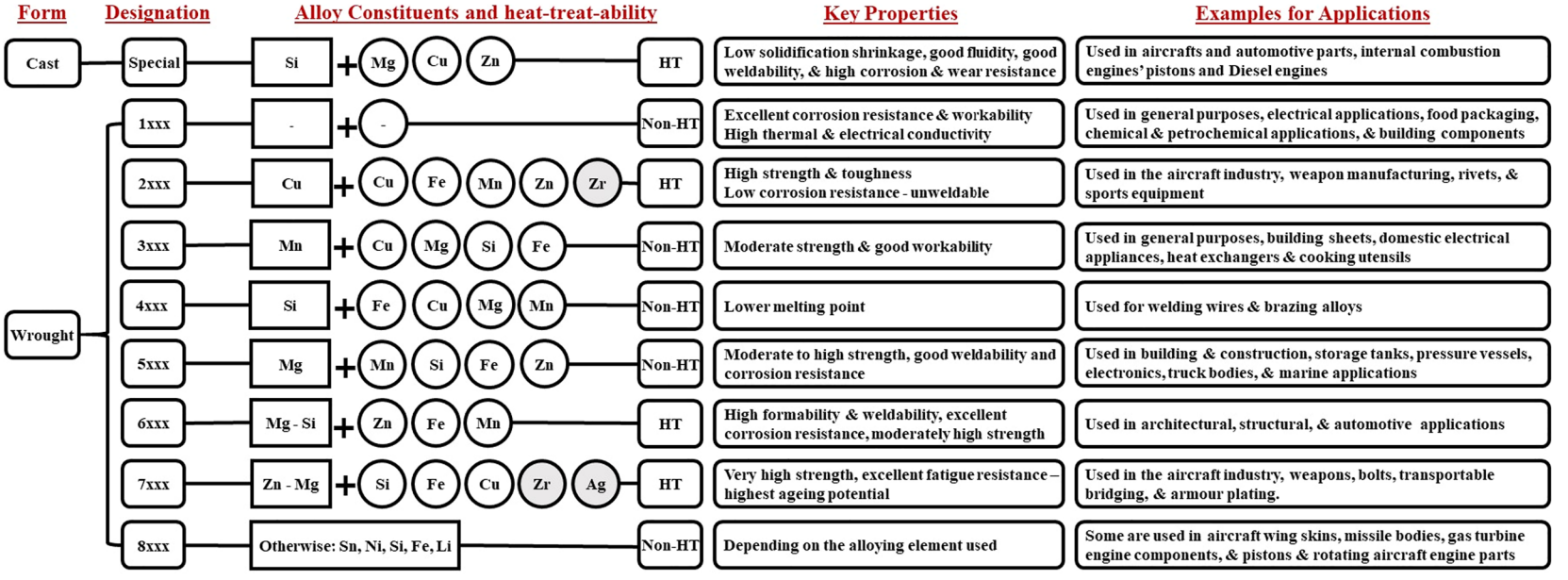

Notes:

- In the alloy designation, the 1st digit denotes the alloy group, the 2nd digit denotes the purity or modifications with the original composition numbered 0 and the modified versions take the numbers 1-9. The 3rd & 4th digits are only meaningful in the case of the 1xxx series as they denote purity but for the rest they only specify a certain alloy.
- Elements greyed out are optional in the alloy's composition.
- Heat treatable alloys can also carry the suffix T followed by a number from 0 to 9 in their designation denoting the heat treatment procedure used.
- There is no widely accepted designation system for cast allows, therefore they are sometimes given special designations depending on the alloying elements and their contents such as AlSi12 and AlSi10Mg, … etc.
- The American system uses different designations for Al alloys in the form of Nxx.x where N changes between 1 and 9 denoting the alloy group based on the main alloying element (1:Al, 2:Cu, 3: Si with Cu or Mg, 4: Si, 5: Mg, 6: unused, 7: Zn, 8: Sn, 9: other), the following two digits define the minimum Al content in the alloy, and the last digit (after the decimal point) indicates the form, i.e. whether this is a cast or ingot.
- The British system uses different designation in the form of LMx with no specific sequence for naming the alloys.

Fig. 8. Classification of Al alloys. The information in this map was collected from these references [125–128].

Table 1
List of conventional Al alloys processed by SLM in the literature with the corresponding references for each point of focus.

Al Alloy	Parametric studies	Defects & remedies	Metallurgy	Mechanical performance
AA-2024			[140]	
AA 2219	[115]			[141]
AA 2618	[115]		[142,143]	[143]
AA-4047			[144]	[144]
AA-6061	[145]	[146]	[146–150]	
AA-7075		[122]	[122,149]	[122,149,150]
AlSi7Mg, A356, A357	[151]	[152]	[148,151,153,154]	[151,152]
AlSi10Mg	[32,34,87,155]	[28,156–161]	[38,40,120,124,162–169]	[12,38,87,120,123,124,162,163,165–167,169–174]
AlSi12	[175,176]	[177]	[175,176,178–180]	[176,178–186]
AlSi20				[187]
AlSi50			[188]	
Al-20Si-5Fe-3Cu			[189]	
Al-Zn-Mg-Cu			[190]	[190]
Al-Cu-Mg	[191]		[191]	[191]
$Al_{85}Nd_8Ni_5Co_2$			[192]	[192]
ScalmalloyRP, Sc- and Zr-modified alloys	[138,139,193–195]	[193–195]	[137,139,193–199]	[138,139,193–199]

ability and packing density [201,202]. Gas phases in the starting powder considerably suppress densification [203,204]. These can be either on the surface from moisture that contributes to hydrogen porosity formation [159] or internal gas pores that are entrapped during the powder production process. Pre-heating the powder before processing to improve its absorptivity [205] is also recommended.

The metal powders used in SLM are either gas- or plasma-atomised with the former being more common [206]. Powders from the same alloy can also have dissimilar morphological properties based on the producer of the powders, as demonstrated in Fig. 9. It can be seen that powder A is irregularly shaped with more elongated particles whereas powder B is spherical. Using the same process parameters, relative densities of parts from A and B were 97.74% and 99.62%, respectively [207], demonstrating the importance of optimising the morphology of the powder prior to processing. However, it is also worth noting that the density of parts from powder A was also improved by altering the parameters, *i.e.* using more energy.

The National Institute of Standards and Technology (NIST) has developed a series of reports on materials standards for AM with the ASTM and ISO committees [206]. Standardized AM powder properties along with standardized methods of testing and evaluation should minimize the variability of produced parts.

4.1.2. In-situ alloying

In-situ alloying is a promising route to produce novel alloy compositions for both SLM process-ability and the properties of the parts. Coating Al alloys or mixing with elements that would enhance their absorptivity or surface tension, for instance, could be a means for better material process-ability. Depositing Cu on Al particles yields particles with intermediate absorptivity and reflectance compared to the original elements [208].

In-situ alloying has the potential to reshape the perception of the SLM process as it could dramatically expand the material palette for the technology. For example, the ability to *in-situ* alloy elemental powders offers the flexibility of having a stock of elemental powder “ingredients” and “cooking” the target alloy recipe through a design compromise between the process requirements and the properties necessary for the part in application. In order to validate this concept, researchers are currently investigating the

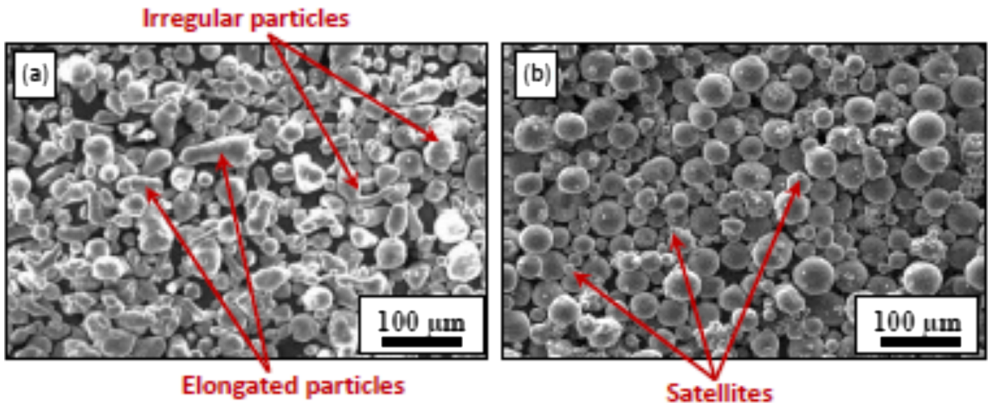

Fig. 9. Variation in morphology of AlSi10Mg powder based on the supplier: powder (A) from supplier 1 and powder (B) from supplier 2 [207].

production of compositions similar to the commercially-available alloys via *in-situ* alloying of the elemental powders making up the alloy's composition. Kang et al. [178] produced the hyper-eutectic alloy AlSi50 from pure Al and pure Si powders using a tumbling mixer; the content of each phase was affected by the process parameters.

One of the challenges in designing alloys this way is understanding how different the materials respond to laser irradiation during processing – individually and combined with others – as this is essential to enable the prediction of the properties and behaviour of the resultant material. Grigoriev et al. [2] processed Ti, Al, and Nb mixed in a turbula mixer to produce Ti_2AlNb parts with a somewhat homogeneous elemental distribution; however some non-fully-molten Nb particles were also distributed in an inhomogeneous manner. This inhomogeneity could be attributed to the high melting point of Nb (2469 °C) compared to that of Ti (1668 °C) and Al (660 °C), where Nb segregates will need higher energy density to melt. However, this highlights one of the challenges with such an alloying approach within SLM as using a higher ED can encourage the evaporation of some of the other elements leading to the entrapment of gas bubbles in the parts, thus depressing their structural quality. Elements' evaporation also means that the final composition will deviate from the target composition in the original design of the alloy. Furthermore, loss of elements can occur via reduction reactions as was reported in the case of SLM of an Al_2O_3/AlSi10Mg [209]. Therefore, this area of the research requires more considered investigation to optimize both material and process parameters to reach a suitable compromise.

Another advantage for *in-situ* alloying is the possibility of tweaking the composition of a commercially-available alloy by adding certain additives motivated by various driving forces. Bartkowiak et al. [210] refined the microstructure of Al by adding traces of Zn and Cu. Xi et al. [180] eliminated the crystallographic texture in AlSi12 by adding TiB_2 particles. Kang et al. [183] used a tumbling mixer to produce AlSi18 from AlSi12 and pure Si powders. Wang et al. [211] used a drum hoop mixer to produce a range of Al-xCu alloys in-situ, starting with Al4.5Cu and adding increments of Cu, increasing the materials compressive strength at the expense of its ductility. They observed segregations of Cu particles, which was not the case when the same composition was processed from pre-alloyed powder [41]. Sistiaga et al. [122] modified the composition of AA-7075 by adding traces of Si; successfully reducing cracking. Similarly, Martin et al. [111] added nano-sized Zr nucleants to AA-7075 and AA-6061 to control the solidification process and prevent micro-cracking. Following the same approach, Zhou et al. [199] added 1% Sc and Zr to an Al-Zn-Mg alloy to eliminate cracking.

SLM has also been used for the *in-situ* production of reinforced Al-based metal matrix composites (MMC) [212,213] with reinforcements distributed in the material in a way that produces properties surpassing the conventionally-processed composites [214–219]. Gu et al. [215,216] produced novel Al-based composites from AlSi10Mg and SiC with multiple reinforcements, yielding enhanced mechanical properties. Zhao et al. [169] showed that three types of reinforcements form in SiC/AlSi10Mg composites, namely, unmelted SiC, Al4SiC4, and the eutectic Si phase. As a result, spatial variation in the mechanical properties was observed. TiC reinforced Al-Si-Mg based nano-composite has been *in-situ* alloyed from mechanically-alloyed AlSi10Mg and TiC [218]. In another study, Gu et al. [219] fabricated a TiC reinforced composite from mechanically-alloyed Ti, Al, and graphite. More recently, Ma et al. [220] produced a diamond/AlSi12 composite characterisation by high performance and a good bond between the matrix and the reinforcing material. However, producing fully dense parts is still challenging and require more research efforts. These present SLM as a promising route to tailor the parts' properties at the microstructure level by producing specific custom metallurgies from the same constituent materials.

Wang et al. [221] added Carbon Nano Tubes (CNT) to AlSi10Mg via ball milling and processed the composite by SLM. However, it was not possible to identify the presence of Al carbides in the material using x-ray diffraction, which led to the assumption that the laser energy destroyed the CNT's distinct structure and that the carbon evaporated. The authors then claimed that the material showed higher hardness and strength due to the effect of carbon atoms from the decomposed CNT; however, no evidence of the decomposition of CNT into C was provided.

From a different perspective, Vora et al. [222] produced AlSi12 parts via *in-situ* alloying through mixing the elemental powders in a mixing drum with ceramic balls to minimize agglomeration or preferential segregation. Comparing the process-ability of the blend and the pre-alloyed powder, the former experienced less residual stress during processing (combined with a higher build-plate temperature) enabling the building of some anchorless structures, e.g. overhangs, which are difficult to achieve in SLM without the use of support structures.

Research regarding in-situ alloying for SLM is still ongoing and can be considered to be at an early stage compared to the work undertaken on pre-alloyed materials. Despite the promising potential in this research area, it still faces numerous hurdles until it reaches maturity. For example, there is the inhomogeneity or segregation of elements that can be introduced in the parts. This is a critical matter because segregation of elements means that in any one produced part there will be regions that belong to different points in the material system's phase diagram. This suggests that the part will incorporate regions that will respond to post-processing heat treatments differently, in addition to performing differently under mechanical loading.

4.1.3. Powder recycling

One of the appealing aspects of SLM is that it is resource-efficient, in particular most unfused powder after a build can be recycled. This minimises the waste material and consequently reduces costs. This is vital for the long-term sustainability and economic viability of the process. Although there are claims that in theory SLM offers 100% material utilisation, this is in reality an overstatement since there is waste in the form of the sieved powder. A more realistic material efficiency of 95% has been reported [223]. However, understanding the effect of laser processing on recycled metal powder and its influence on the microstructural and mechanical properties of the final parts is of utmost importance.

After an SLM process is completed, two types of powder remain in the powder-bed. The first type is composed of powder affected by the build process and includes powder that was partially-melted or heated during the process but was not fused in the fabricated

part; this can in turn be divided into the laser spatter and the condensate (from vaporised powder). Laser spatter is material ejected from the melt pool and is characterised by rougher surfaces that can sometimes be significantly larger than the fresh powder [157] (see Section 5 for more details on laser spatter). The condensate is the gaseous condensate from the processed powder, which is sufficiently small that it is carried away from the powder-bed by the argon flowing in the process chamber. This process-affected powder (spatter and condensate) should ideally be removed, for the reasons explained in Section 5.

The second type of powder recovered after a build is that which has not been laser-irradiated and hence, supposedly, was not affected by the process despite the probability of them being coated by the generated condensate, which could affect the laser absorption, flowability, etc… This second type of powder and fresh powder share similar morphologies, with relatively smooth surfaces. Therefore, this powder is suitable for reuse for other SLM builds by sieving. The distinction between the sieved and reused powder and the fresh powder can be seen in Fig. 10. The microstructure of the sieved reused powder is also similar to the fresh powder. The laser spatter on the other hand shows a coarser microstructure due to the slower solidification of the molten spatter [157].

The similarity between the fresh powder and sieved recycled powder suggests the possibility of producing parts from the latter with comparable microstructural and mechanical properties to those from the former. A comprehensive study on this matter was published by Maamoun et al. [224], detailing the similar microstructure and mechanical properties of parts fabricated using either AlSi10Mg virgin or recycled powder. This was also supported by the work of Asgrai et al. [132] for AlSi10Mg used once, *i.e.* recycled one time only. In other work and for other materials, it has been shown that Stainless steel 17–4 PH [225], 316L stainless steel [226], and IN718 [223] powder can be re-used up to 11, 12, and 14 times, respectively, without deterioration in the properties of built parts. The number of times Al alloys can be successfully recycled is still to be fully determined.

Powder recycling is traditionally carried out by collecting the leftover powder from each build and sieving to remove powder agglomerates and spatter. The sieved powder is then returned to the system for use in further builds. However, the powder is exposed to air during handling and hence the formation of surface moisture and oxides is possible [226,227]. The surface moisture can be counteracted by drying the powder prior to processing and the use of a low power scan per layer before the full power scan also helps alleviate the effect of moisture via *in-situ* drying [159]. The surface oxides, on the other hand, can then break into the melt pools and become trapped as hard oxides in the final parts.

The particle size distribution of the powder changes slightly with reuse in that the fraction of smaller particles is reduced [226] and larger particles increased [228]. This indicates that there must be a threshold for the number of times metal powders can be recycled without negatively influencing the quality of the produced parts or a strategy to unify the properties of the recycled and virgin powders. Recently, a method and apparatus were patented by O'Neill [229] to de-oxidize residual metal powder from AM so that it could go back into the system with properties close to the virgin powder. This apparatus includes a conveyor to transfer the leftover powder to a reducing chamber filled with hydrogen gas or a reducing liquid to recondition the powder through removing the oxides. The process can be accelerated by heating the reducing chamber. The reconditioned powder is either stored in controlled-atmosphere containers or conveyed back to the SLM machine. Alternatively, some SLM systems are equipped with automatic sieving stations so that the cycle is a closed-loop with minimal environmental exposure.

4.2. The processing environment

The process chamber in an SLM machine is purged with an inert gas so that the process is conducted in an inert environment, where the oxygen level is kept below 0.2%. This is crucial for processing Al alloys given their high susceptibility to oxidation [16,176,230,231]. Oxygen within the process chamber stimulates the formation of oxide layers on top of the processed material that are then broken and embedded in the final parts as defects, being exacerbated by the high temperature within the melt pool with high potential to attracting oxygen. These oxides can also promote porosity formation. The type of inert gas used to flush the chamber is flexible, where argon is the most commonly used purging gas [32,87] but nitrogen and helium have also been used [176]. The type of inert atmosphere has been reported to have little effect on densification of AlSi12, however, helium has been shown to induce brittleness under tensile loading [176]. Helium was also not favoured for some other alloys [232].

The gas flow rate within the chamber influences the quality of fabricated parts through affecting the individual tracks' heights and denudation levels [233]. It controls the amount of condensate and spatter removed during processing [234]. The amount of spatter produced is controlled by the laser power and spot size [33], among other factors. Inefficient removal of the spatter might lead to its entrapment as inclusions [123] given that their structure and chemical composition is different from the original powder [157].

4.3. The materials and their qualification

Prior to starting the experimental aspect of material qualification for a new material, the authors believe that it is useful to use simulation models to determine the processing space, such as the D-optimal [235] and response surface [87] methods in the Design of Experiments approach. It is also important to understand a material's thermal behaviour during SLM, as this will aid in predicting the microstructures to be produced alongside the mechanical properties of the parts. Furthermore, this is essential for research on developing alloys for SLM. Investigating this experimentally is difficult, which also points to the use of computational modelling.

The experimental approaches [34] to material qualification have received more attention than the theoretical. Although they are quite costly and time-consuming, their relative ease could be the reason behind their extensive adoption. The complex nature of the process, with some regions being re-melted more than once, requires thorough understanding before the prediction models can be trusted to accurately represent the stages the material goes through during laser irradiation and material melting and solidification.

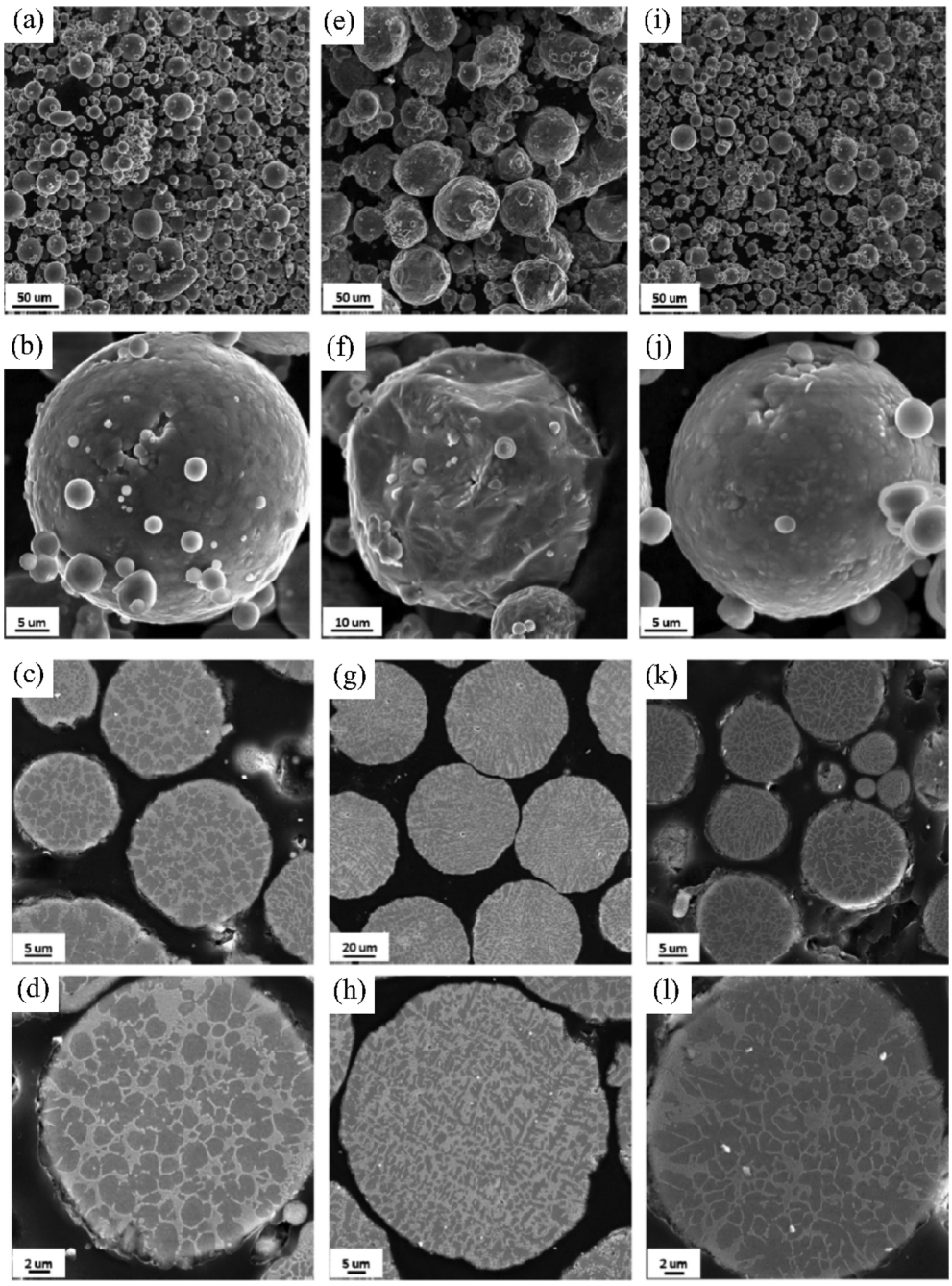

Fig. 10. The spherical and smooth morphology of fresh AlSi10Mg powder presented in (a) and (b) with the corresponding internal microstructure in (c) and (d) seen to be fine equiaxed. The laser spatter significantly larger with a rougher surface is shown in (e) and (f) with the coarser dendritic microstructure in (g) and (h). The similarity between the recycled powder and the fresh powder is displayed in (i–l) [132].

Models should consider several phenomenon taking place in the melt pool, such as material shrinkage (due to the escape of gases trapped in the powder), evaporation (due to exceeding the boiling point of the metal), and material removal via the gas flow within the chamber [236]. Numerical simulation models have been developed [34,236] utilizing data from single tracks experiments. These can predict (1) the temperature distribution in a melt pool and its variation with speed and power and (2) suitable combinations of parameters to produce dense parts. For the work on modelling the SLM process, readers are referred to the review in [129].

Various experimental approaches have been proposed in the literature to define the best set of process parameters for the production of fully-dense parts. One of the common approaches is to build cubic samples, using a range of energy densities, and then quantify the defects, such as pores. By quantitatively tracking the evolution of porosity versus the energy density, the optimum

combination of parameters can be determined, such as in the work by Wang et al. [108]. The drawback to this approach is that the operator is left with infinite possibilities for the combinations of parameters to be examined. This makes the process exhaustive and infeasible, since the best combination can be easily missed out. Furthermore, there is the limitation on using the volumetric energy density as a sole design parameter, as discussed in Section 2.

Wei et al. [237] and Aboulkhair [36] conducted material qualification through producing single tracks with various speeds and powers, then individual layers, eventually progressing to cubic samples (bulk components). The scan tracks were analysed by: (I) evaluating the presence of irregularities and distortions along their lengths, *i.e.* defining zones of continuity and (II) determining the geometrical features of each melt pool. This analysis narrows down the process window for the power and speed. It is also used to define the layer thickness and hatch spacing through the shape of the melt pool [101]. Although the layer thickness is usually pre-defined, inclined platforms can be used for investigating its influence alongside the other process parameters (power and speed) [100,101]. The best combination of speed and power are then used to create individual layers varying the hatch spacing to ascertain the one that ensures the construction of a consolidated defect-free layer [37]. Single layers and walls are also used to optimize surface roughness and to investigate the presence of brittle or hard oxidation on the surface [210]. The overlap can either be in the horizontal or vertical planes to create a layer [37,238] or a thin wall [115], respectively.

There are some requirements that need to be fulfilled in single tracks and layers: (1) continuity, (2) each layer must lightly penetrate the previous layer, (3) each layer has to be high enough to build up the part cumulatively, and (4) the connection angle with the previous layer should be close to 90° [203]. Bonding of a layer to another is controlled by wettability, *i.e.* molten powders spreading instead of balling [200,205]. A good bond between two layers minimizes the formation of cracks or pores.

In the final stage of process parameter(s)-definition, cubic samples with minimal porosity can be fabricated by fine-tuning the parameters and it is at this stage where the effect of deploying various scan strategies is investigated. This bottom-up approach saves time expended with starting straightaway with cubic samples, enabling a wider range of potential parameters to be investigated. The time expended building cubic samples and analysing them is much greater than that needed to construct and analyse single track, walls, or layers.

The alloys AlSi10Mg and AA-6061 were two of the first Al alloys to receive attention in SLM processing [239]. However, they were initially found to be difficult to process for various reasons. The difficulties in the case of AA-6061 were related to the formation of thin oxide layers that promoted porosity formation [145] and solidification cracking [111]. The challenge with AlSi10Mg was excessive porosity and the need for high energy densities [29].

When processing Al alloys, it is advised to use slower scan speeds [32,34,87] with high laser powers [105] for better densification. Because of their high reflectivity and thermal conductivity [32], Al alloys require a high laser power [105] to broaden the processing window [35]. The laser power and scan speed are claimed to be the most influential parameters [240]. The use of high laser power (up to 1KW) has been shown to increase the usable speed range [29]. The relative density of the parts is then inversely related to the scan speed and is demonstrated by the results collated in Table 2 and an example can be seen in Fig. 11.

Slower scan speeds mean higher temperature within the melt pool and hence lower viscosity, enabling the liquid to spread, thus improving bonding [34]. The slower the speed, the more molten material there is thus producing deeper and wider melt pools [101,202,243]. Thus the size of a track (depth and width) is inversely proportional to the scan speed [38]. Another issue is that at high scan speeds, balling is promoted [32] causing porosity [204] and surface defects. A scan speed range has been defined for AlSi10Mg below which irregularities were observed and above which insufficient melting and lack of fusion between layers occurred [155,203].

The mode of melting during SLM is controlled by the balance between the material's conductivity and reflectivity [244]. Aboulkhair et al. [38] concluded that the dominant mechanism for AlSi10Mg was keyhole-mode melting (see Fig. 7(b)) for the parameters investigated in their study. Qi et al. [135] observed a correlation between the scan speed and the melting mode for AA-7050. At slow scan speeds, the keyhole mode dominated, with the melt pools having a conical shape. As the speed increased significantly, a shift to conduction mode occurred resulting in a semi-circular melt pool. Intermediate speeds resulted in a mix of both melt pool shapes, indicating a transition phase from one mode to the other. This should be taken into account when selecting the layer thickness and hatch spacing employed during processing.

All the above-mentioned experimental approaches have proven successful for material qualification. The main difference from one approach to another is the time and effort consumed to optimize the parameters for an alloy.

One of the main hindrances to efficient material qualification for SLM is that the results are not yet transferrable between machines. Therefore, every manufacturer has to develop their own sets of parameters for each material, as demonstrated in Table 2 for AlSi10Mg. The comparison between the listed studies shows how different the parameters are from one machine-make to another to achieve roughly similar relative density. Even for the studies that use the same machine manufacturer, some discrepancy can be seen which could also be attributed to the properties of the raw material, assuming that machines (of the same model) from the same manufacturer behave similarly. The theoretical approach to narrow down the parameters window is capable of reducing the amount of experimental work needed to define the optimised parameter set. Therefore, their use can help reduce the effort and expense incurred by manufacturers in optimising process parameters.

As discussed previously, there is no direct correlation between the energy density values and the quality of the produced part and it is clear that simply using energy density in its current form is not able to fully represent the SLM process. For example, ED does not take into account the scan strategy and scan pattern and constitutes the layer thickness rather than the actual depth of penetration of the laser energy. It also does not reflect the spot size of the laser beam used, which affects the amount of energy delivered to the material; for example: a 100 W laser power using a spot size of 25 μm in a Realizer SLM-50™ will not deliver the same energy as the 100 W from the 70 μm spot size in a Renishaw AM250™. The energy density formula fails to reflect this. Furthermore, the same energy density can be achieved using diverse laser power and speed combinations. Given how each parameter affects the quality of the part distinctively, the energy density as a material qualification quantity for SLM can therefore be misleading.

Table 2
Examples for the outcome from some material qualification studies on a range of Al alloys listing the optimized process parameters (P: laser power, v: scan speed, h: hatch spacing, and t: layer thickness).

Alloy	Machine used	Investigated range[†]				Optimised values				Energy density (J/mm^3)	Relative density (%)	Ref.
		P (W)	v (mm/s)	h (mm)	t (mm)	P (W)	v (mm/s)	h (mm)	t (mm)			
AlSi10Mg	Realizer SLM-50	100	250–1000	0.05–0.25	0.04	100	500	0.050	0.04	100	99.8	[32]
	Concept Laser M2	100–200	700–2000	0.075–0.12	0.05	175	1025	0.098	0.05	34	99.7	[87]
	Concept Laser M1	–	–	–	–	200	1400	0.105	0.03	45	99.4	[40]
	Renishaw AM250	–	–	–	–	200	570	0.130	0.025	108	99.9	[124]
	Trumpf TrumaForm LF130	–	–	–	–	250	500	0.15	0.05	67	> 99	[172]
	SLM-250 HL	–	–	–	–	350	1140	0.17	0.05	36	N/A	[165]
	Custom-made	300–1000	500–4500	0.15–0.3	0.05	1000	2200	0.15	0.05	61	99.5	[29]
AlSi12	Realizer SLM-100	100	100–600	0.1–0.20	0.05	100	150	0.150	0.05	89	89.5	[145]
	Custom-made	100–200	70–200	0.1–0.5	0.2–1	200	120	0.1	0.2	67	77	[175]
	Realizer SLM-100	200	375–2000	0.15	0.05	200	500	0.15	0.05	53	98	[176]
AlSi12Mg	N/A	–	–	–	–	350	921	0.19	0.05	40	99.86	[241]
AlSi20	SLM-250 HL	–	–	–	–	320	1455	0.11	0.05	40	N/A	[187]
A356[‡]	EOSINT M280	200–370	400–3000	0.08–0.18	0.03	250	1400	0.1	0.03	60	99.8	[242]
A357	EOSINT M280	100–370	500–5000	0.1	0.03	300	2000	0.1	0.03	50	99.7	[151]
Al-Cu-Mg[§]	Custom-made	200	83–333	0.07–0.13	0.04	200	83	0.07	0.04	860	99.8	[191]
AA-2219	Realizer SLM-50	70–100	N/A**	0.05–0.17	0.03	N/A	N/A	N/A	0.03	235	97.5	[115]
AA-2618	Realizer SLM-50	70–100	N/A**	0.05–0.13	0.03	N/A	N/A	N/A	0.03	235	> 99.5	[115]
AA-6061	Realizer SLM-100	50–100	50–1000	0.05–0.30	0.05	100	150	0.150	0.05	89	88.7	[145]

[†] The (–) means that a parametric study was not presented in this work.
[‡] Also known as AlSi7Mg0.3.
[§] Chemical composition close to AA-2024.
** Ranges of exposure times and point distances were reported instead of scan speeds.

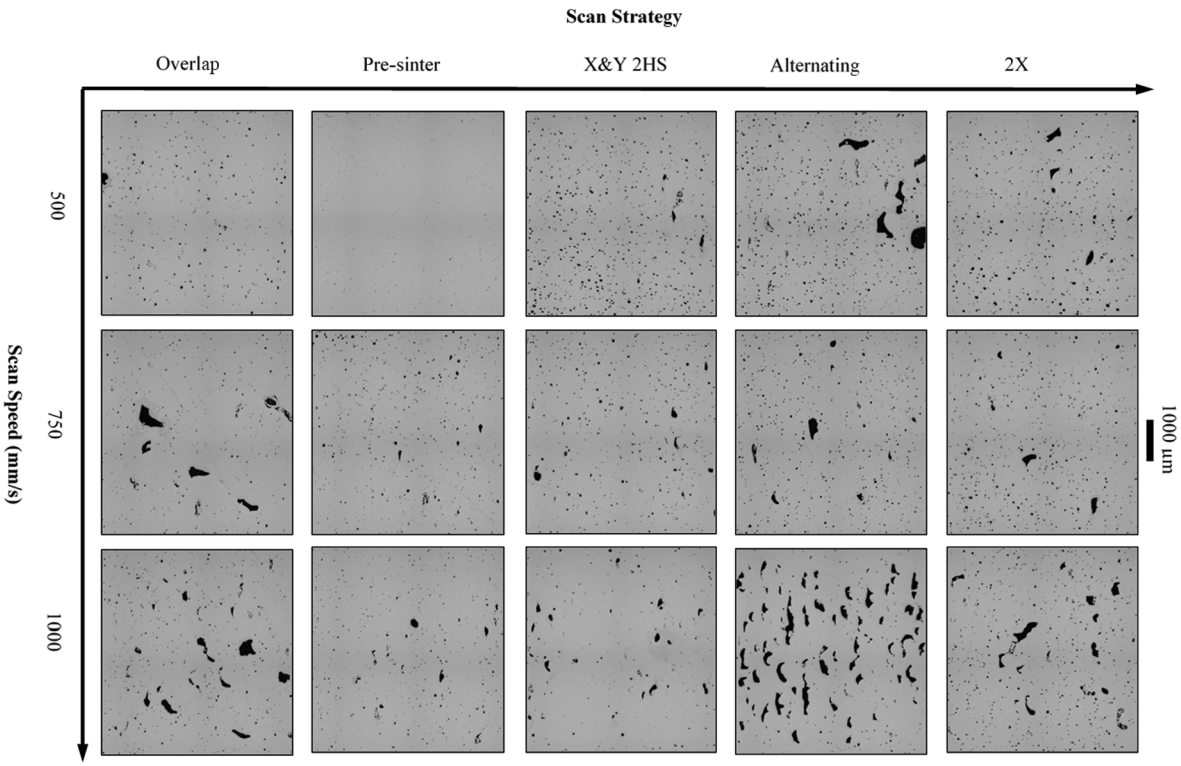

Fig. 11. The effect of changing the scan speed and scan strategy on porosity developed in AlSi10Mg [32]. The strategies used were overlap (scanning each layer twice with the second scan melting the overlap between each two adjacent melt pools), Pre-sinter (scanning each layer twice with the first scan at reduced power), X&Y 2HS (scanning each layer twice, rotating 90° between scans and changing the hatch spacing per scan), Alternating (rotating the scan direction by 90° every layer), and 2X (scanning each layer twice).

Overall, the Al-Si cast alloys are easier to process, compared to the wrought Al alloys, as the main contributor to depressing their relative densities is porosity. The high strength Al alloys, on the other hand, suffer from both porosity and cracking. Optimising the process parameters to minimise porosity has proven feasible. However, to avoid micro-cracking other approaches need to be adopted. These are discussed in Section 5. It is worth noting, however, that for higher strength capabilities (in comparison to the cast alloys), ScalmalloyRP was successfully processed defect-free with 99.9% relative density [245].

As a process parameter, scan strategy has been mostly used to control the material's crystallographic texture [40], the residual stresses in the material [246], or cracking [90]. Thijs et al. [40] showed the use of variable scan patterns to control crystallographic texture. Aboulkhair et al. [32] investigated the effect of the scan strategy on porosity formation. They [32] started by building parts with the simplest scan strategy, *i.e.* the unidirectional scans, and tested a range of scan strategies, tracing the evolution of porosity formation in terms of quantity and type to define the best suitable scan strategy for the investigated alloy (see Fig. 11). This investigation concluded that the scan strategy not only controls the crystallographic texture and residual stresses in the material but also has an effect on porosity, both quantitatively and qualitatively.

5. Defects in SLM of Al alloys

5.1. Types of defect

5.1.1. Porosity

One of the most common defects in SLM parts in general, irrespective of the material, is porosity. Most material qualification studies start with the objective of minimising porosity in the fabricated parts. SLM Al samples suffer from extensive porosity, which Buchbinder et al. [29] attributed to the material's low laser absorptivity in the SLM wave-length range, which affects the melt efficiency during processing.

Two types of pore, based on their distinctive shapes and formation mechanisms (see Fig. 12) were categorised by [32]. The first type has a spherical morphology with a small size (up to tens of microns [152]) – these are referred to as metallurgical pores and, further, Weingarten et al. [159] denoted them as gas pores or hydrogen porosity in reference to their formation mechanism. Their formation is attributed to the presence of moisture on the surfaces of the starting powder as well as the readily-entrapped hydrogen.

The second type of pore has an irregular morphology and is larger in size (hundreds of microns [152]), typically spanning across several layers. Maskery et al. [156] visualised these pores in 3D and observed a geometric anisotropy, with a flat disc-like shape. They are referred to as keyhole or "lack-of-fusion" pores and can be found to enclose non-molten powder. The presence of non-molten powder might not be observed due to smearing or removal whist polishing when using common metallographic techniques. Some of this type of pore have also been attributed to the presence of oxides in the sample that form during melting and solidification [170].

The type of pore has been reported to be dependent on the scan speed employed during processing [32], as shown in Fig. 12. The faster the scan speed, the more keyhole pores are formed, as this is associated with melt pool instabilities and incomplete melting and filling of the melt pool area. Metallurgical pores, on the other hand, increase as the scan speed is reduced due to the higher amount of energy induced in the melt pool. These observations are only valid within the range of scan speeds investigated in the study (250–1000 mm/s). Weingarten et al. [159] investigated the use of scan speeds below 250 mm/s and reported that the metallurgical pores start to decrease again beyond a critical speed lower limit. However, their results from speeds exceeding 250 mm/s support the findings in [32].

This distinction between the type of pore and how they are controlled by the scan speed shows that although most of the process parameters have a quantitative influence on porosity formation, *i.e.* they have an effect on the amount of pores produced in the part, the scan speed controls porosity in a qualitative way additionally [32].

5.1.2. Cracking

High strength Al alloys suffer from extensive cracking when processed by SLM due to the steep cooling curves associated with the process, *i.e.* the melting and solidification dynamics. This has been evidenced by Sistiaga et al. [122] and Martin et al. [111] in AA-7075 and Qi et al. [135] in AA-7050. The AA-7075 alloy is sensitive to hot cracking during fast solidification, hence its poor weldability [125]. In addition, the presence of pores can potentially promote cracking due to the notch effect [125].

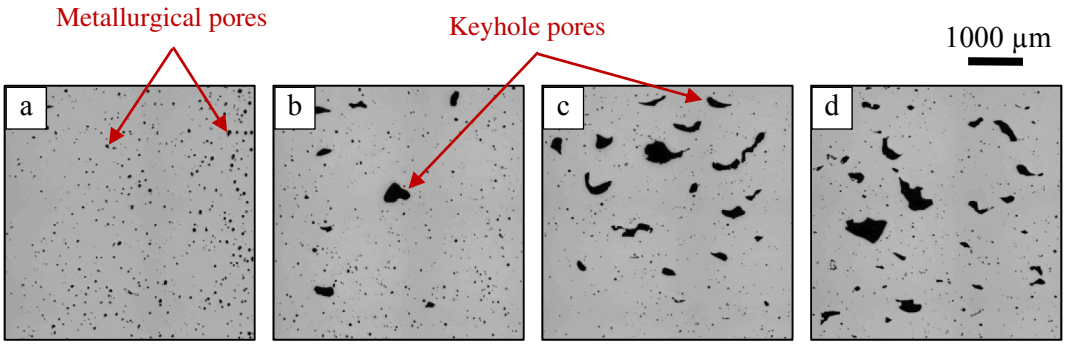

Fig. 12. The change of pore type formed during processing with the scan speed. Metallurgical pores form at (a) the slowest scan speed and as the scan speed increases gradually in (b, c, and d) the amount of metallurgical pores decrease and keyhole pores are promoted [32].

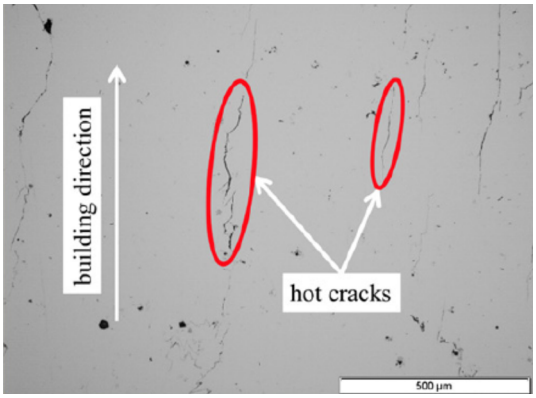

Fig. 13. Hot cracks formed in SLM AA-7075 along the build direction [125].

Martin et al. [111] reported cracks forming in AA-6061 parallel to the build direction, a similar observation to Kaufmann et al. [125] for AA-7075 (Fig. 13). Cracks in AA-2024 [191] increased with scan speed, which was thought to be due to the presence of Cu and Mg widening the material's solidification range.

During the solidification of high strength Al alloys, columnar grains grow in the direction of the thermal gradient, leaving inter-dendritic liquid at the interface, which coupled with shrinkage, lead to the formation of cracks (Fig. 23). Therefore, the melting mode can be correlated to their formation.

Solidification cracks form and grow along the grain boundaries during the last stage of solidification due to shrinkage and thermal stresses coupled with lack of liquid filling. Keyhole mode melting results in small grains with a higher degree of misorientations compared to the conduction mode, thus cracking is more evident in case of the latter [135]. Also, the formation of residual stresses exceeding the material's yield strength during solidification promotes the progression of cracks along that direction.

5.1.3. Laser spatter

Laser spatter is created in the form of small droplets of material expelled from the melt pool, oxidising in-flight [157] with the spatter then landing onto the powder-bed. Spatter is classed as a defect; if it lands in the area where a part is being fabricated, it can get trapped as a contaminant that does not completely melt during re-melting while processing the following layers. An example of a laser spatter particle that was trapped and not re-melted during processing AlSi10Mg is shown in Fig. 14. This was observed on the fracture surface of a sample that failed under cyclic loading.

The region onto which the spatter is expected to land is dependent on the process parameters, *i.e.* the spatter ejection path change with the parameters employed during laser scanning [247]. Laser spatter landing on the powder-bed can also worsen the surface roughness and promote porosity formation.

The reason behind spatter formation has long been believed to be the vapour recoil pressure and splashing within the melt pool. This analogy is borrowed from the welding literature. However, Ly et al. [248] recently published results indicating that this mechanism only counts for approximately 15% of the spatter forming in SLM. The remaining spatter was attributed to vapour-driven entrainment of micro-particles by the surrounding gas flow.

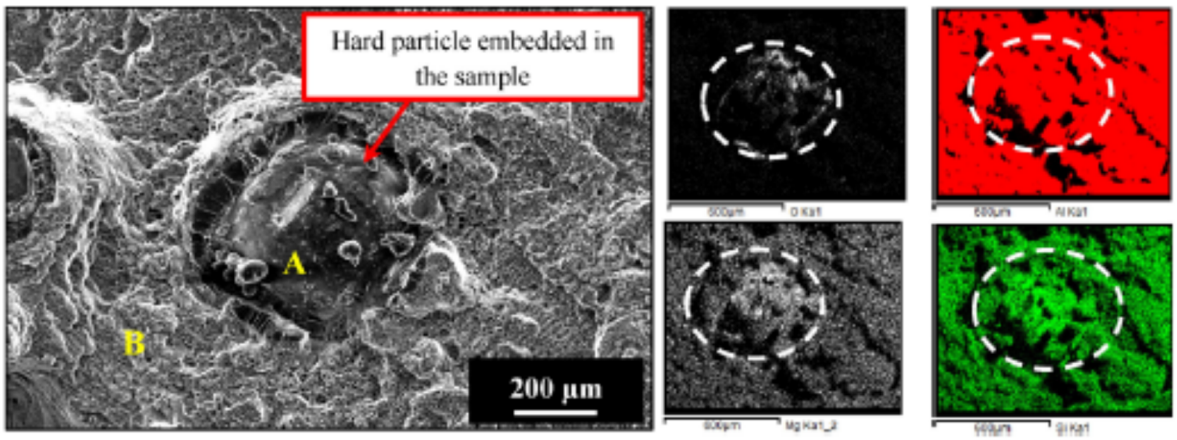

Fig. 14. Laser spatter particle embedded as a defect in AlSi10Mg samples as seen on the fracture surface of a fatigue sample. The energy dispersive spectroscopy maps show that this particle is rich in Si, Mg, and O typical of laser spatter [123].

Kaufmann et al. [125] reported loss in Zn of 1.6% when processing AA-7075 due to vaporisation of the element driven by the difference in evaporation temperatures between Zn and Al and Aboulkhair et al. [32] observed loss in Si and Mg in AlSi10Mg samples where the laser spatter was correspondingly rich in Si and Mg. According to Simonelli et al. [157], AlSi10Mg laser spatter has a spherical morphology with a size that is much larger than the fresh powder and it also has a textured or rough surface, with patches of surface oxides primarily rich in Mg. Selective oxidation reactions take place on the surface of the laser spatter, thus explaining the favouring of Mg oxides; Mg being a volatile element with strong affinity to oxygen.

The formation of laser spatter is usually accompanied with the loss of elements in the bulk sample, *i.e.* an alteration in the chemical composition of the produced sample when compared to the starting powder which can lead to microstructural changes upon solidification. In addition, there will be uncertainty in the level of adherence to the required composition in the fabricated parts, potentially affecting the mechanical properties of the parts, as well as their response to post-processing heat treatments. Martin et al. [111] advised adding traces of the elements that are susceptible to evaporation to account for this phenomenon in advance.

5.1.4. Surface defects

Various types of surface defects can form in SLM parts. Surface open pores and poor surface finish are quite common. The surface roughness of SLM parts is nearly 4–5 times that of the machined surfaces [249]. The high surface roughness is mostly due to the balling phenomenon and the presence of satellites, which together result in producing parts with a wide range of surface irregularities. Both features are shown in Fig. 15.

Balling is scan speed dependent; the higher the scan speed the more balling features are observed [32,161]. As can be seen in Fig. 15, a ball has the same microstructure as the rest of the built material whereas, conversely, satellites have a microstructure similar to the fresh powder. Satellites pose less probability of affecting the build process due to their relatively small sizes, whereas balls, with their significant sizes, can hinder the success of a build. Excessive balling will prevent the deposition of uniform layers of powder and so failure can occur. Furthermore, the irregular surface might include gaps and trapped powder, which promote porosity [250].

5.1.5. Shape distortion

SLM parts suffer exaggerated amounts of thermally-induced residual stresses, driven by the fast cooling rates experienced in SLM and can result in distortions in the shapes of the desired parts. As an SLM layer is scanned line-by-line, plastic compressive stresses form at the beginning of each scan vector whereas plastic tensile stresses form towards the end; the latter having a lower magnitude [28]. The distortion of an SLM part can occur during processing, in which case the build will fail, or during removal of the part from the build-plate after the process.

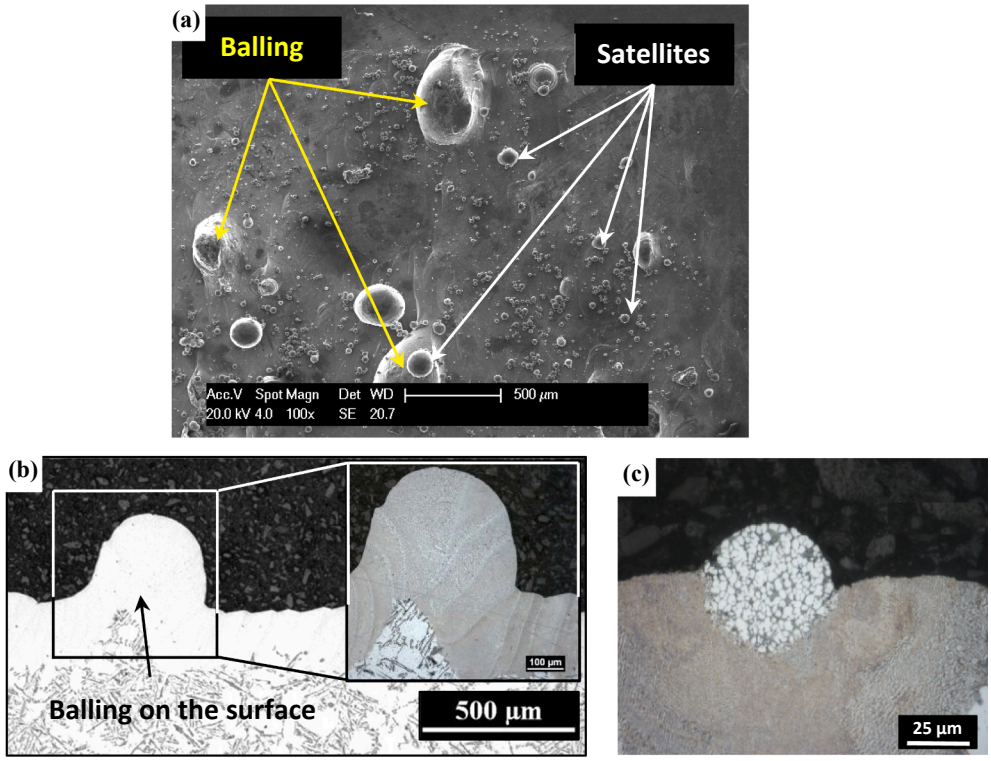

Fig. 15. (a) Balling and satellites on the surface of AlSi10Mg sample, (b) a cross-sectional view for balling on the surface of AlSi10Mg sample, and (c) a cross-sectional view showing a satellite that landed on a single track of AlSi10Mg with the satellite showing a microstructure similar to the fresh powder [38].

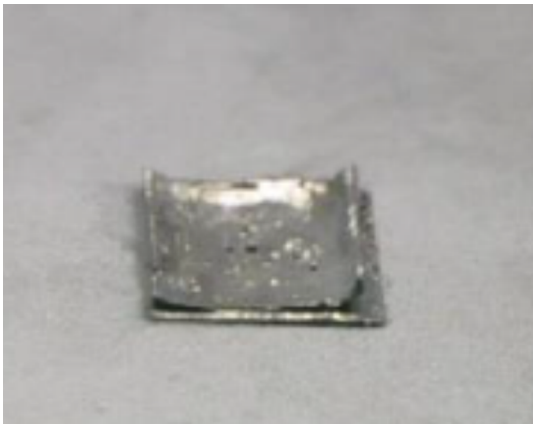

Fig. 16. Flaking behaviour during SLM of pure Al [251].

One of the forms of distortion that occurs during processing is flaking due to the layer being processed not bonding to either its preceding layer, the support structure, or the substrate, and thus peeling off as shown in Fig. 16. Flaking behaviour can be instigated by building on a build plate of a dissimilar material [251]. Shrinkage during solidification is another form of shape distortion, which causes lack of dimensional accuracy.

5.2. Methods of defects detection

Porosity in SLM samples can be quantified using cross-sectioning and microscopy [29,32,87], X-ray computed tomography CT [156,252,253], the Archimedes method [145,176,254], or spatially resolved acoustic spectroscopy (SRAS), [255,256]. Of the first three methods, the Archimedes method (with water or acetone) provides the most reliable results for medium-to-large samples, especially for specimens of low porosity [257]. Cross-sectioning and microscopy rely on the analysis of one section (or a small number) from the sample; however, the likelihood of this slice representing the whole sample is low. This is even more critical in the case of samples with low pore fractions as the chances of missing slices with pores increases.

Cross sectioning and microscopy suffer two more shortcomings. Firstly, the accuracy of the quantitative measurement of the pore fractions is easily affected by the thresholding algorithms used to process the micrographs [258–261]. Secondly, the protocol for metallographic preparation of the cross-section can play a role in determining the detected level of porosity. Softer metals can experience metallographic smearing, which closes small pores causing an underestimation of the total porosity. Also, trapped, partially-sintered powder particles can be removed from large, keyhole, pores – see Fig. 17.

Despite its shortcomings, micrograph analysis is useful in assessing pore size, shape, and position, which is not obtained using the Archimedes method. This information can be very useful during material qualification, as the types of pores and their locations can be related to the process parameters [32,262,263], thus providing a guidance for parameters optimisation. X-ray CT is even more useful in this respect, since the pores are characterised in 3D. Therefore, it has been used for pore analysis [156,245,253,262–264] and correlating pore morphologies to mechanical failure mechanisms [265,266].

Besides being used for porosity evaluation, cross-sectioning, X-ray CT, and SRAS have also been used to investigate the presence of cracks, especially their density and orientations [90,93,267]. Surface defects, on the other hand, do not require sophisticated tools for detection. Visual inspection can be sufficient for features such as balling and shape distortion in the form of swelling or curling. Contact [268] and non-contact profilers [250] as well as coherence scanning interferometers [269] can be used to characterise the parts' surfaces alongside microscopy [250,270].

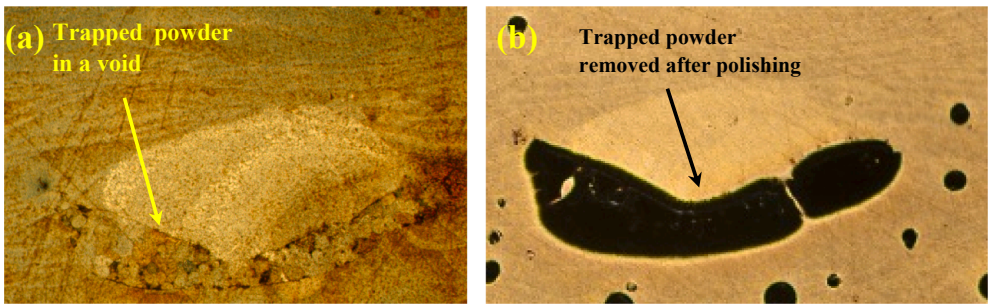

Fig. 17. AlSi10Mg sample processed by SLM: (a) polished without removing the trapped powder, and (b) polished until the removal of the sintered powders.

5.3. Current approaches to minimise defects in SLM parts

Al alloys have been qualified in various research studies that produced near fully-dense parts (with relative densities surpassing 99.8%, as demonstrated in Table 2) after thorough process parameters optimizations. The approaches to achieve this result were quite distinctive. Buchbinder et al. [29] recommended the use of high laser powers up to 1 KW to compensate for the material's low laser absorptivity. However, this is not convenient for systems that are not equipped with such high laser powers; the SLM system used in that study being custom-made and therefore, this solution is limited to machines with such capability.

Aboulkhair et al. [32] tailored the scan strategy to minimise porosity without the need for high laser powers. The use of a "pre-sinter" scan strategy, where every layer is scanned with a pre-melt scan at half the laser power needed for melt, significantly reduced porosity, enabling the production of near fully-dense parts. This approach was further supported by Weingarten et al. [159]; according to their study drying the powder before processing reduced porosity by 50% (in agreement with Yang et al. [152]) and the use of a preliminary scan (with lower power) prior to the main scan acted as an in-process drying step reducing the moisture content before irradiation with the main scan, reducing the pore fraction by 90%.

These studies reduced porosity during processing to produce near defect-free parts in the "as-SLM" state. Conversely, Tradowsky et al. [166] adopted the approach of reducing porosity in post-processing by applying a hot isostatic pressing (HIP) treatment to the SLM parts. Although their procedure "*closed*" the pores leading to a quantitatively lower porosity content, it is not recommended from a structural point of view as a HIP treatment may close the pores whilst retaining weakness that is revealed as soon as the part is subjected to high temperature or loading, leading to the parts' failure. For instance, Cunningham et al. [271] observed that pores that were closed during a HIP treatment not only reopened again once the material was heat-treated but they actually became larger compared to their original sizes before HIP. Furthermore, HIP can cause surface oxidation due to high temperature and pressure.

Shot peening is another post-process remedy that has been shown to reduce porosity (close to the surface) through pores' shrinkage and collapse [270]. Maskery et al. [156] investigated the effect of various heat treatments (annealing and precipitation hardening (T6)) on porosity; concluding that heat treatment does not affect the number of pores in the material.

Cracks formation during SLM can be attributed to high residual stresses. Selecting the most suitable scan strategy for the material and part to be produced is essential to reduce the amount of residual stresses introduced by the fast solidification rates associated with the process [246]. Another benefit from the freedom offered by the variability in the scan strategy is the possibility of minimizing cracking in weld-crack susceptible alloys by using fractal scan strategies [90]. A correlation between the scanned area and the amount of defects formed has been observed for AA-2618; as the area becomes larger the cracking density increases, as demonstrated in Fig. 18 [272]. The fractal scan strategies effectively push the theory of the checkerboard scan strategy to smaller scales; the area to be scanned is divided into much smaller regions that are scanned via a continuous laser path based on mathematical area-fill curves with a principal scan vector length in the order of nearly 100 μm, reducing the area over which residual stresses can build up. These scan strategies were shown to affect the formation of cracks in a Ni superalloy, however their influence on Al alloys has not yet been investigated.

Another means to reduce or eliminate cracks is altering the composition of the crack-susceptible alloys. For example, changing the composition of the AA-7075 alloy by adding traces of Si has been shown to reduce cracking [122]. Martin et al. [111] presented a study on seeding the main powder with nano-particles to promote heterogeneous new grain nucleation, controlling the resultant microstructure for high strength Al alloys, an approach that successfully resulted in crack-free parts. This is similar to the idea behind the addition of Sc in designing ScalmalloyRP, where Al_3Sc particles form acting as sites for heterogeneous nucleation [139], among other new alloys designed more recently [198].

The use of preheated build-plates is generally considered to reduce the amount of residual stresses introduced in the material through a less steep thermal gradient, therefore decreasing distortion in produced parts [28]. Prashanth et al. [192] significantly reduced cracks in an Al85Nd8Ni5Co2 alloy by heating the build plate to 673 K during SLM processing. Kaufmann et al. [125] attempted to reduce the cracking density via increasing the build-plate pre-heating temperature to 200 °C, but observed no significant effect whereas hot isostatic pressing (HIP) successfully reduced cracks in Ni-based alloys [93]. However, this still bears the disadvantage explained in its use for porosity reduction; closing the cracks by HIP without eliminating them at the source poses the risk of them acting as points of weaknesses once the material is subjected to high temperatures or severe loading conditions.

Post-processing techniques, such as mechanical machining, polishing, or blasting, to improve the parts' surface roughness have all been reported in the literature [123]. Mechanical polishing reduces the surface roughness to values that are comparable to machined parts whereas the effect of electro-polishing was minor [249]. Although such treatments can lead to better mechanical performance, this is not always feasible. For example, a key reason for implementing SLM is the ability to produce complex features with high degrees of freedom; however, the post-machinability of these structures can be impossible to achieve.

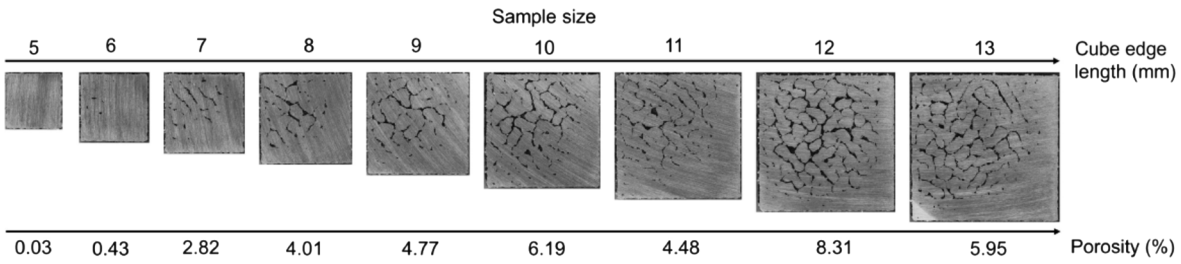

Fig. 18. The effect of sample size on porosity and cracking density forming in SLM AA-2618 [272].

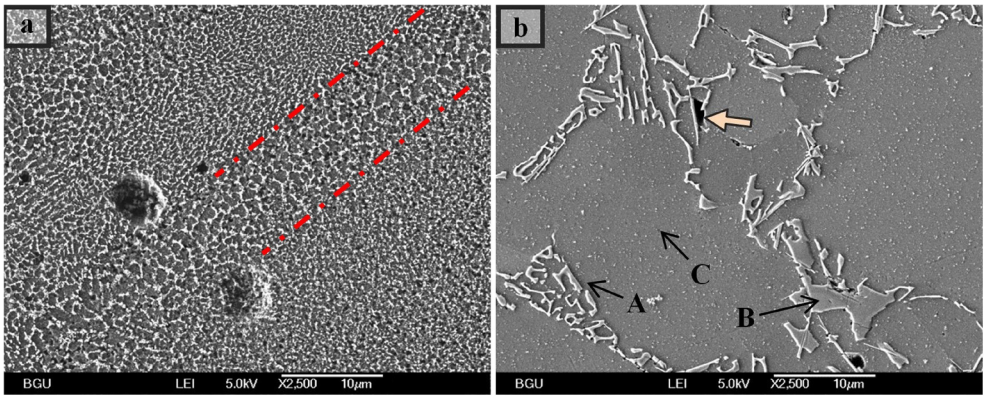

Fig. 19. SEM images showing the clear distinction between the microstructure of AlSi10Mg developed by (a) SLM and (b) casting. The arrows in (b) point to (A) the Al-Si eutectic, (B) Si dispersed in the Al matrix, and (C) Fe-containing intermetallic phases [275].

6. The metallurgy of SLM Al alloys

6.1. Microstructures

The thermal history during SLM [239] controls the formation of the microstructure. The material is subjected to directional heat transfer and high thermal gradients during processing. In addition, it is re-melted several times due to penetration of the laser beam across layers and internal heat transfer. Solidification occurs at a very fast rate (10^3–10^8 K/s [273]) that increases with laser power and scan speed [34] producing a fine microstructure [32] with metastable phases [274]. This fine microstructure is in demand as an alternative to the coarse microstructures developed by conventional manufacturing [34,273]. A comparison between the microstructures developed by SLM and casting is presented in Fig. 19.

Considering the metallurgy of SLM Al-Si alloys, an example of the characteristic microstructure with the overlapping melt pools in the vertical and horizontal directions is shown in the isometric collage in Fig. 20(a). Similar metallurgy has been reported for AlSi10Mg [32], AlSi12 [119], AA-2024 [191], and AA-7050 [135].

The higher magnification scanning electron microscope (SEM) images in Fig. 20 (c) and (d) reveal the microstructure in the planes parallel and perpendicular to the build direction, respectively. Along the build direction, α-Al solidifies with a columnar morphology with continuous segregations of inter-dendritic Si at the boundaries [179]. Each melt pool is divided into three regions [32,40]; (i) the melt pool core where the cells are finer with a more equiaxed structure, (ii) the melt pool boundary where the cells are coarser and mostly elongated, and (iii) the heat affected zone (HAZ).

The solidification mechanism in SLM AlSi10Mg and AlSi12 is cellular-dendritic. A cellular structure is stimulated when there is a high velocity solidification front coupled with constitutional undercooling; both occurring in SLM. Prashanth et al. [179] explained the melting and solidification of AlSi12 during SLM. During cooling down, the solidification front rejects Si into the liquid increasing the Si content in the liquid. According to the Al-Si phase diagram [276] in Fig. 21, the solubility of Si in Al decreases as the temperature drops, except under high cooling rates, which extend the solubility of Si in Al (the Si content in Al in SLM samples is ~7 wt% instead of the expected 1.6 wt% [273]). A similar observation was made for the extended solubility of Cu and Mg in Al in AA-2024 [191]. Therefore, the formation of a cellular structure is promoted in which α-Al solidifies first leaving the residual Si to segregate at the cellular boundaries, as shown in Fig. 20(c) and (d) and Fig. 22(d) and (e).

Qi et al. [135] reported distinction between the microstructures produced from keyhole and conduction modes of melting in that the former contained more fine grains at the melt pool boundary compared to the latter. This is due to the melt pool's high aspect ratio which leads to increased re-melting of the boundaries. The columnar morphology at the melt pool boundary is driven by the tendency of the solidifying material to grow in the direction of the thermal gradient [124], *i.e.* pointing towards the heat source. These columnar or elongated Al cells are observed to be equiaxed when viewed from the plane perpendicular to the build direction. Wu et al. [120] reported the length of the columnar cells to be up to hundreds of microns, with 20 μm width, as demonstrated in the electron backscatter diffraction (EBSD) pattern in Fig. 22(a–c). The higher magnification SEM images in Fig. 22(b) and (c) show sub-cells in the order of 500 nm. This is in agreement with measurements reported in [36], where the coarser cells at the melt pool boundary were in the range of ~650 nm and the finer ones at the melt pool core were in the range of ~500 nm.

This inhomogeneous microstructure results from the liquid oscillations and temperature profile within a single melt pool, as explained by Li et al. [273]. At the centre of the melt pool, the temperature (based on simulations) is 1439 °C, which is higher than the material's branching temperature. Moving further from the centre, the temperature decreases, with a large portion of the melt pool at temperatures within the range between the branching (~1290 °C) and dissolution (~1080 °C) temperatures. This is the range where an inhomogeneous microstructure of Al-rich and Si-rich phases co-existing is formed. Rapid cooling helps retain the Al-rich super-saturated matrix as well as the Si-rich nano-sized particles. The fine microstructure alongside the solidification mechanism explained earlier leads to the formation of parts with a good dispersion of all the alloying elements; as exemplars, this was reported for AlSi10Mg [88] and AA-2024 [191].

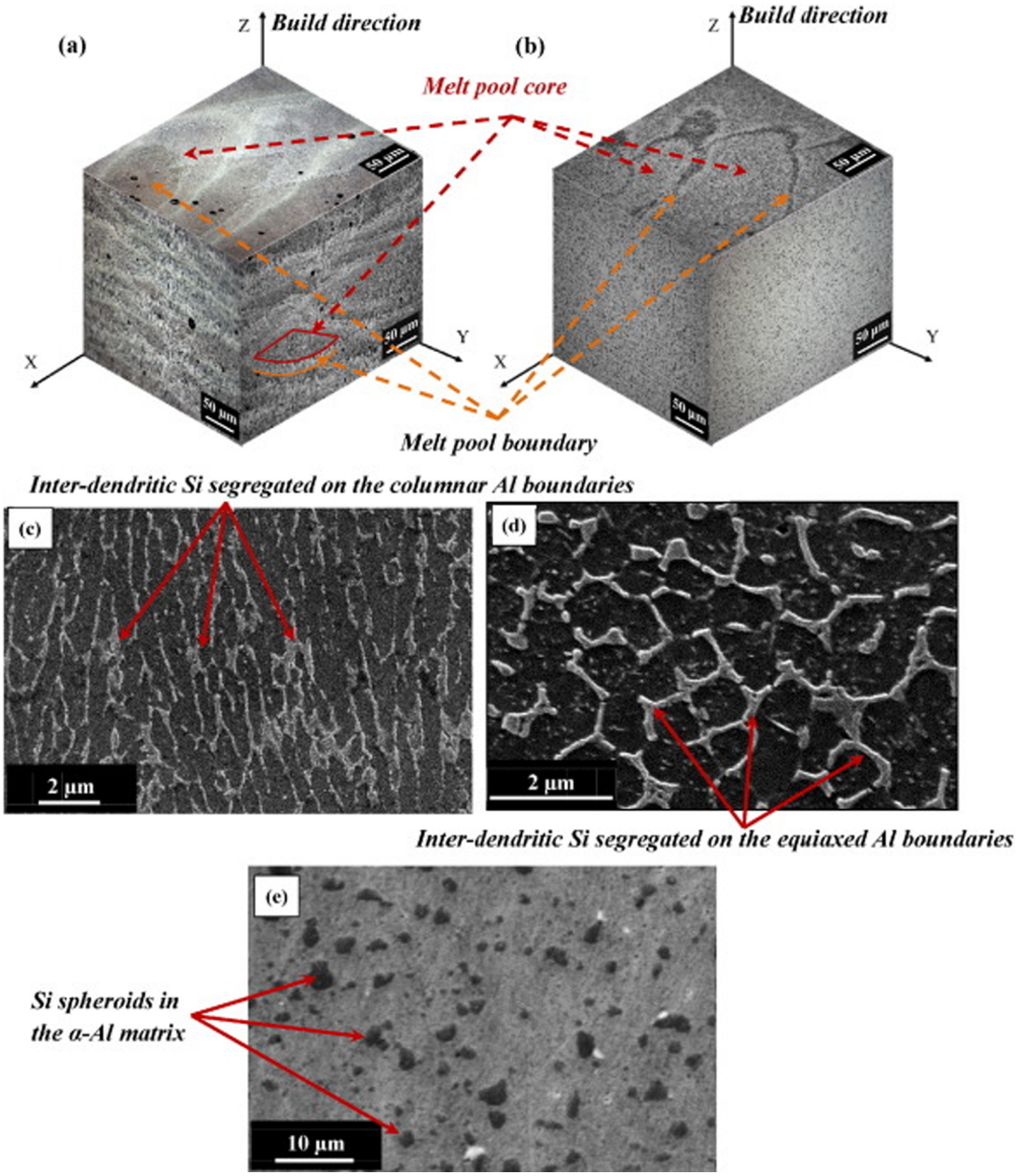

Fig. 20. Isometric views for the microstructure of SLM AlSi10Mg (a) as-built and (b) after heat-treatment, (c) elongated α-Al as seen on the XZ plane in the as-built material, (d) equiaxed α-Al grains as seen on the XY plane in the as-built material, and (e) Si spheroids in the α-Al matrix after T6 heat treatment [123].

Takata et al. [168] found the microstructure described above to be in agreement with the sequence suggested by the calculated phase diagram for AlSi10Mg using Calphad. Furthermore, they reported a change in the microstructure of the material produced depending on the size of the fabricated sample. Smaller samples, in the range of 0.1–0.3 mm, contained Si particles inside the columnar Al grains, indicating precipitation of Si during SLM under these conditions. This can be explained by the efficiency of the heat flow. In the case of the smaller samples, the melt pool is surrounded by un-molten powder which has lower thermal conductivity compared to the solidified material surrounding the melt pool in the case of the larger samples. The lower thermal conductivity reduces the heat flow efficiency, imposing a relatively low rate of solidification, hence, the prolonged durations at elevated temperatures allow for the precipitation of Si in the columnar Al grains.

The elongated, or columnar, microstructure common in SLM Al-alloys has some downsides where, for example, it leads to anisotropic mechanical properties (as discussed further in Section 8). Furthermore, in high strength alloys this columnar growth promotes the creation of cracks during solidification (Fig. 23). Adding lattice-matched nano-particles to the powder before processing can be used to control solidification and replace the elongated grains with fine equiaxed ones, as shown in Fig. 23.

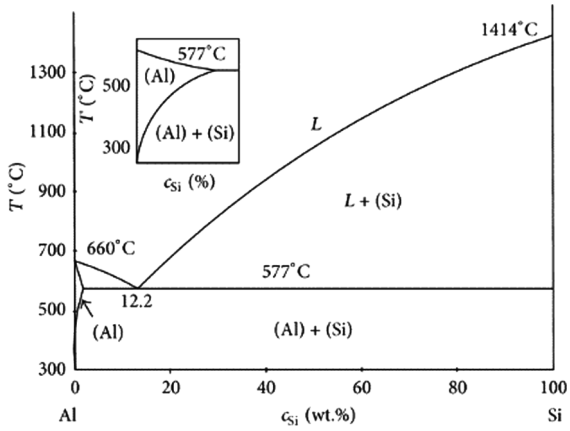

Fig. 21. Al-Si phase diagram [277].

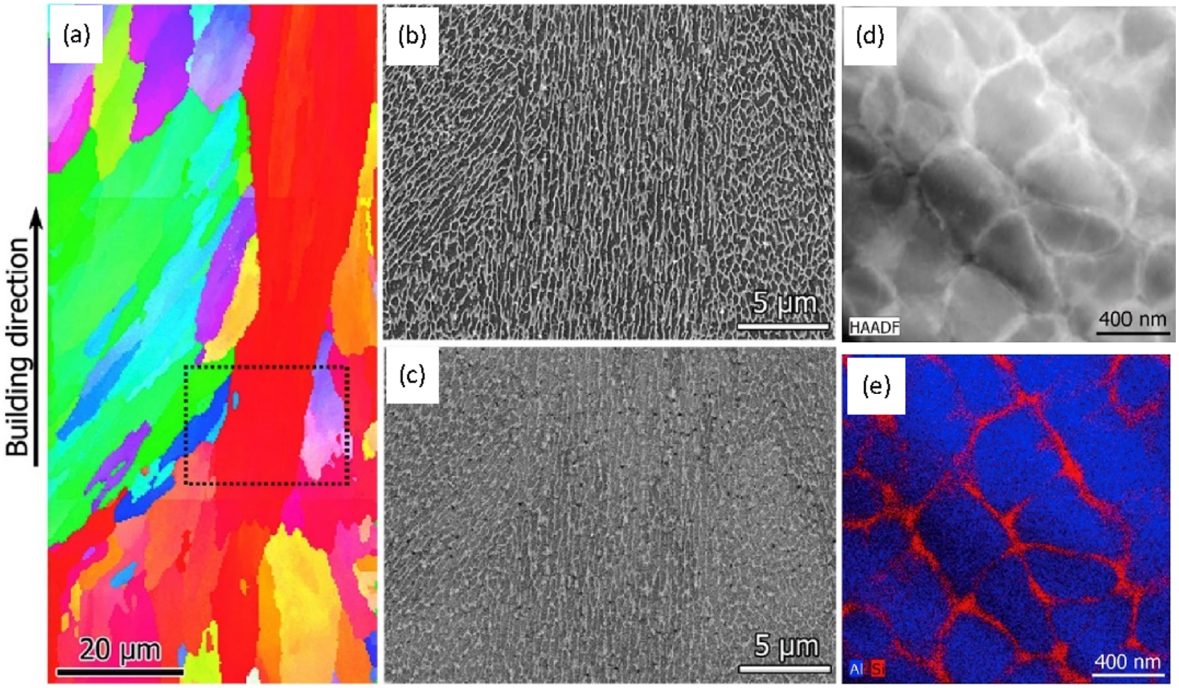

Fig. 22. The (a) EBSD image showing the grain structure of AlSi10Mg produced by SLM with columnar cells growing parallel to the build direction and the microstructure in the dashed region in (a) is shown in (b) using a secondary electron detector and (c) using a backscatter electron detector on a scanning electron microscope. A STEM image for the cells in the as-built SLM AlSi10Mg is shown in (d) with the corresponding Al-Si EDX map in (e) [120].

6.2. Crystallographic texture

Although SLM does not involve any mechanical processing capable of imparting deformation texture, thermal gradients and extreme cooling rates foster epitaxial growth of columnar grains in most Al alloys. This texture causes mechanical anisotropy (yield strength and elongation at failure) and crack susceptibility. The origin of crystallographic texture in SLM Al components is derived from the directional solidification within the melt pool. The melt pool shape and, in turn, the heat flow direction at the liquid/solid interface and solidification rate, are however significantly affected by the choice of processing parameters and the thermo-physical properties of the material. Therefore, the strength of the resulting grain texture varies significantly depending on the equipment and feedstock used [129].

During the early stages of melt pool solidification, the average grain growth direction is a function of the solidification front direction (typically perpendicular to the melt pool boundary) and thermal gradients. Thermal gradients are predominantly opposite to the build direction, or radial, depending on the melt pool width-to-depth ratio, as constitutional undercooling is hindered in most Al alloys due to high thermal conductivity and solidification velocities [111]. These conditions create morphological grain texture, with the longitudinal cross-section of SLM parts showing elongated grain structures developing from the melt pool boundaries. These

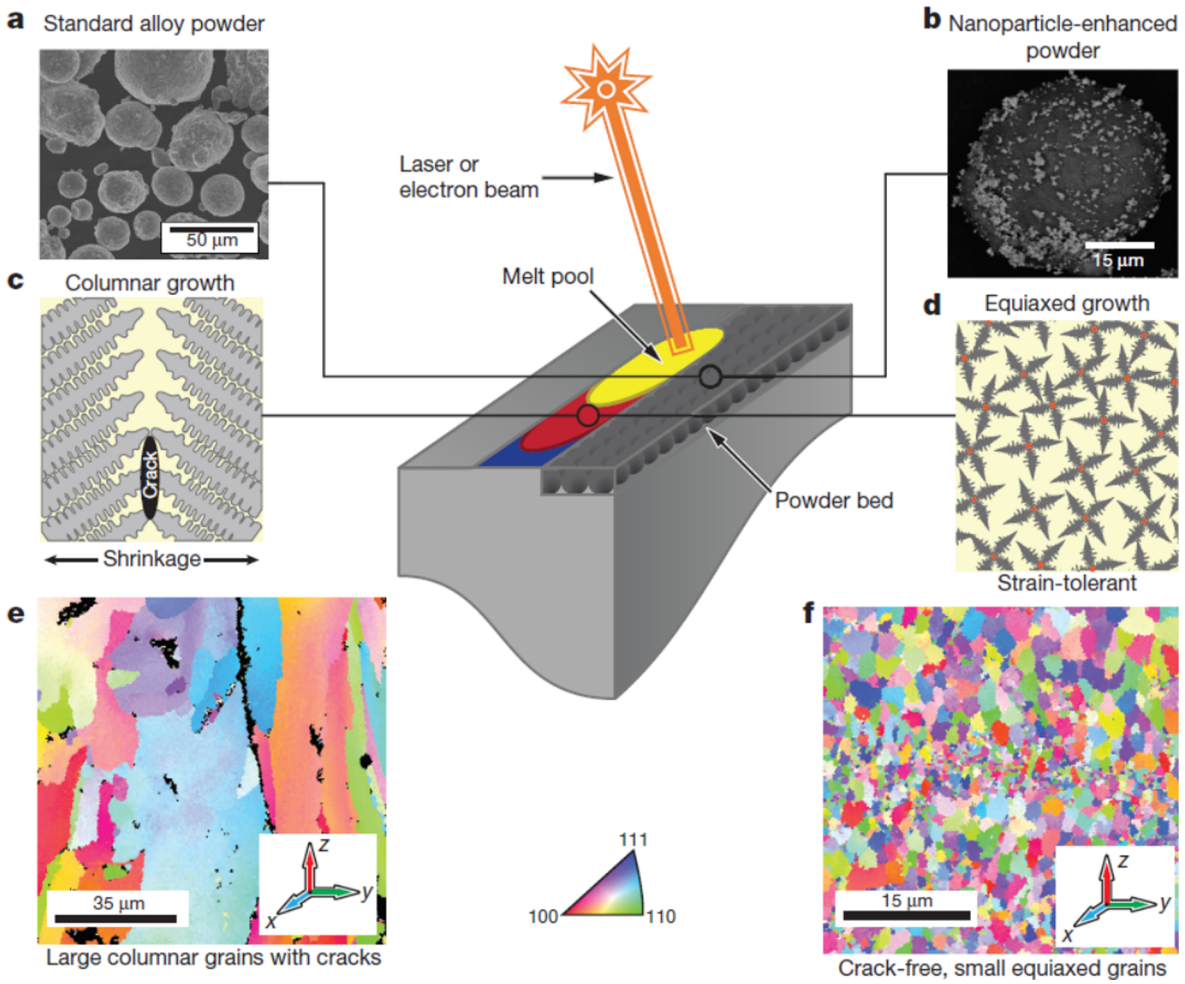

Fig. 23. Adding lattice-matched nano-particles to high strength Al alloys to replace the elongated grains with equiaxed grains and avoid cracking. The standard alloy powder is shown in (a) with (b) showing the powder after adding the nano-particles. The columnar growth in (c) is then replaced by the equiaxed growth in (d). The outcome is that the columnar grains with the cracks in (e) are replaced with the equiaxed crack-free microstructure in (f) [111].

elongated grains are either aligned to the build direction or slanted towards the melt pool centre. Such morphological grain texture is accompanied by a crystallographic texture in metals characterised by "easy growth" directions: this is the case for Al alloys, where dendrites with ⟨1 0 0⟩ directions aligned to the solidification front stifle less optimally aligned grains (Fig. 24).

The coupling between morphological and crystallographic textures of the grain formed from the melt pool boundary has indeed been confirmed by numerous researchers. Wu et al. [120] have shown that elongated grains (found near the melt pool boundaries of SLM AlSi10Mg) consist of sub-cells of identical orientation. Thijs et al. [40] showed that this predominant grain orientation gives rise to a ⟨1 0 0⟩ fibre texture component along the scan direction. Similar results are reported by Suryawanshi et al. [181] for AlSi12. On the other hand, Takata et al. [130] and Zhang et al. [191] demonstrated how the elongated grain structure of AlSi10Mg and Al-Mg-Cu has a dominant ⟨1 0 0⟩ texture along the build direction. Although not explicitly reported, these differences are attributed to variations in the melt pool shape geometry and hence thermal gradients.

As the solidification of the melt pool proceeds, elongated grains either consume the remaining liquid [111,122] or refined equiaxed grain structure forms [40,130]. Equiaxed grains, expected to originate in alloys with narrow solidification range from surface nucleation [40], have no predominant crystallographic texture and are those desirable to minimise mechanical anisotropy.

Recent research has focused on strategies to obtain a more homogenous refined structure throughout the melt pool that would cancel any crystallographic texture and reduce solidification cracking [111,122,139,278,279]. The addition of suitable heterogeneous elements that increase the density of nucleation sites in the melt pool and encourage columnar to equiaxed transition of the grain structure have indeed proved effective in promoting a refined texture-free melt pool grain structures in a number of Al alloys, including Al-Mg-Zr, AA-2xxx, AA-6061, and AA-7075.

The intensity of the crystallographic texture developed in SLM parts depends, additionally, on the way different individual melt pools and tracks are combined. During partial re-melting of the neighbouring tracks, any refined equiaxed structure formed in the latter

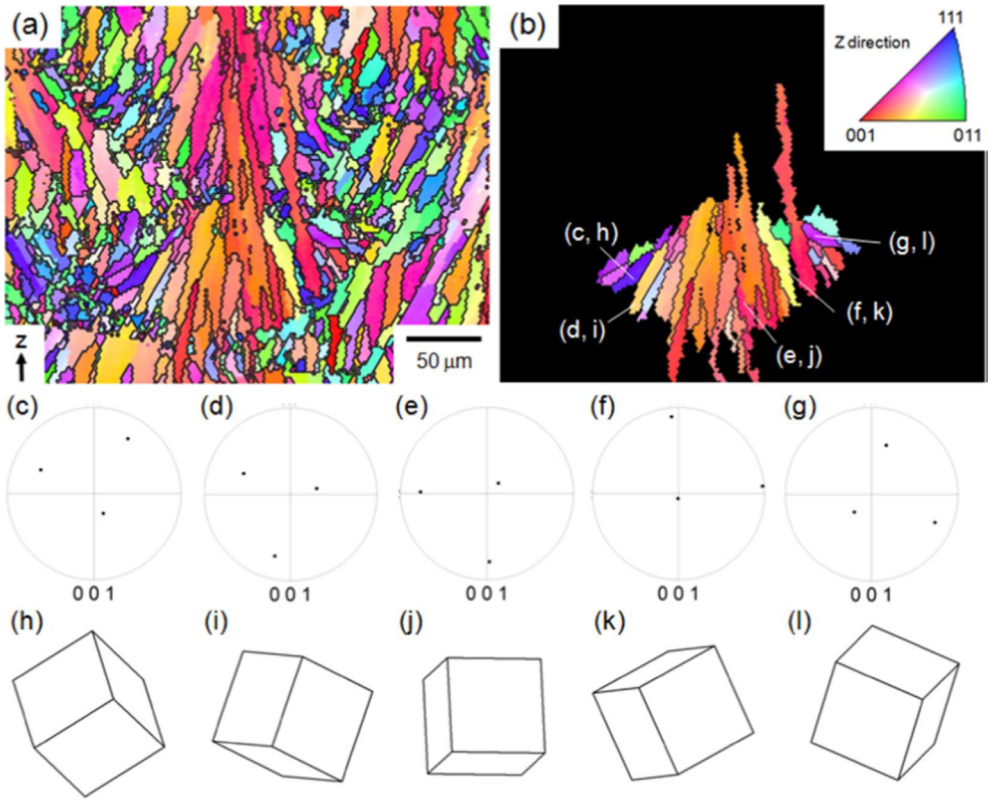

Fig. 24. Inverse pole figure orientation map showing predominant ⟨1 0 0⟩ orientation of the elongated grain structure along the build direction The orientation map shows also refined grain structure at the sides and top of the melt with no distinct predominant orientation [130].

stage of the melt pool solidification can be reduced significantly at the expense of elongated textured grains [40]. Different texture intensity might thus occur when the same alloy is processed when the fraction of textured grains in the part is affected by the amount of partial re-melting of the neighbouring tracks and thus hatch spacing, layer thickness, and laser scan strategy used [40,135].

Inter- and intra-layer rotation of the scan strategy have also proved to be an effective way to reduce texture, as shown in recent studies on AlSi10Mg [40,181] where melt pools formed by the moving laser source are elongated in shape, and rotating the scan direction reduces the amount of re-melted material in comparison to uni/bi directional scan strategies and encourages retention of the randomly-orientated equiaxed grain structures formed in the firstly solidified melt pool (Fig. 25).

7. Heat treating SLM Al alloys

Despite the increasing interest in SLM of Al alloys, thermal post-processing has mostly been limited to the application of traditional heat treatments to the SLM material. These traditional procedures have been specifically-tailored for the completely different microstructures that are produced from conventional processing methods. In principle, the aim of any heat treatment procedure is to modify the microstructure in order to alter the mechanical properties to suit its function in an application. Therefore, designing a heat treatment procedure should take into account both the starting and resultant microstructures.

As established in the previous section, the microstructures produced by SLM are substantially different from those from conventional processing, suggesting that their response to a particular heat treatment will be dissimilar to that of a conventionally-manufactured part. Both AlSi12 and AlSi10Mg exhibit meta-stable cellular microstructures upon processing by SLM [119]. Prashanth and Eckert [119] attributed the formation of these unique characteristic microstructures to (i) the high solidification rates associated with the process, (ii) the near eutectic composition, and (iii) having a Si-Al equilibrium partition ratio less than one. The metastable cellular microstructure leads to phase transformation by decomposition with heat treatment. As the SLM material is annealed, the fine low-angle grain boundaries sub-structure is consumed [130] through annihilation during recovery of the array of dislocations originally present in the as-built material. The Si, which is originally in the form of continuous segregations around the α-Al cells, decomposes into spheroids of Si, resulting in a composite-like microstructure with an Al matrix reinforced by Si particles, as can be seen in Fig. 20(b) and (e). The Si content in Al dropped to the 1.6 wt% after 30 min of solution heat treatment at 500 °C [273]. The spherical morphology of the Si particles is attributed to the thermally-activated growth of Si along the most stable plane with the lowest free energy, *i.e.* {1 1 1} [273]. The Si particles coarsen with increasing the treatment duration, *i.e.* the number of Si particles decreases and their size increases as particles coalesce [162]. This spherodisation phase transformation has been reported when annealing AlSi12 [119,179], AlSi20 [187],

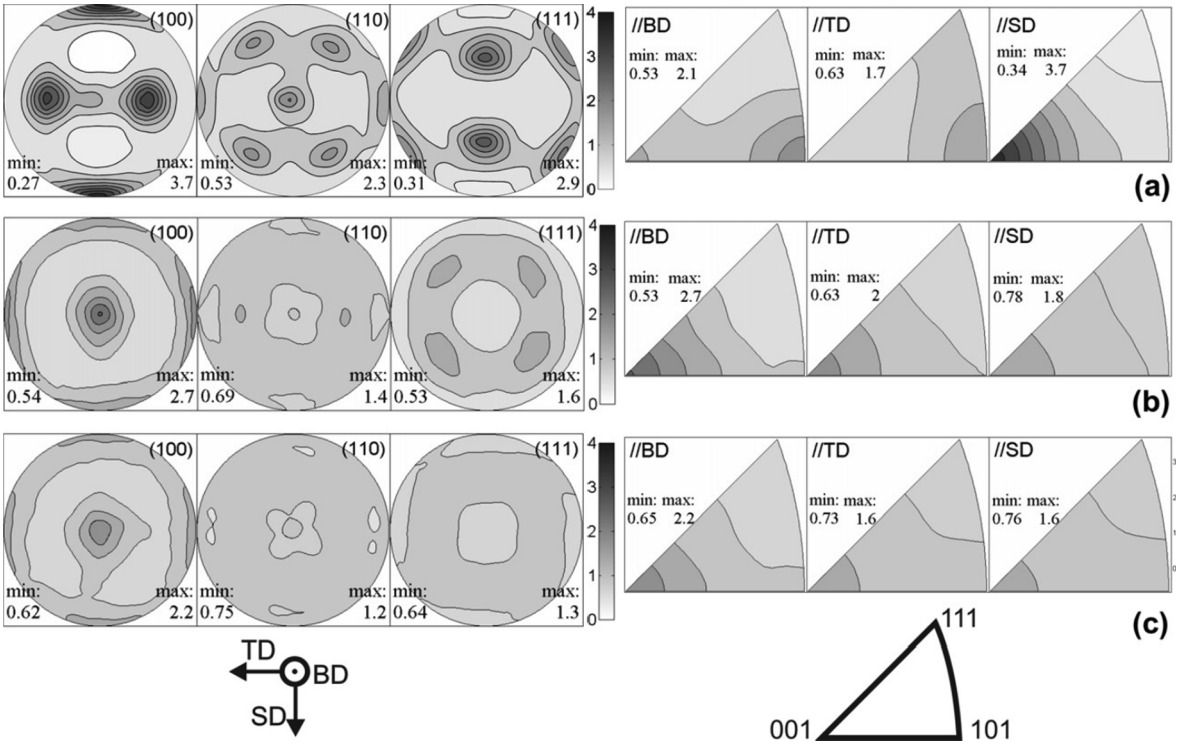

Fig. 25. Contour pole figures and inverse pole figures of AlSi10Mg SLM parts produced using (a) unidirectional, (b) bidirectional and (c) chessboard laser scanning strategies. The ⟨1 0 0⟩ texture along the scanning direction can be decreased when inter- or intra-layer scanning rotations are used [40].

and AlSi10Mg [130,156] as well as solution heat treatment of AlSi12 [273] and precipitation hardening (T6 – solution heat treatment followed by water quenching and artificial ageing) of AlSi10Mg [123,124,162,172].

Studies on the crystallographic texture evolution during heat treatment of SLM Al alloys are scarce. Takata et al. [130] compared the texture of AlSi10Mg in the as-built and annealed/ solution-treated conditions. Aside differences in the sub-structure of the alloy, no significant differences in terms of Al grain shape and morphology and texture was reported, suggesting that Si particles might act as pinning sites for Al grains and heat treatments would only lead to a recovery of the structure.

8. The performance of SLM Al alloys

Essential to cope with SLM's growing popularity [204], the assessment of the feasibility of its use for structural parts through mechanical characterization is ever increasing. Material-laser interaction and rapid solidification lead to microstructural features that can potentially yield enhanced material properties [280]. However, the presence of defects from the process, if not sufficiently controlled by the process parameters, may as discussed deleteriously influence the mechanical behaviour [172].

Anisotropy is affected by the material's crystallographic texture [254,281], which is attributed to the process parameters [40,254]. The build direction is claimed to affect the mechanical properties, with better properties for horizontal samples [29,172,254] since the density of dislocations is dependent on the build direction [281]. However in some cases, no significant effect was observed under tension [87] or in fatigue behaviour [172]. This section will cover a range of mechanical properties that have received researchers' attention in the literature.

8.1. Nano-hardness

The extremely fine hierarchal microstructures produced by SLM triggered researchers' interest in studying the local mechanical properties of the material, *i.e.* at the nano-scale level. Published research [282] used nanoindentation, a depth sensing indentation technique, to show that the hardness profile across an individual AlSi10Mg melt pool is uniform whilst being significantly higher than that of the cast material. Everitt et al. [171] further supported these findings by mapping the hardness profile across the SLM material and the cast substrate, as shown in Fig. 26(a–b). Zhao et al. [169] reported similar results for the same alloy reinforced with SiC, where the nano-hardness was uniform between the melt pool boundary and core but it significantly increased (by nearly three folds) when indenting a reinforcing structure. Conversely, Prashanth et al. [192] reported spatial variation in $Al_{85}Nd_8Ni_5Co_2$ processed by SLM, since the resultant microstructure was more of a composite-like microstructure of an Al matrix reinforced with three types of

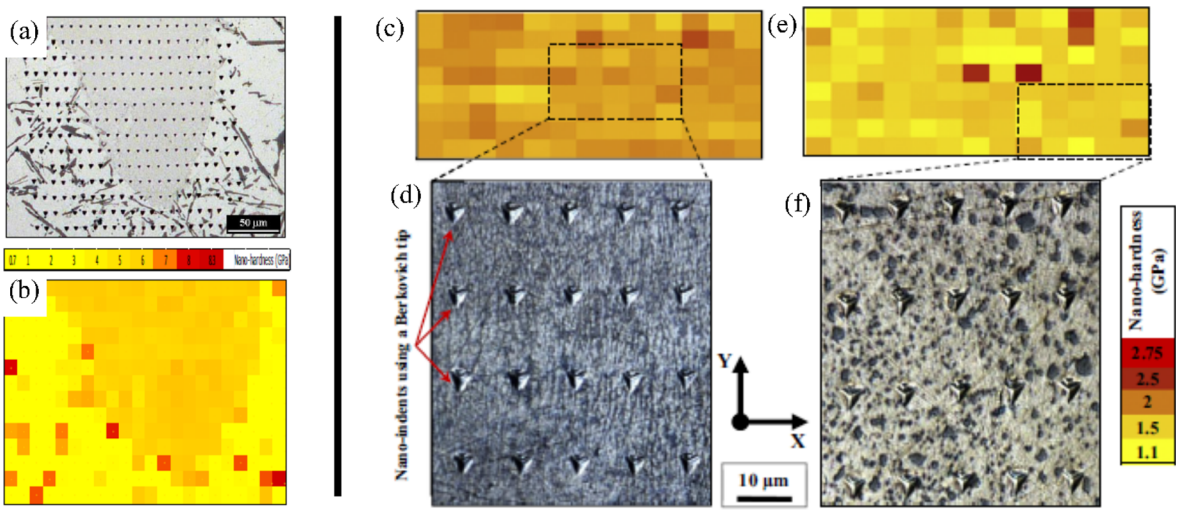

Fig. 26. Nano-hardness profile mapped on (a) an AlSi10Mg single track created on a cast AlSi12 cast substrate showing (b) the uniform profile across the SLM material versus the non-uniform profile in the cast counterpart [171]. A comparison is presented between the nano-hardness profile of (c–d) the as-built material and (e–f) the heat treated material [124].

reinforcements, each returning a different nano-hardness value. This indicates how the constituent elements in each alloy and their response to SLM processing controls the local mechanical properties through changes in the produced microstructure and distribution of the various phases present in the material.

The uniform profile across the SLM material was attributed to the extremely fine microstructure coupled with the fine dispersion of the alloying elements [38]. This was contrasted to the coarser microstructure in the cast material, which showed spatial variation dependent on the indented phase. Everitt et al. [171] also reported a uniform hardness profile across the overlapping melt pools in an individual layer. As for the nano-hardness profile across multi-layered samples, Fig. 26(c–d) shows a uniform profile [124]. It can be concluded that the overlap of the melt pools to construct the 3D structures does not significantly affect the local mechanical properties of the material, *i.e.* the re-melting and solidification of the material does not cause a trend in its local hardness despite the variation in grain size within each melt pool.

Qi et al. [135] adopted similar methods in [124] to study the mechanical properties variation in AA-7050, in that study the uniformity of the material, as indicated by the nano-hardness profile was seen to depend on the melting mode to an extent. In their study, conduction mode melting was seen to produce a higher nano-hardness, with a more uniform profile. An increase in the nano-hardness in keyhole samples towards the bottom of the melt pool was attributed to the presence of more fine grains in that region, which can enhance the material's resistance to deformation through increased grain boundary area. However, these conclusions were drawn based on a single line of indentations rather than an array, so further investigations may be needed to support this finding. Uzan et al. [275] used nanoindentation to show how shot peening induces an increase in the hardness of the sample near the surface.

The effect of the microstructural changes with heat treatment (following a conventional T6 procedure) on the material's local mechanical properties is demonstrated in Fig. 26(e–f). The formation of Si particles through spherodisation and their coarsening with thermal treatment led to spatial variation in the material's nano-hardness with higher hardness returned by the indentations coincident on Si particles. Furthermore, an overall softening was observed upon heat treatment [124,167]. Annealing had a more pronounced softening effect [283] with the reason behind this softening being discussed in the next section.

8.2. Micro-hardness

Micro-hardness is commonly used to investigate the mechanical properties of SLM Al parts due to the relative ease of the test, as well as small sample sizes requirements, making it a quick way to assess mechanical properties. Enhanced micro-hardness has been reported for SLM AA-2xxx [210] compared to the traditionally produced counterparts; the micro-hardness of the as-built AA-2024 was ~37% higher than the equivalent 2024-O sheet but ~20% less than the T6-treated conventionally-processed sheet [191]. A summary of the micro-hardness results from the literature are presented in Fig. 27 and listed with further relevant details in Table 3 where the variation in results between studies is clear. This is typical of SLM materials; the reasons behind this variation includes the use of different machines, different combinations of process parameters, and different quality starting powder, which leads to various degrees of densifications. Nevertheless, all the listed studies reported properties that are either similar to or even harder than the conventionally-processed counterparts.

The summary in Table 3 and the map in Fig. 28 show how the various heat treatment procedures (annealing, solution heat treatment, and solution heat treatment followed by ageing (T6)) softened the material significantly. This is similar to the trend in the nanoindentation section. To understand this trend, the authors [162] considered the various factors contributing to strengthening both the as-built and heat-treated AlSi10Mg samples. In the as-built material there is: (i) the strengthening driven by grain size

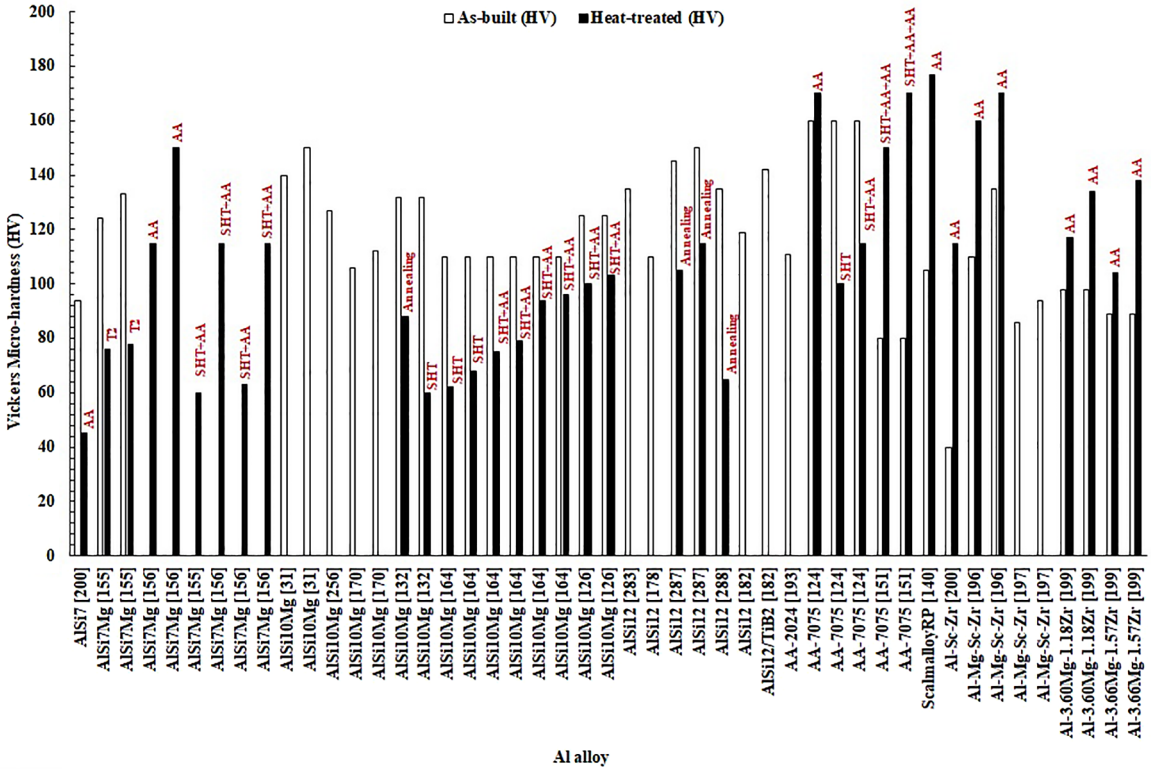

Fig. 27. Some of the micro-hardness data from the literature for various SLM Al alloys in their as-built and heat treated conditions.

refinement, (ii) the solid solution strengthening, and (iii) the dislocation strengthening as the dislocations hinder each other's motion. Factors (ii) and (iii) still hold in case of the heat-treated material (T6-procedure); the main difference is that the grain size coarsens upon heat treatment, but this is counteracted by Orowan strengthening due to the formation of Si spheroids where due to the stronger effect of grain size refinement, the as-built material remains harder than the heat-treated one. Softening was more pronounced with annealing due to the reduction in the dislocation density through annihilation of dislocations in addition to the microstructural coarsening. A similar effect was seen for the T6 heat-treated AA-7075, according to Table 3. Material softening by T6 heat treatment was not the case for ScalmalloyRP as an enhancement of 69% was achieved due to the formation of a large amount of Al_3Sc [138]. This was also reported for Al alloys modified by Zr additions either with or without Sc [194,197].

Takata et al. [168] investigated the effect of the sample size on the micro-hardness of AlSi10Mg through fabricating samples with thicknesses ranging from 0.1 to 10 mm; the hardness decreased slightly as the samples got smaller. However, this was not very significant in the presented data since the change in hardness was from 112 HV to 107 HV across the investigated range of thicknesses. This can be correlated to the rate of solidification and its change with the sample size; the smaller the part the slower the rate of solidification imposed. This suggests a coarser microstructure that can potentially lead to a softer material.

Although the as-built material has higher hardness compared to the conventionally-processed material, the necessity to develop new tailored heat treatment procedures that can suitably alter the microstructure to further harden the material cannot be overlooked. There is the hypothesis that the as-built material is already in a peak hardened state as precipitation occurs during processing and therefore, any further T6 heat treatment causes over-ageing. The academic community would benefit from a dedicated study for this matter. Atomic probe tomography could be helpful in investigating the precipitation behaviour defining the types of precipitates forming, if any.

8.3. Tensile behaviour

The exceptionally fine microstructure in SLM Al parts improves their tensile strength. Some of the tensile properties from the literature are presented in Table 4 and Fig. 29. The tensile strength of AlSi10Mg [29,87,124,254] and AlSi12 [176,179,287] have been repeatedly reported to be better than their conventionally-processed counterpart. The improved strength is believed to be due to the presence of sub-grain boundaries and inter-dendritic Si that hinder the motion of dislocations [120]. At elevated temperatures, the AlSi12 alloy showed a slight reduction in the tensile strength coupled with a marginal improvement in the ductility, putting the alloy forward for use in applications that involve high temperature environments [288]. Nevertheless, it is worthwhile noting that it was not clear in that study for how long were the samples maintained at high temperature. Comparing this behaviour to the material's creep behaviour was also missing.

Table 3
Micro-hardness of SLM Al parts and the effect of heat treatment.

Material	Heat treatment	Details	As-built (HV)	Heat-treated (HV)	Source
AlSi7	AA	300 °C – (0.1–168 h)	94	45	[198]
AlSi7Mg	T2	300 °C – 3 h	124–133	76–78	[153]
	AA	165 °C – 0.01–60 h	–	115–150	[154]
	SHT + AA	535 °C – 1–8 h 165 °C – (0.01–60) h	–	60–115	[154]
	SHT + AA	535 °C – 1–8 h 180 °C – (0.01–60) h	–	63–115	[154]
AlSi10Mg	–	–	140–150	–	[29]
	–	–	127	–	[254]
	–	–	106–112	–	[168]
	Annealing	300 °C – 2 h	132	88	[130]
	SHT	530 °C – 6 h	132	60	[130]
	SHT	520 °C – (1–4) h	110	62–68	[162]
	SHT + AA	520 °C – 1 h 160 °C – (6–12) h	110	75–79	[162]
	SHT + AA	520 °C – 4 h 160 °C – (6–12) h	110	94–96	[162]
	SHT + AA	520 °C – 1 h 160 °C – (6–7) h	125	100–103	[124]
AlSi12	–	–	135	–	[284]
	–	–	110	–	[176]
	Annealing	300 °C – 3 h	145–150	105–115	[285]
	Annealing	450 °C – 6 h	135	65	[286]
	–	–	119	–	[180]
AlSi12/TiB_2	–	–	142	–	[180]
AA-2024	–	–	111	–	[191]
AA-7075	AA	150 °C – 6 h	160	170	[122]
	SHT	470 °C – 2 h	160	100	[122]
	SHT + AA	470 °C – 2 h 150 °C – 6 h	160	115	[122]
	SHT + AA + AA	470 °C – 1 h 110 °C – 5 h 150 °C – 14 h	80	150–170	[149]
ScalmalloyRP	AA	325 °C – 4 h	105	177	[138]
Al-Sc-Zr	AA	300 °C – (0.1–168 h)	40	115	[198]
Al-Mg-Sc-Zr	AA	300 °C – 12 h	110–135	160–170	[194]
	–	–	86–94	–	[195]
Al-3.60Mg-1.18Zr	AA	400 °C – 0.5–144 h	275	320–410	[197]
Al-3.66Mg-1.57Zr	AA	400 °C – 0.5–144 h	300	360–420	[197]

Heated build-plates significantly reduce the strength without affecting the ductility [151]; since a lower thermal gradient produces a relatively coarser microstructure. The range of values reported for each material can be quite broad due to several reasons including, but not limited to, the influence of the process parameters and the variation from a machine to another plus the discrepancies in the raw material used as well as the build orientation. This applies to the as-built and heat-treated properties.

Despite having higher strength, the brittleness cannot be overlooked. Heat treatments such as annealing recovered a fraction of the ductility [187] at the expense of the strength although the microstructure does not change significantly [130]. This is supported by the results documented in Table 4. The reduction in strength can be attributed to the reduced solid solution strengthening and recovery, which coarsens the microstructure detangling the arrays of dislocations.

A significant amount of residual tensile stress was measured for Si in as-built AlSi12 that was relaxed by solution heat treatment. These stresses alongside the ultra-fine-grained Al and the nano-sized Si mean that there is a high dislocation density, which eases diffusion during heat treatment leading to enhanced recovery, which is advantageous for the material's ductility or capability for stable plasticity [273]. Solution heat treatment increased the ductility of AlSi12 by 400% at the expense of its ultimate tensile strength (UTS) which dropped by 46% [273]. The conventional T6 heat treatment, on the other hand, provided AlSi10Mg with a push of ductility (180% increase) without significantly losing its strength (12% reduction) [124]. Therefore, it can be surmised that the T6 heat treatment can yield a compromise between the strength and ductility.

Rao et al. [151] reported anisotropy with the build orientation in A357 parts in ductility but not strength. This agrees with results published by Read et al. [87] for AlSi10Mg who showed that horizontally produced samples exhibited increased ductility. In addition to agreeing with these findings, Takata et al. [130] showed that the AlSi10Mg vertical samples also tend to have lower yield strength. After heat treatment via either annealing or solution heat treatment, there was no direction-dependence any more [130]. This is due to the phase transformation during heat treatment where the melt pool structure is cancelled and replaced with a more homogeneous composite-like structure without distinct directionality in the microstructure.

The direction of loading with respect to the build orientation plays a vital role on the performance of the material under tensile loading. Given the columnar grain morphology, less resistance will face crack propagation when loading is parallel to the build

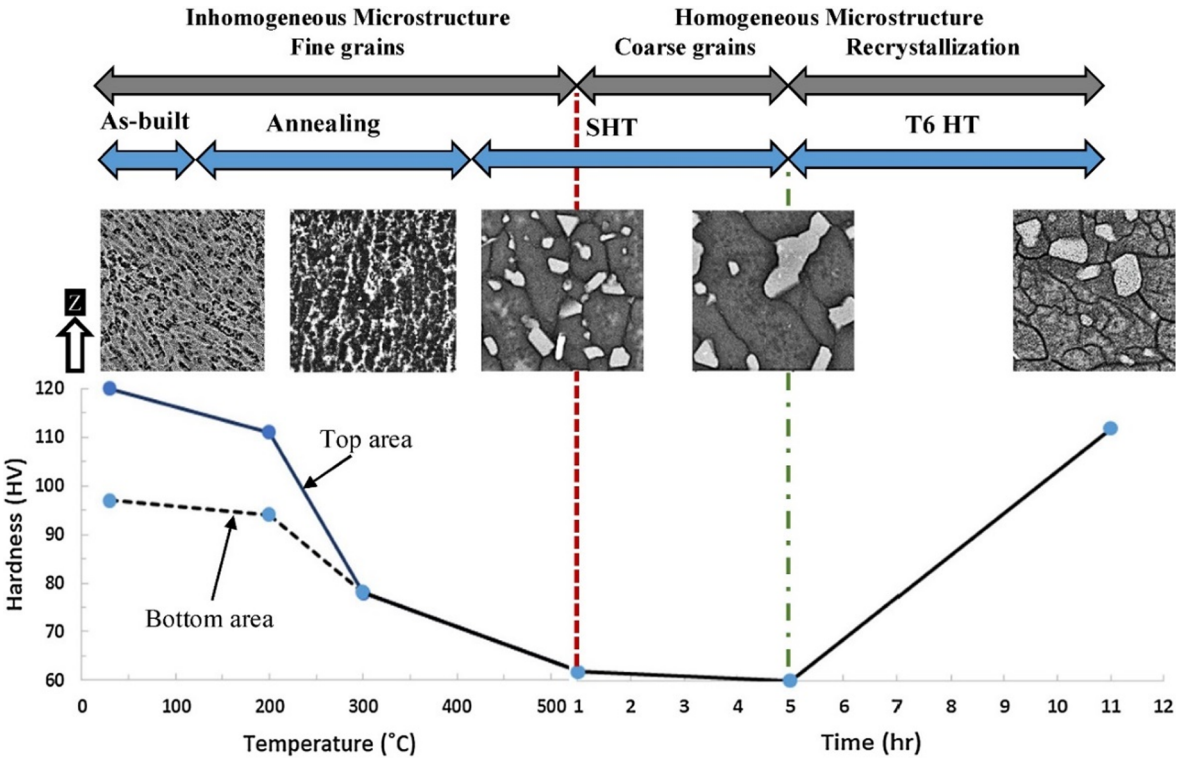

Fig. 28. The effect of various heat treatment procedures on the micro-hardness of SLM AlSi10Mg [224].

orientation. Nevertheless, the morphology of the irregularly shaped pores in the parts can also affect the strength. The lack-of-fusion pores typically resemble the shape of the melt pool, as shown in Fig. 12; they have an ellipsoidal shape with their long axes perpendicular to the build orientation. Loading along this long axis will eventually close the pore, mainly without material diffusion. However, loading perpendicular to the long axis will result in opening this pore and delamination occurring across the plane where it lies.

As for the high strength alloys, micro-cracking has been shown to lead to poor mechanical properties, as reported for AA-7075 [111]. Functionalising the surface of the powder with Zr nano-particles eliminated cracking and refined the microstructure leading to tensile properties that are comparable to the wrought material [111]. The strength and ductility of AA-2024 was improved over the non-heat-treated cast samples but fell short of the wrought aged equivalent [191]. Sc-containing alloys, such as ScalmalloyRP, yielded ultimate tensile strength values exceeding 530 MPa with elongation percentages up to 14% (aged) [138]. Furthermore, the anisotropy with the build orientation was insignificant [138,139]. The high strength in this alloy was attributed to the supersaturation of Sc as well as the precipitation of Al_3Sc, which hinders the dislocations' motion through pinning [245]. Adding increments of Zr to Al-Cu-Mg-Mn alloys enhanced the tensile strength along with improving the material's ductility [196]. Furthermore, Al-Mg alloys strengthened by Zr with no Sc exhibited outstanding tensile properties due to the formation of Al_3Zr precipitates (cuboidal [137]), close to the Sc-containing ones without the extra cost associated with using Sc [197]. Sub-micrometer particles and nanosized precipitates of Al_3Zr led to grain refinement, preventing hot tearing during rapid solidification and enhancing the strength through the Hall-Petch effect. This was coupled with material's hardness that is significantly higher than the Sc-containing alloys. Further refinement was realised by laser rescanning driven by a shallower melt pool forming by the second scan due to the reduced laser absorptivity of the consolidated metal [137]. It is worth noting that the Zr-modified alloy was characterised by higher ductility than the Sc-modified alloys [197]. Another approach to remarkably strengthen the Al-Si alloys whilst benefitting from their relative ease of processing by SLM is tweaking their chemical compositions, such as the work by Pozdniakov et al. [292]. By means of heat treatments, this alloy offered a compromise between strength and ductility.

Failure under tensile loading occurs along the boundaries between the melt pools for samples built in the vertical orientation [124,130], as shown in Fig. 30(a), *i.e.* fracture occurs through the melt pools' detachment. This is the area where coarser grains were observed, *i.e.* softer regions and less grain boundaries obstructing the dislocation motion. The finer microstructure in the as-built specimens alongside the more homogeneous dispersion of the alloying elements (Fig. 30(a) and (c)) justifies the higher tensile strength. Si provides the material with strain hardening capability so the cracks initiate within the softer α-Al grains. Therefore, the distribution of Si in the material controls the properties directional-dependence. In the case of samples built in the horizontal orientation, cracks initiated at random defects and propagated through the melt pools (Fig. 30(e)) [132].

After heat treatment (Fig. 30(b) and (d)), cracks initiated and coalesced at the Si particles [124]; the favoured sites for crack initiation. The spherical morphology of the Si particles is much better, in terms of the material's ductility, than the rod- or needle-like morphology in the conventionally-processed material that act as stress concentrators reducing ductility [273].

Table 4
Tensile properties of SLM Al parts and the effect of heat treatments.

Material	Ref	As-built			Heat treatment	Heat-treated		
		UTS (MPa)	Yield strength (MPa)	Elongation (%)		UTS (MPa)	Yield strength (MPa)	Elongation (%)
AlSi7Mg, A356	[153]	368	–	9.2	T2	226	–	12.8
	[242]	380–390	200–225	12.5–17.5	Annealing	200–420	125–250	27–30
					T6	270–275	190–210	7–13
AlSi10Mg	[111]	315	209	7.3	–	–	–	–
	[87]	316	231	1.1	–	–	–	–
	[124]	333	268	1.4	T6	292	239	3.9
	[289]	340–370	160–220	4–7	–	–	–	–
	[245]	350–380	250	8	–	–	–	–
	[290]	384	241	6	HIP	141	115	35
	[167]	446	270	8	Annealing	273	170	15
					T6	214	164	11
	[174]	–	–	–	Stress-relief	358	204	7.2
AlSi12	[273]	350	225	5	SHT	200	100	25
	[288]	375	260	2.8	–	–	–	–
	[291]	425	101	12.1	–	–	–	–
	[176]	342–368	221–224	1.5–4.8	–	–	–	–
	[179]	380	260	3	Annealing	150	95	15
	[185]	190–418	150–220	0.98–4.38	–	–	–	–
	[186]	380	240	2.8	–	–	–	–
AlSi11CuMn	[292]	470	350	1.8	Annealing	434	242	4.4
	[292]	470	350	1.8	T6	354	288	5.4
AA-2024	[191]	402	276	6	–	–	–	–
AA-7075	[111]	25	–	0.4	–	–	–	–
	[150]	42–203	–	0.5	T651	45–206	–	0.2–0.5
ScalmalloyRP	[139]	400–430	270–310	–	–	–	–	–
	[245]	490	470	8.2	–	–	–	–
	[138]	–	–	–	Ageing	520	500	14
Zr/Al-Cu-Mg-Mn	[196]	411–494	256–484	4.8–11.8	–	–	–	–
Al-Mg-Sc-Zr	[194]	300–410	405	1.5–5.0	T6	470–500	357	1.5–2.5
Al-Mn-Sc	[198]	460	431	21.5	AA	550	570	18.1
Al-3.60Mg-1.18Zr	[197]	287–292	220–221	25.6–29.0	AA	382–386	350–353	17.1–18.6
Al-3.66Mg-1.57Zr	[197]	329–332	282–290	24.0–25.2	AA	383–389	349–365	19.5–23.9
Al-6Zn-2Mg-1(Sc + Zr)	[199]	386	283	18.4	T6	435	418	11.1

8.4. Compressive behaviour

Investigating the compressive behaviour of Al alloys is not generally common due to the material's ductility. Such alloys normally buckle or barrel under compressive loading, which can complicate the analysis of the stress-strain curves collected from compression tests. For example, internal work by the authors has shown that the sample size along with the length-to-diameter ratio affect the material's response to compressive loading, as shown in Fig. 31. The samples with a length-to-diameter ratio of 3 buckled. A length-to-diameter ratio of 2, on the other hand, led to barrelling. The change in sample size, therefore, influences the material's yield strength, ultimate strength, and Young's modulus.

There is no strong driving force for assessing the compressive behaviour of these alloys from an application's perspective and this is not any different for the SLM-produced parts. The amount of studies focussing on this aspect is quite limited with most of the attention directed to investigating the compressive behaviour of Al lattice structures.

The characteristic microstructure also yielded compressive behaviour surpassing that of the conventionally-processed counterpart. Compressive yield strength three times that of the cast material was reported for AlSi10Mg [124]. The use of reinforcements to improve the compressive strength was evidenced in an AlSi12-TNM composite that showed an enhanced compressive strength at the expense of ductility [293]. The compressive strength of AlSi12 was also improved by adding TiB_2 particles without affecting the material's ductility through eliminating the crystallographic texture [180].

The compressive behaviour of the high-strength alloy AA-7075 was found to be inferior to the conventional counterpart, despite the enhancement achieved by heat treatment [122]. It is worth noting that this result was for AA-7075 with 4% Si addition to reduce cracking; worse behaviour would be expected if the cracks were not reduced beforehand. An AlMg6.5 alloy modified by Sc and Zr additions yielded enhanced compressive strength values that changed with changing the energy density [193]. The $Al_{85}Nd_8Ni_5Co_2$ alloy yielded superior compressive strength (1.08 GPa) that was retained after heat treatment and when tested at elevated temperatures [192]. This was attributed to the formation of a composite-like material after SLM process in the form of an Al matrix reinforced with $AlNd^3$, Al_4CoNi_2, and $AlNdNi_4$, these reinforcements forced crack deflection under loading.

Although the compressive behaviour of Al alloys has not received much consideration previously, it is becoming more important now as Al alloys are increasingly being used in SLM produced lattice structures, where compressive strength is often of interest. Overall, it can be concluded that the fact that the compressive performance of parts fabricated by SLM is superior to the conventionally-processed is attractive for various applications.

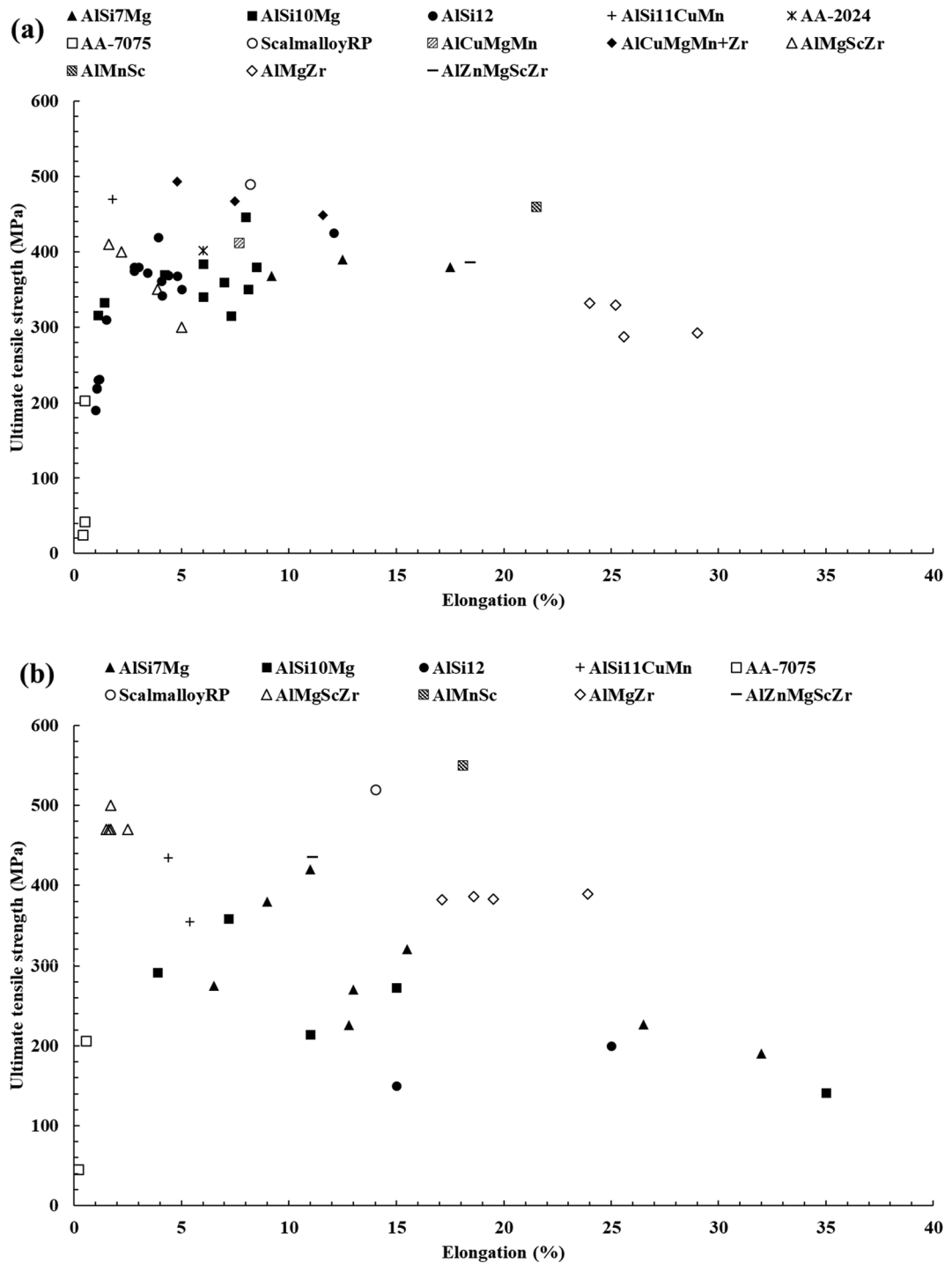

Fig. 29. Tensile strength versus elongation per cent for some of the Al alloys processed by selective laser melting in the as-built and heat-treated condition.

8.5. Fatigue performance

The fatigue performance of SLM materials usually falls short of the conventionally-manufactured counterparts [294]. This has been attributed to various factors in the literature as fatigue performance is prone to common SLM defects such as porosity, residual stresses, and surface roughness [281,295,296] specially for cast alloys due to second phase particles [297]. These act as stress concentrations depressing the fatigue life through crack nucleation and growth [172,295,297–299]. However, acceptable fatigue

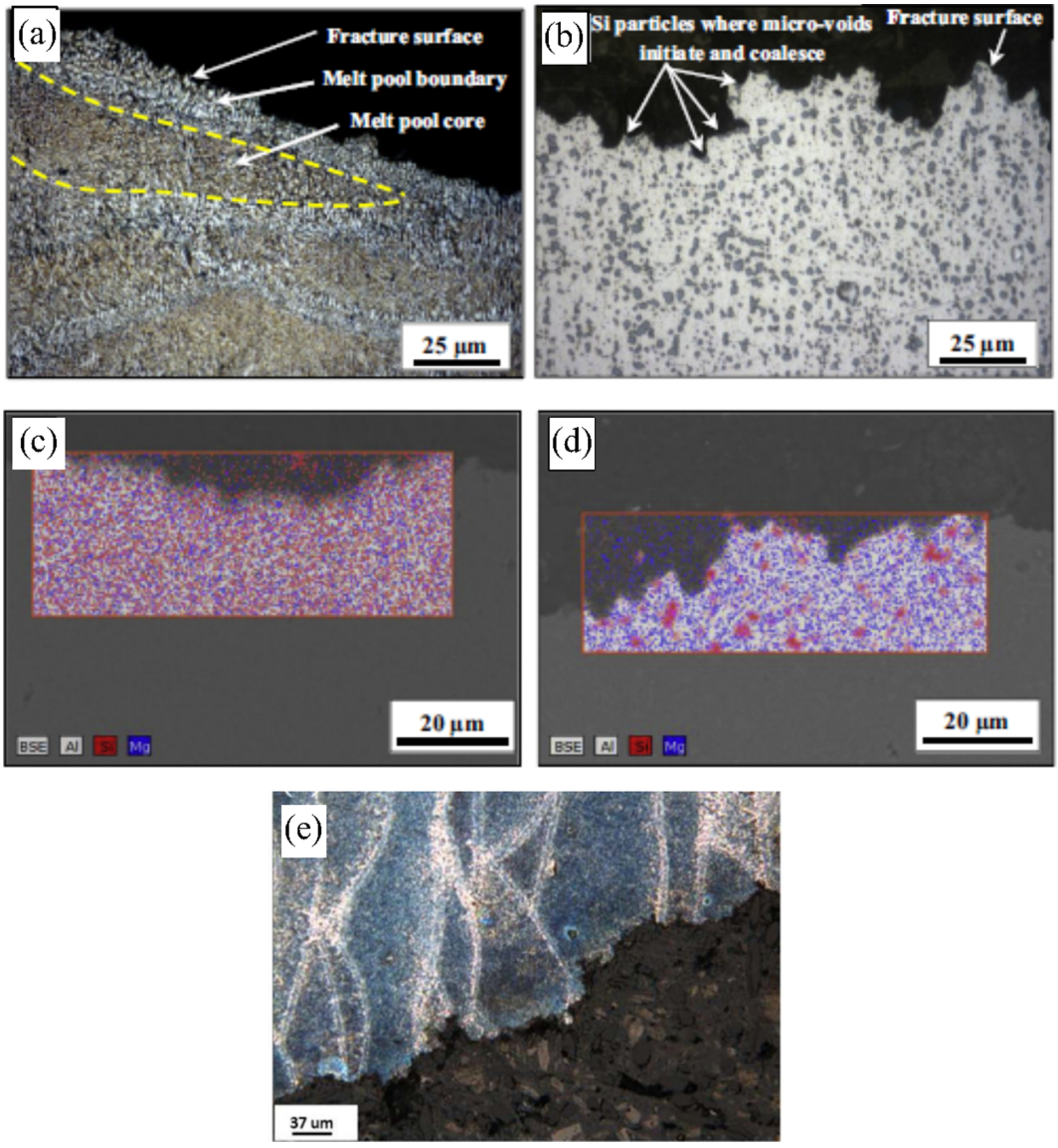

Fig. 30. Cross-sectional views of fracture surfaces from SLM AlSi10Mg tensile specimens comparing the (a) as-SLM sample built in the horizontal orientation along with its corresponding EDS map in (c) to the heat-treated sample in (b) and (d) [124]. The fracture surface of an as-SLM sample built in the horizontal orientation is shown in (e) [132].

strength was observed in SLM parts from Al alloys for the finer microstructure developed in the material, as demonstrated in Fig. 32 where the S-N curves from various studies are plotted in comparison to the performance of the conventionally-cast material. The variability between parts fabricated from different powders on different systems using a wide range of process parameters leads to a significant variation in fatigue properties.

Internal pores containing un-bonded powder have been observed in SLM parts from alloys such as AlSi10Mg [32,87] and Al6061 [145], among others. Although they are reasonably small, *i.e.* they might not considerably reduce the load bearing area under tension [87], they might have a more pronounced effect under cyclic loading. As the size of the defect grows larger, the fatigue life is shortened [170]. Furthermore, oxides forming at these pores or randomly scattered across the samples lead to premature failure. These oxides and pores are commonly observed at the crack initiation region (see Fig. 33). The formation of these oxides is believed to be due to laser spatter (see Fig. 14), oxidised vapour, and the oxide layer originally on the powder used in the process [123,170].

Surface open pores or sub-surface porosity also leave the part susceptible to premature failure under cyclic loading. Damon et al. [270] observed a ring of porosity close to the sample's surface. Work by the author [123] has reported sub-surface pores to surface upon machining increasing the scatter in data, which is usually performed to improve the surface roughness of SLM samples. These pores were found to be points where cracks initiate and propagate, eventually causing failure. Yang et al. [152] compared samples

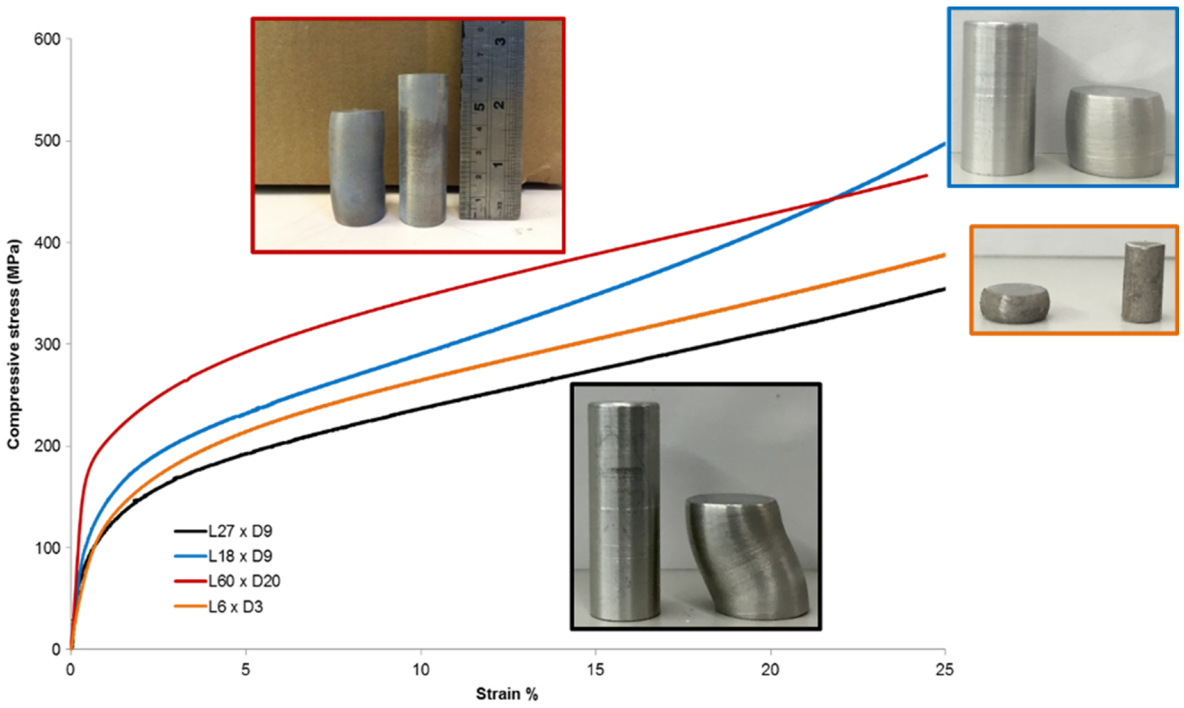

Fig. 31. The various failure modes of SLM AlSi10Mg based on the sample size.

with machined surfaces leaving some residual sub-surface porosity to ones presumably without sub-surface porosity. The latter showed better fatigue life while both of them exceeded the life of the as-built samples. Therefore, the sub-surface pores play a detrimental effect in the fatigue life of SLM samples. Siddique et al. [184] recommended scanning the contours of the parts more than once for re-melting to reduce the probability of porosity formation in these regions.

The fatigue performance is also affected by some of the process parameters, such as the build orientation and the build-plate temperature, as the fatigue strength of a material is directly related to its ductility. Given that the ductility of the SLM material showed evidence of anisotropy based on the build orientation, this was also expected for the material's fatigue resistance. This was confirmed by Mower and Jong [249], Tang and Pistorius [170], and Awd et al. [245] who reported the fatigue life of samples built in the horizontal orientation to be longer than those built in a vertical orientation.

Incorporating supporting structures in parts with overhangs improves the fatigue strength of the material, where supports aid in increasing the cooling rate, thus imposing the development of a finer microstructure [300]. The build-plate temperature was not seen to affect the fatigue strength of SLM AlSi10Mg by Brandl et al. [172] but rather it reduces the scatter in data. Heating the build-plate also reduced the scatter in data for AlSi12 [182]. An enhancement in fatigue strength was also observed (see Fig. 32(b)), negating an earlier observation by Siddique et al. [185]. The reasons behind this discrepancy is not clear.

Fatigue life of parts can be improved by several methods such as sand blasting [301], shot peening [270,275], rolling, burnishing [298], heat treatments, and hot isostatic pressing [295,296]. Shot peening using steel and ceramic balls improved the fatigue strength of AlSi10Mg, exceeding the performance of the conventionally-processed samples (see Fig. 32(c)). Brandl et al. [172], further supported by Aboulkhair et al. [123], have shown that a conventional T6 heat treatment remarkably improved the performance (see Fig. 32 (d)) through material softening [162], *i.e.* increasing the ductility [124]. Si dendrites transformation into spheroids hinder crack initiation and propagation [172]. The enhancement by heat treatment was effective for samples both with and without machined surfaces. Aboulkhair et al. [123] have also shown that the effect of heat treatment surpasses that of machining, *i.e.* improved fatigue performance can be achieved through heat treatment on its own. This is a promising result for the production of net-shapes since post-process machining might not always be feasible, such as in the case of geometrically challenging topology optimised parts and lattice structures where shape complexity is high. The combined effect of heat treatment with a surface treatment such as sand blasting or shot peening was insignificant compared to the effect of surface treatment on its own [301]. The discrepancy between the magnitudes of the effect of surface treatments on the fatigue performance of SLM parts can be attributed to the variability in quality of samples produced using different machines and process parameters. The post-process treatment, hot isostatic pressing (HIP), caused fatigue performance deterioration in both AlSi10Mg [290] and AlSi12 [184] samples.

The high strength Al alloys (e.g. AA-7075) showed a much worse fatigue behaviour when compared to the conventionally-processed material [150]. This is due to the high cracking density in the material, as explained in earlier sections.

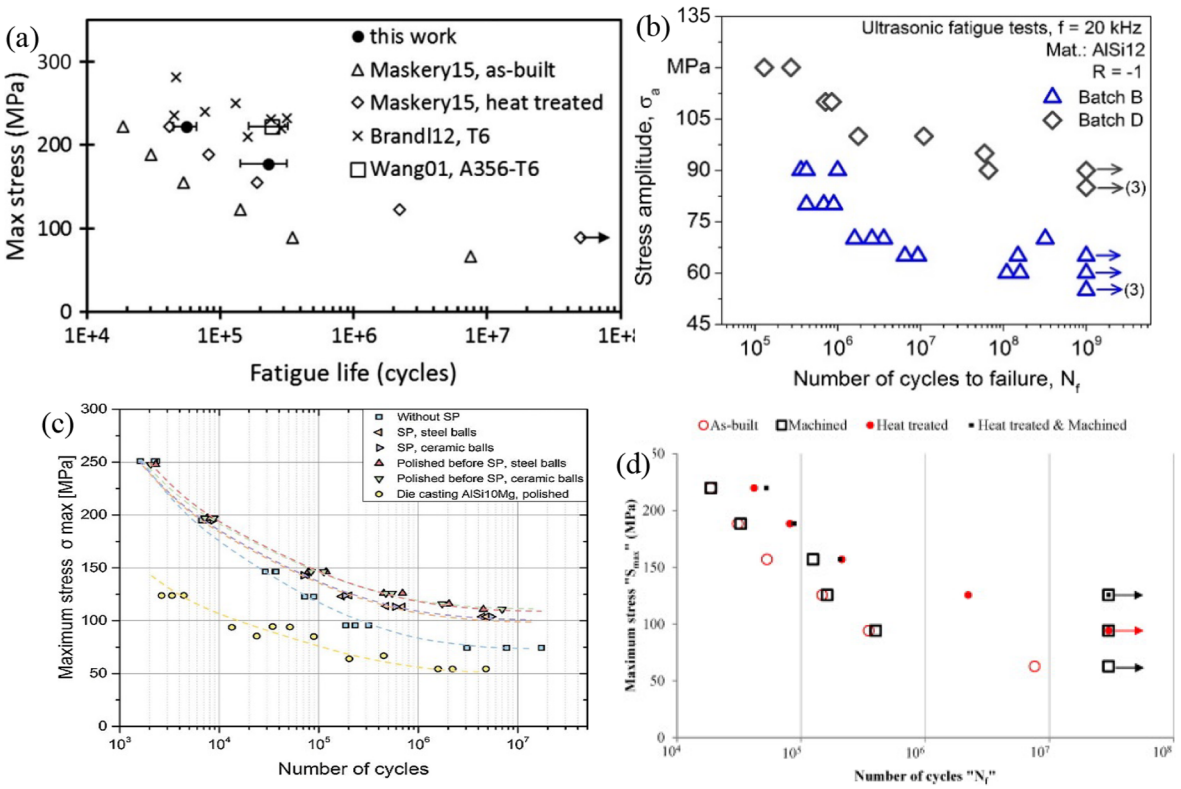

Fig. 32. (a) Some of the fatigue data in the literature for SLM AlSi10Mg. (b) S-N curves for SLM AlSi12 showing the effect of build plate heating were batch B is manufactured without build plate heating and batch D had a build plate temperature of 200 °C [182]. (c) S-N curves demonstrating the effect of shot peening on SLM AlSi10Mg samples [275]. (d) S-N curves for SLM AlSi10Mg showing the effect of heat treatment and machining on the material's fatigue behaviour [123].

8.6. Fracture toughness

The fracture toughness of a material defines its ability to resist crack propagation. A material's toughness is directly proportional to its ductility. However, the toughness of the SLM material markedly surpassed that of the cast material by nearly 3 or 4 times [181] despite having lower ductility. This is driven by the presence of inter-dendritic Si at the boundaries of the Al cells that hinder the crack propagation. Also, the circular morphology of the melt pools and the favoured crack propagation at the melt pool boundaries forces the crack to change its path quite frequently, which is translated in higher fracture toughness. The anisotropic microstructure produced by SLM has therefore influenced the fracture toughness of samples built in various build orientations; the vertical samples having the lowest fracture toughness [302].

Annealing reduced the fracture toughness of the material although its ductility improved and strength decreased. The decomposition of the melt pool boundary's structure is believed to be the reason behind the lower resistance to crack propagation, *i.e.* lower fracture toughness. Nevertheless, the toughness of the heat-treated material was still double that of the cast counterpart [181].

It can be concluded that SLM offers the possibility of fabricating parts benefitting from enhanced strength and ductility, concurrently. This combination of properties is an advantage unachievable using the conventional processing techniques.

8.7. Creep resistance

A material's creep resistance is an assessment of its time-dependent mechanical performance at elevated temperatures. The temperature limit above which creep becomes a design consideration is material-dependent. Because Al has a relatively low melting temperature, it is known to creep at around 200–300 °C. Read et al. [87] reported the creep resistance of SLM AlSi10Mg parts to be within the predictions for this material, *i.e.* comparable to the conventionally-processed material, in agreement with [174]. As expected, the creep resistance deteriorated with increasing the testing temperature or the load/stress applied. Creep resistance deteriorates at higher temperatures as recovery can start to take place.

One of the approaches that improves creep resistance is to increase the obstacles that limit the dislocation motion. This could explain the improved creep resistance observed in the abovementioned study; since SLM produces parts with a high dislocation density. These dislocations are expected to entangle and act as obstacles to one another, improving the resistance to deformation.

Contrary to the tensile behaviour, creep resistance is normally enhanced for larger grain-sized materials. This is because the larger

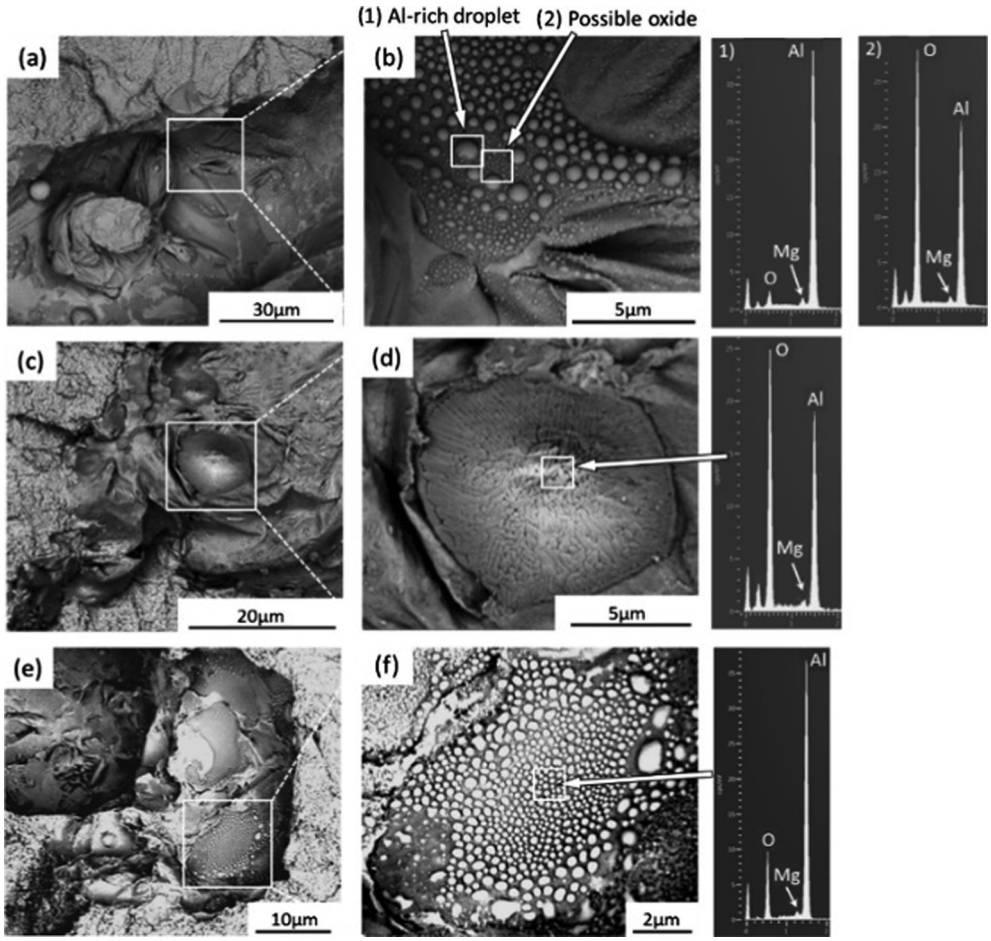

Fig. 33. Evidence for the presence of oxides in the SLM sample at the crack initiation region that promotes pre-mature failure under cyclic loading [170].

grain size depresses the diffusion rate and limits grain boundaries sliding, which are two phenomena critical for creep. The presence of precipitates in the material also increases the resistance to creep, which is the case for age hardenable Al alloys. However, whether this will hold for SLM materials or not is still unknown given the converse effect age hardening had on the other mechanical properties discussed earlier. Solid solution strengthening has a similar effect.

The work on creep resistance of SLM Al in the literature is quite superficial. Studies investigating the above mentioned approaches for enhancing creep resistance are still lacking.

8.8. Impact resistance

In the SLM field, investigating the impact resistance behaviour is probably more relevant for lattice structures. This is driven by their potential for use as an impact-protective mechanism and within energy absorption applications.

The impact resistance of a material is typically assessed through measuring the impact energy experimentally; the amount of work needed to fracture a specimen. Upon impact, the energy is absorbed by the sample up to the yield point, after which plastic deformation starts. As the material reaches the threshold and becomes unable to absorb more energy it fractures. The dynamic behaviour of a metallic sample is quite complicated and is governed by the competition between the material's strain hardening capacity (up to the peak flow stress) followed by thermal softening [303].

Similar to the other types of mechanical strengths discussed up to this point, the impact resistance of SLM parts was superior to the conventionally-processed equivalents. Although this was not expected as limited ductility usually goes hand-in-hand with inferior impact resistance. The impact energy of as-processed SLM samples from Charpy impact tests were either comparable to [304] or better than (~1.5 times) [254] the cast material. The dynamic yield strength of heat-treated samples from planar impact tests was almost double that of the sand-cast counterpart, while the dynamic tensile strength was four times better [305]. The improved impact strength is owing to the finer more homogeneous microstructure.

Despite having a bit of influence on some mechanical properties, anisotropy was not evident in the case of impact resistance, *i.e.* the material's resistance to impact was not dependent on the build orientation [254,305].

8.9. Wear resistance

The tribological behaviour of an SLM Al part is particularly important for applications in the automotive industry where a part can experience a significant amount of friction in application. In the Al-Si alloy family, the higher the Si content, the higher is the material's wear resistance [178]. The finer grain structure produced by SLM results in good wear resistance in the case of sliding wear, surpassing its cast [286] and extruded [183] counterparts. Similar results were observed for wear by erosion [306] and corrosion [307].

Wear resistance can be enhanced by adding reinforcements to the materials. Metallic reinforcements offer better compatibility with the parent metal compared to ceramic reinforcements. For example, the metallic reinforcement TNM granted AlSi12 higher wear resistance capabilities [293].

The wear mechanism is mainly abrasive for higher hardness materials, shifting to adhesive as the hardness decreases [183]; this is influenced by the SLM process parameters. A material's resistance to wear is directly proportional to its hardness. The lowest wear rate is therefore observed for parts in the as-built condition; annealing softens the material leading to a higher wear rate (see Fig. 34(a)).

The tribological behaviour of the SLM material in comparison to the cast counterpart is shown in Fig. 34(b) [286]. Since processing by SLM produces material that is harder than the conventional processes do, the enhanced tribological behaviour is justified.

The coefficient of friction in SLM samples is higher at the surface [109] due to the presence of a surface oxide layer, which is removed during the first rounds of sliding in a wear test. Beyond this layer, the coefficient of friction stabilises and becomes more representative of the material's performance. Kang et al. [183] attributed this to the weld-fracture mechanism common in soft metals before stabilisation. This is observed in the form of fluctuations in the coefficient of friction patterns. The longer the fluctuation region, the softer the material. Samples that suffer from extensive porosity tend to show no fluctuation region due to the limited weld-fraction mechanism.

8.10. Electrical properties

Al is a good conductor for electricity; coupled with its weight and price compared to copper, silver, and gold, it is attractive for a range of electrical applications. Alloying elements, particularly if they have more of an insulating nature, can however increase the electrical resistance [308]. The extent of resistance is correlated to their morphology and distribution. A finer grain size means an increased area of grain boundaries that are barriers to electrical conductivity. The grain boundary state can significantly influence the material's resistivity, *i.e.* lowering the grain boundary energy state by a heat treatment procedure without affecting the grain size in ultrafine-grained materials can reduce the resistivity [309].

The finer microstructure produced by SLM leads to higher resistivity [283] due to the increased grain boundaries and density of dislocations. In AlSi10Mg, the networks of Si encapsulating the α-Al columnar grains act as barriers increasing the resistivity. Therefore, the anisotropic nature of SLM parts affects the electrical properties as they are correlated to the build orientation. Horizontal samples tend to show higher resistivity (needing to cross more Si barriers) than the vertical ones with inclined samples showing intermediate values [283].

Heat treatments (annealing and T6-procedure) reduce the resistivity of the parts to be closer to the cast counterpart [283,308], in addition to eliminating anisotropy [283]. This is attributed to the phase transformation during heat treatment (Section 7), where the breakdown of Si allows an easier path for the electrons along the Al matrix. It is important to note that these heat treatment procedures however were not optimised for the lowest resistivity. Further improvements can potentially be achieved.

Another approach to reduce the material's resistivity is the use of additives during the SLM process. Adding carbon nanotubes (CNT) to AlSi10Mg significantly reduced the resistivity [310]. This was attributed to the presence of C in the material due to the decomposition of the CNT upon laser irradiation. However, further investigations are needed to support this hypothesis, as the

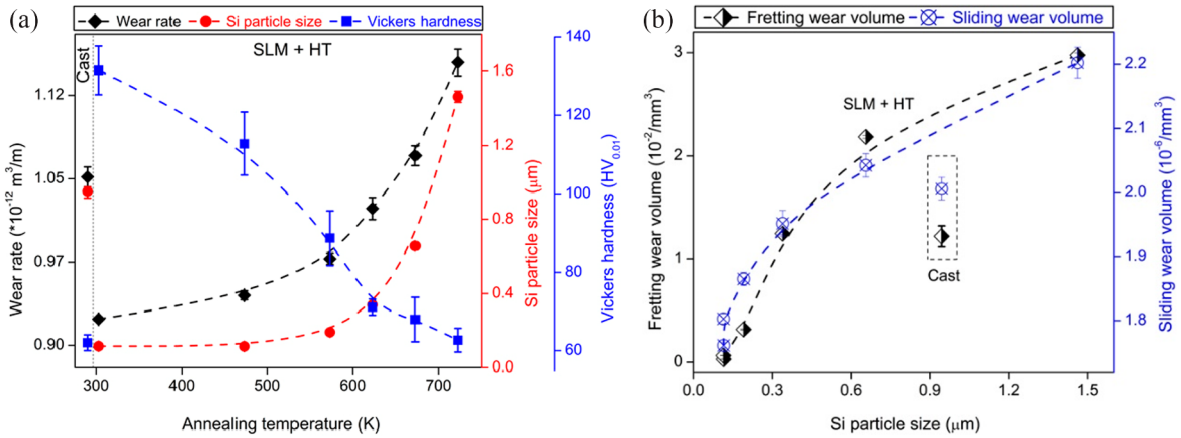

Fig. 34. (a) The effect of heat treatment on the wear rate and hardness in SLM AlSi12. (b) The tribological behaviour of the SLM material shown to be comparable to the cast counterpart [286].

authors of the work used energy dispersive spectroscopy to prove the presence of C, which might not be the most accurate technique. Raman spectroscopy would serve better to analyse the form of C present in the material after SLM.

9. Summary

Additive manufacturing of metals is becoming more common – both on the industrial and academic levels – with the recent advancements in the field. This review article focussed on the recent progress in the literature on selective laser melting of Al-alloys.

Al alloys are in high demand in various industrial sectors, therefore they are receiving significant attention. Being a large alloy family with a range of alloying elements, not all classes of Al-alloys behaved similarly when processed by SLM due to the difference in alloying elements and compositions.

There is an abundance of published works on optimising the process parameters to avoid the formation of defects (pores, cracks, laser spatter, surface irregularities, and shape distortions) in the fabricated parts. Some of these defects can now be resolved in-process while others still require post-processing. Virtually defect-free parts from Al-Si alloys can now be fabricated using a range of SLM systems. These alloys are conventionally processed by casting due to the presence of the Si hard phase, which poses limitations on their machinability. Their excellent fluidity and cast-ability are behind the good SLM process-ability and the larger amount of work conducted on them compared to the other Al alloys. The high strength Al alloys remain challenging as they suffer extensive cracking; these cracks form during the final stages of solidification due to material shrinkage. The most effective approach to eliminate cracks is changing the alloy composition by in-situ alloying where the added elements promote heterogeneous nucleation during solidification, replacing the columnar microstructure (common in SLM materials) with an equiaxed microstructure avoiding cracks' formation.

During processing, the metal powder is irradiated with a high energy laser beam and allowed to rapidly solidify to room temperature. The steep cooling rate leads to the formation of extremely fine microstructures within the overlapping melt pools. Three regions of grains make up every melt pool; the core with fine equiaxed grains, the boundary with coarser columnar grains, and the heat affected zone. The columnar grains grow in the direction of the thermal gradient. This directionality produces a textured material with the texture controllable by the scan strategy used during processing. The characteristically fine microstructure produced during manufacture is an excellent alternative to the traditional approach of using additives to refine the conventionally-processed microstructures to improve their mechanical properties and cope with the demands of the automotive and aerospace industries [273]. This was reflected on the improved hardness, tensile and compressive strengths, fatigue performance, creep, impact, and wear resistance, and electrical properties. The main downside in SLM parts is the lack of ductility. However, heat treatments provide the material with an increase of ductility and with careful treatment selection the strength is not significantly lost.

10. The outlook

The amount of work undertaken in the field of SLM of Al alloys nowadays is significant. However, some confinement is needed to direct the future research into the aspects that can further improve the standing of the technology. This section provides some examples for the areas that can benefit from researchers' efforts in the future. Some of these topics are of a more generic nature that they can be applied to the process irrespective of the material being processed.

Material qualification studies often optimise the process parameters for cubic samples with side dimensions that range from 5 to 10 mm. However, the set of optimised parameters at this scale might not be scalable for larger or smaller parts, *i.e.* the quality of larger parts can be different and they might even become more susceptible to failure during processing. Research into the effect of the sample size on the process parameters and their selection is still lacking. Similarly, the translation of these process parameters to the fabrication of significantly small features, such as in the case of lattice structures, is not yet fully explored. Custom scan-strategies for lattice structures can improve their quality and thus their performance will be enhanced.

Research into remedying the defects produced in SLM parts has been split into two routes; in-process or post-processing. Although the latter route may have received more attention in the literature, research on the former is essential for the progression of SLM as a net-shape manufacturing process as post-processing techniques add to the time and costs of production. For instance, the steep cooling rates in SLM play an important role in the formation of defects in the produced parts and therefore heated build-plates have been used to reduce the residual stresses by slightly slowing down the rate of solidification. Most of the studies deploying this feature used a temperature of 200 °C, limited by the machines' capabilities. Higher build-plate temperatures can potentially reduce the defects developed in the process but its effect on the material's microstructure and mechanical properties and the process's efficiency can be an issue.

Standardizing the properties of metal powders for SLM is important for the process to cope with its needs through producing powder with specifications meeting the process requirements. Despite the success in producing defect-free parts from powders that do not fully comply with the process requirements, it requires extra measures when selecting the process window, which means that every batch of powder might require its own material qualification study if its properties were not identical.

Besides the advances regarding the readily-available alloys, there has been some interest in developing new alloys for the process that take into account the process needs and the target properties concurrently. The reviewed approaches in this field mostly relied on *in-situ* alloying of mixed powders where there is a large chance of segregation in the produced samples due to variations in particle size distributions and such. Designing new alloys for the process and producing them in the form of pre-alloyed powder is costly and beyond the budgets for most research projects. Materials' design softwares and high-throughput methods to experimentally validate the custom alloys are needed to exploit this capability effectively. This should aim at understanding the effect of the alloying constituents on the process-ability of the material by SLM and ultimately the properties of the fabricated parts in application.

The feasibility of SLM and its efficiency is an important area of research [30,33]. However, such research is hindered by the

immaturity of the process reflected in the variability and inconsistency in production. Only when these issues are tackled and the scatter in data from different research that is driven by material variability (depending on the source or supplier that controls the properties of the powders) and the machine variability (variation in results from machine to machine based on manufacturer) [239] is reduced, the efficiency-related research will find its way. Modifications to the currently-available systems and using different types of laser (diode lasers or green lasers) to improve the efficiency of the process can then follow.

References

[1] Astm. ASTM52900-15 Standard Terminology for Additive Manufacturing - General Principles - Terminology. West Conshohocken, PA: ASTM International; 2015.
[2] Grigoriev A, Polozov I, Sufiiarov V, Popovich A. In-situ synthesis of Ti2AlNb-based intermetallic alloy by selective laser melting. J Alloy Compd 2017;704:434–42.
[3] Babu SS, Goodridge R. Additive manufacturing. Mater Sci Technol 2015;31:881–3.
[4] Conner BP, Manogharan GP, Martof AN, Rodomsky LM, Rodomsky CM, Jordan DC, et al. Making sense of 3-D printing: creating a map of additive manufacturing products and services. Addit Manuf 2014;1–4:64–76.
[5] Baumers M, Tuck C, Wildman R, Ashcroft I, Hague R. Shape complexity and process energy consumption in electron beam melting: a case of something for nothing in additive manufacturing? J Ind Ecol 2016. n/a–n/a.
[6] Panesar A, Ashcroft I, Brackett D, Wildman R, Hague R. Design framework for multifunctional additive manufacturing: coupled optimization strategy for structures with embedded functional systems. Addit Manuf 2017;16:98–106.
[7] Maskery I, Hussey A, Panesar A, Aremu A, Tuck C, Ashcroft I, et al. An investigation into reinforced and functionally graded lattice structures. J Cell Plast 2016;53:151–65.
[8] Panesar A, Brackett D, Ashcroft I, Wildman R, Hague R. Hierarchical remeshing strategies with mesh mapping for topology optimisation. Int J Num Meth Eng 2017;111:676–700.
[9] Vaithilingam J, Saleh E, Wildman RD, Hague RJM, Tuck CJ. Optimisation of substrate angles for multi-material and multi-functional inkjet printing. Sci Rep 2018;8:9030.
[10] Kruth JP, Mercelis P, Vaerenbergh JV, Froyen L, Rombouts M. Binding mechanisms in selective laser sintering and selective laser melting. Rapid Prototyp J 2005;11:26–36.
[11] Maskery I, Aremu AO, Simonelli M, Tuck C, Wildman RD, Ashcroft IA, et al. Mechanical properties of Ti-6Al-4V selectively laser melted parts with body-centred-cubic lattices of varying cell size. Exp Mech 2015:1–12.
[12] Maskery I, Aboulkhair NT, Aremu AO, Tuck CJ, Ashcroft IA, Wildman RD, et al. A mechanical property evaluation of graded density Al-Si10-Mg lattice structures manufactured by selective laser melting. Mater Sci Eng A 2016;670:264–74.
[13] Averyanova M, Cicala E, Ph B, Dominique G. Experimental design approach to optimize selective laser melting of martensitic 17–4 PH powder: part I – single laser tracks and first layer. Rapid Prototyp J 2012;18:28–37.
[14] Rännar L-E, Koptyug A, Olsén J, Saeidi K, Shen Z. Hierarchical structures of stainless steel 316L manufactured by Electron Beam Melting. Addit Manuf 2017;17:106–12.
[15] Loeber L, Biamino S, Ackelid U, Sabbadini S, Epicoco P, Fino P, et al. Comparison of seletive laser and electron beam melted Titanium Aluminides. Solid freedom fabrication symposium. 2011.
[16] Gibson I, Rosen DW, Stucker B. Additive manufacturing technologies. Springer; 2010.
[17] Shu X, Chen G, Liu J, Zhang B, Feng J. Microstructure evolution of copper/steel gradient deposition prepared using electron beam freeform fabrication. Mater Lett 2017;213:374–7.
[18] Lathabai Sri. Additive manufacturing of aluminium-based alloys and composites. Fundamentals of aluminium metallurgy Elsevier; 2018. p. 47–92https://linkinghub.elsevier.com/retrieve/pii/B9780081020630000023https://doi.org/10.1016/B978-0-08-102063-0.00002-3.
[19] Shishkovsky I, Missemer F, Smurov I. Metal matrix composites with ternary intermetallic inclusions fabricated by laser direct energy deposition. Compos Struct 2018;183:663–70.
[20] Hamilton RF, Bimber BA, Taheri Andani M, Elahinia M. Multi-scale shape memory effect recovery in NiTi alloys additive manufactured by selective laser melting and laser directed energy deposition. J Mater Process Technol 2017;250:55–64.
[21] Li L, Saedan M, Feng W, Fuh JYH, Wong YS, Loh HT, et al. Development of a multi-nozzle drop-on-demand system for multi-material dispensing. J Mater Process Technol 2009;209:4444–8.
[22] Cao W, Miyamoto Y. Freeform fabrication of aluminum parts by direct deposition of molten aluminum. J Mater Process Technol 2006;173:209–12.
[23] Yamaguchi K, Sakai K, Yamanaka T, Hirayama T. Generation of three-dimensional micro structure using metal jet. Precis Eng 2000;24:2–8.
[24] Luo Z, Wang X, Wang L, Sun D, Li Z. Drop-on-demand electromagnetic printing of metallic droplets. Mater Lett 2017;188:184–7.
[25] Adrian FJ, Bohandy J, Kim BF, Jette AN. A study of the mechanism of metal deposition by the laser-induced forward transfer process. J Vac Sci Technol B: Microelectron Process Phenom 1987;5.
[26] Visser CW, Pohl R, Sun C, Römer G-W, Huis in 't Veld B, Lohse D. Toward 3D printing of pure metals by laser-induced forward transfer. Adv Mater 2015;27:4087–92.
[27] Kempen K, Vrancken B, Thijs L, Buls S, Van Humbeeck J, Kruth J-P. Lowering thermal gradients in Selective Laser melting by pre-heating the baseplate. Solid freedom fabrication symposium. 2013.
[28] Buchbinder D, Meiners W, Pirch N, Wissenbach K, Schrage J. Investigation on reducing distortion by preheating during manufacture of aluminum components using selective laser melting. J Laser Appl 2014;26.
[29] Buchbinder D, Schleifenbaum H, Heidrich S, Meiners W, Bültmann J. High power selective laser melting (HP SLM) of aluminum parts. Phys Proc 2011;12(Part A):271–8.
[30] Schleifenbaum H, Meiners W, Wissenbach K, Hinke C. Individualized production by means of high power Selective Laser Melting. CIRP J Manuf Sci Technol 2010;2:161–9.
[31] Scipioni Bertoli U, Wolfer AJ, Matthews MJ, Delplanque J-PR, Schoenung JM. On the limitations of volumetric energy density as a design parameter for selective laser. Melt Mater Des 2017;113:331–40.
[32] Aboulkhair NT, Everitt NM, Ashcroft I, Tuck C. Reducing porosity in AlSi10Mg parts processed by selective laser melting. Addit Manuf 2014;1–4:77–86.
[33] Matilainen V, Piili H, Salminen A, Syvänen T, Nyrhilä O. Characterization of process efficiency improvement in laser additive manufacturing. Phys Proc 2014;56:317–26.
[34] Li Y, Gu D. Parametric analysis of thermal behavior during selective laser melting additive manufacturing of aluminum alloy powder. Mater Des 2014;63:856–67.
[35] Kamath C, El-dasher B, Gallegos GF, King WE, Sisto A. Density of additively-manufactured, 316L SS parts using laser powder-bed fusion at powers up to 400W. Int J f Addit Manuf Techol 2013;74:65–78.
[36] Aboulkhair NT. Additive manufacture of an aluminium alloy: processing, microstructure, and mechanical properties. UK: University of Nottingham; 2015.
[37] Su X, Yang Y. Research on track overlapping during Selective Laser Melting of powders. J Mater Process Technol 2012;212:2074–9.
[38] Aboulkhair NT, Maskery I, Tuck C, Ashcroft I, Everitt NM. On the formation of AlSi10Mg single tracks and layers in selective laser melting: microstructure and nano-mechanical properties. J Mater Process Technol 2016;230:88–98.
[39] Sufiiarov VS, Popovich AA, Borisov EV, Polozov IA, Masaylo DV, Orlov AV. The Effect of Layer Thickness at Selective Laser Melting. Procedia Eng

2017;174:126–34.
[40] Thijs L, Kempen K, Kruth J-P, Van Humbeeck J. Fine-structured aluminium products with controllable texture by selective laser melting of pre-alloyed AlSi10Mg powder. Acta Mater 2013;61:1809–19.
[41] Pauly S, Wang P, Kühn U, Kosiba K. Experimental determination of cooling rates in selectively laser-melted eutectic Al-33Cu. Addit Manuf 2018;22:753–7.
[42] Thomas M, Baxter GJ, Todd I. Normalised model-based processing diagrams for additive layer manufacture of engineering alloys. Acta Mater 2016;108:26–35.
[43] Trapp J, Rubenchik AM, Guss G, Matthews MJ. In situ absorptivity measurements of metallic powders during laser powder-bed fusion additive manufacturing. Appl Mater Today 2017;9:341–9.
[44] Matthews M, Trapp J, Guss G, Rubenchik A. Direct measurements of laser absorptivity during metal melt pool formation associated with powder bed fusion additive manufacturing processes. J Laser Appl 2018;30:032302.
[45] Prashanth KG, Scudino S, Maity T, Das J, Eckert J. Is the energy density a reliable parameter for materials synthesis by selective laser melting? Mater Res Lett 2017;5:386–90.
[46] Sigmund O, Maute K. Topology optimization approaches A comparative review. Struct Multidiscip O 2013;48:1031–55.
[47] Allaire G, Jouve F, Toader AM. Structural optimization using sensitivity analysis and a level-set method. J Comput Phys 2004;194:363–93.
[48] Wang MY, Wang X, Guo D. A level set method for structural topology optimization. Comput Meth Appl Mech Eng 2003;192:227–46.
[49] Abdi M, Ashcroft I, Wildman R. Topology optimization of geometrically nonlinear structures using an evolutionary optimization method. Eng Optim 2018:1–21.
[50] Abdi M, Wildman R, Ashcroft I. Evolutionary topology optimization using the extended finite element method and isolines. Eng Optim 2013;46:628–47.
[51] Bendsøe Martin P, Sigmund Ole, editors. Topology optimization: theory, methods and applications. Berlin, Heidelberg: Springer Berlin Heidelberg; 2004.
[52] Brackett D, Ashcroft I, Hague R. Topology optimization for additive manufacturing. Solid freedom fabrication symposium, Texas, USA. 2011.
[53] Seabra M, Azevedo J, Araújo A, Reis L, Pinto E, Alves N, et al. Selective laser melting (SLM) and topology optimization for lighter aerospace componentes. Proc Struct Integr 2016;1:289–96.
[54] Yadroitsev I, Thivillon L, Bertrand P, Smurov I. Strategy of manufacturing components with designed internal structure by selective laser melting of metallic powder. Appl Surf Sci 2007;254:980–3.
[55] Materialise 3-matic software.
[56] Autodesk Netfabb software.
[57] Yan C, Hao L, Hussein A, Bubb SL, Young P, Raymont D. Evaluation of light-weight AlSi10Mg periodic cellular lattice structures fabricated via direct metal laser sintering. J Mater Process Technol 2014;214:856–64.
[58] Yan C, Hao L, Hussein A, Young P, Huang J, Zhu W. Microstructure and mechanical properties of aluminium alloy cellular lattice structures manufactured by direct metal laser sintering. Mater Sci Eng, A 2015;628:238–46.
[59] Beyer C, Figueroa D. Design and analysis of lattice structures for additive manufacturing. J Manuf Sci Eng 2016;138:121014–5.
[60] Qiu C, Yue S, Adkins NJE, Ward M, Hassanin H, Lee PD, et al. Influence of processing conditions on strut structure and compressive properties of cellular lattice structures fabricated by selective laser melting. Mater Sci Eng, A 2015;628:188–97.
[61] Maskery I, Aboulkhair NT, Aremu AO, Tuck CJ, Ashcroft IA. Compressive failure modes and energy absorption in additively manufactured double gyroid lattices. Addit Manuf 2017;16:24–9.
[62] Tancogne-Dejean T, Spierings AB, Mohr D. Additively-manufactured metallic micro-lattice materials for high specific energy absorption under static and dynamic loading. Acta Mater 2016;116:14–28.
[63] Mines RAW, Tsopanos S, Shen Y, Hasan R, McKown ST. Drop weight impact behaviour of sandwich panels with metallic micro lattice cores. Int J Impact Eng 2013;60:120–32.
[64] Wong M, Owen I, Sutcliffe CJ, Puri A. Convective heat transfer and pressure losses across novel heat sinks fabricated by Selective Laser Melting. Int J Heat Mass Transf 2009;52:281–8.
[65] Emmelmann C, Scheinemann P, Munsch M, Seyda V. Laser additive manufacturing of modified implant surfaces with osseointegrative characteristics. Phys Proc 2011;12:375–84.
[66] Murr LE, Gaytan SM, Martinez E, Medina F, Wicker RB. Next generation orthopaedic implants by additive manufacturing using electron beam melting. Int J Biomater 2012;2012:14.
[67] Yan C, Hao L, Hussein A, Young P. Ti–6Al–4V triply periodic minimal surface structures for bone implants fabricated via selective laser melting. J Mech Behav Biomed Mater 2015;51:61–73.
[68] Zhang XY, Fang G, Zhou J. Additively manufactured scaffolds for bone tissue engineering and the prediction of their mechanical. Behav Rev Mater (Basel, Switzerland) 2017;10.
[69] Matlack KH, Bauhofer A, Krödel S, Palermo A, Daraio C. Composite 3D-printed metastructures for low-frequency and broadband vibration absorption. Proc Natl Acad Sci 2016;113:8386–90.
[70] Hur K, Hennig RG, Wiesner U. Exploring periodic bicontinuous cubic network structures with complete phononic bandgaps. J Phys Chem C 2017;121:22347–52.
[71] Wang X, Zhang P, Ludwick S, Belski E, To AC. Natural frequency optimization of 3D printed variable-density honeycomb structure via a homogenization-based approach. Addit Manuf 2018;20:189–98.
[72] Abueidda DW, Jasiuk I, Sobh NA. Acoustic band gaps and elastic stiffness of PMMA cellular solids based on triply periodic minimal surfaces. Mater Des 2018;145:20–7.
[73] Gibson LJ, Ashby MF. Cellular solids: structure and properties. 2nd ed. Cambridge: Cambridge University Press; 1999.
[74] Khaderi SN, Deshpande VS, Fleck NA. The stiffness and strength of the gyroid lattice. Int J Solids Struct 2014;51:3866–77.
[75] Kapfer SC, Hyde ST, Mecke K, Arns CH, Schröder-Turk GE. Minimal surface scaffold designs for tissue engineering. Biomaterials 2011;32:6875–82.
[76] Montazerian H, Davoodi E, Asadi-Eydivand M, Kadkhodapour J, Solati-Hashjin M. Porous scaffold internal architecture design based on minimal surfaces: a compromise between permeability and elastic properties. Mater Des 2017;126:98–114.
[77] Al-Ketan O, Abu Al-Rub RK, Rowshan R. The effect of architecture on the mechanical properties of cellular structures based on the IWP minimal surface. J Mater Res 2018;33:343–59.
[78] Al-Ketan O, Rowshan R, Abu Al-Rub RK. Topology-mechanical property relationship of 3D printed strut, skeletal, and sheet based periodic metallic cellular materials. Addit Manuf 2018;19:167–83.
[79] Rosen DW. Research supporting principles for design for additive manufacturing.pdf. Virt Phys Prototyp 2014;9:225–32.
[80] Tang Y, Dong G, Zhou Q, Zhao YF. Lattice structure design and optimization with additive manufacturing constraints. IEEE Trans Autom Sci Eng 2017:1–17.
[81] Tang YL, Zhao YF. A survey of the design methods for additive manufacturing to improve functional performance. Rapid Prototyp J 2016;22:569–90.
[82] Thomas D. The development of design rules for selective laser melting the development of design rules for selective laser melting. Philosophy 2009.
[83] Calignano F. Design optimization of supports for overhanging structures in aluminum and titanium alloys by selective laser melting. Mater Des 2014;64:203–13.
[84] Brika SE, Mezzetta J, Brochu M, Zhao YF. Multi-objective build orientation optimization for powder bed fusion by laser. Volume 2: additive manufacturing. Materials 2017:V002T01A10.
[85] Hussein A, Hao L, Yan CZ, Everson R, Young P. Advanced lattice support structures for metal additive manufacturing. J Mater Process Technol 2013;213:1019–26.
[86] Langelaar M. Topology optimization of 3D self-supporting structures for additive manufacturing. Addit Manuf 2016;12:60–70.
[87] Read N, Wang W, Essa K, Attallah MM. Selective laser melting of AlSi10Mg alloy: process optimisation and mechanical properties development. Mater Des 2015;65:417–24.
[88] Aboulkhair NT, Everitt NM, Maskery I, Ashcroft I, Tuck C. Selective laser melting of aluminum alloys. MRS Bull 2017;42:311–9.
[89] Olakanmi EO, Cochrane RF, Dalgarno KW. A review on selective laser sintering/melting (SLS/SLM) of aluminium alloy powders: processing, microstructure, and properties. Prog Mater Sci 2015;74:401–77.

[90] Catchpole-Smith S, Aboulkhair N, Parry L, Tuck C, Ashcroft IA, Clare A. Fractal scan strategies for selective laser melting of 'unweldable' nickel superalloys. Addit Manuf 2017;15:113–22.
[91] Choi J-P, Shin G-H, Yang S, Yang D-Y, Lee J-S, Brochu M, et al. Densification and microstructural investigation of Inconel 718 parts fabricated by selective laser melting. Powder Technol 2017;310:60–6.
[92] Marchese G, Garmendia Colera X, Calignano F, Lorusso M, Biamino S, Minetola P, et al. Characterization and comparison of Inconel 625 processed by selective laser melting and laser metal deposition. Adv Eng Mater 2017;19. 1600635–n/a.
[93] Carter LN, Martin C, Withers PJ, Attallah MM. The influence of the laser scan strategy on grain structure and cracking behaviour in SLM powder-bed fabricated nickel superalloy. J Alloy Compd 2014;615:338–47.
[94] Garibaldi M, Ashcroft I, Lemke JN, Simonelli M, Hague R. Effect of annealing on the microstructure and magnetic properties of soft magnetic Fe-Si produced via laser additive manufacturing. Scr Mater 2018;142:121–5.
[95] Garibaldi M, Ashcroft I, Simonelli M, Hague R. Metallurgy of high-silicon steel parts produced using Selective Laser Melting. Acta Mater 2016;110:207–16.
[96] Lemke JN, Simonelli M, Garibaldi M, Ashcroft I, Hague R, Vedani M, et al. Calorimetric study and microstructure analysis of the order-disorder phase transformation in silicon steel built by SLM. J Alloy Compd 2017;722:293–301.
[97] Simonelli M. Microstructure evolution and mechanical properties of selective laser melted Ti-6Al-4V [doctoral thesis] Loughborough University; 2014.
[98] Simonelli M, Tse YY, Tuck C. Effect of the build orientation on the mechanical properties and fracture modes of SLM Ti–6Al–4V. Mater Sci Eng, A 2014;616:1–11.
[99] Simonelli M, Tse YY, Tuck C. On the texture formation of selective laser melted Ti-6Al-4V. Metall Mater Trans A 2014;45:2863–72.
[100] Ciurana J, Hernandez L, Delgado J. Energy density analysis on single tracks formed by selective laser melting with CoCrMo powder material. Int J Addit Manuf Techol 2013;68:1103–10.
[101] Pupo Y, Delgado J, Serenó L, Ciurana J. Scanning space analysis in selective laser melting for CoCrMo powder. Proc Eng 2013;63:370–8.
[102] Monroy K, Delgado J, Ciurana J. Study of the pore formation on CoCrMo alloys by selective laser melting manufacturing process. Proc Eng 2013;63:361–9.
[103] Takaichi A, Suyalatu, Nakamoto T, Joko N, Nomura N, Tsutsumi Y, et al. Microstructures and mechanical properties of Co–29Cr–6Mo alloy fabricated by selective laser melting process for dental applications. J Mech Behav Biomed Mater 2013;21:67–76.
[104] Yadroitsev I, Gusarov A, Yadroitsava I, Smurov I. Single track formation in selective laser melting of metal powders. J Mater Process Technol 2010;210:1624–31.
[105] Zhang B, Liao H, Coddet C. Effects of processing parameters on properties of selective laser melting Mg–9%Al powder mixture. Mater Des 2012;34:753–8.
[106] Song B, Dong S, Deng S, Liao H, Coddet C. Microstructure and tensile properties of iron parts fabricated by selective laser melting. Opt Laser Technol 2014;56:451–60.
[107] Ng CC, Savalani MM, Lau ML, Man HC. Microstructure and mechanical properties of selective laser melted magnesium. Appl Surf Sci 2011;257:7447–54.
[108] Wang D, Yu C, Ma J, Liu W, Shen Z. Densification and crack suppression in selective laser melting of pure molybdenum. Mater Des 2017;129:44–52.
[109] Gu D, Hagedorn Y-C, Meiners W, Meng G, Batista RJS, Wissenbach K, et al. Densification behavior, microstructure evolution, and wear performance of selective laser melting processed commercially pure titanium. Acta Mater 2012;60:3849–60.
[110] Demir AG, Monguzzi L, Previtali B. Selective laser melting of pure Zn with high density for biodegradable implant manufacturing. Addit Manuf 2017;15:20–8.
[111] Martin JH, Yahata BD, Hundley JM, Mayer JA, Schaedler TA, Pollock TM. 3D printing of high-strength aluminium alloys. Nature 2017;549:365.
[112] Andersson JO, Helander T, Höglund L, Shi P, Sundman B. Thermo-Calc & DICTRA, computational tools for materials science. Calphad 2002;26(2):273–312.
[113] Pollock TM. Alloy design for aircraft engines. Nat Mater 2016;15:809.
[114] Jain A, Ong SP, Hautier G, Chen W, Richards WD, Dacek S, et al. Commentary: The Materials Project: a materials genome approach to accelerating materials innovation. APL Mater 2013;1:011002.
[115] Ahuja B, Karg M, Nagulin KY, Schmidt M. Fabrication and characterization of high strength Al-Cu alloys processed using laser beam melting in metal powder bed. Phys Proc 2014;56:135–46.
[116] Porter DA, Easterling KE. Phase transformation in metals and alloys. Great Britain: Chapman & Hall; 1992.
[117] Brown MS, Arnold CB. Fundametals of Laser-Material interaction and application to multiscale surface modification. In: Sugioka K, editor. Laser precision microfabrication. Germany: Springer; 2010. p. 91–120.
[118] Ion JC. Laser processing of engineering materials: principles, procedure and industrial application. United Kingdom: Elsevier; 2005.
[119] Prashanth KG, Eckert J. Formation of metastable cellular microstructures in selective laser melted alloys. J Alloy Compd 2017;707:27–34.
[120] Wu J, Wang XQ, Wang W, Attallah MM, Loretto MH. Microstructure and strength of selectively laser melted AlSi10Mg. Acta Mater 2016;117:311–20.
[121] Peter M, Jean-Pierre K. Residual stresses in selective laser sintering and selective laser melting. Rapid Prototyp J 2006;12:254–65.
[122] Montero Sistiaga ML, Mertens R, Vrancken B, Wang X, Van Hooreweder B, Kruth J-P, et al. Changing the alloy composition of Al7075 for better processability by selective laser melting. J Mater Process Technol 2016;238:437–45.
[123] Aboulkhair NT, Maskery I, Tuck C, Ashcroft I, Everitt NM. Improving the fatigue behaviour of a selectively laser melted aluminium alloy: influence of heat treatment and surface quality. Mater Des 2016;104:174–82.
[124] Aboulkhair NT, Maskery I, Tuck C, Ashcroft I, Everitt NM. The microstructure and mechanical properties of selectively laser melted AlSi10Mg: the effect of a conventional T6-like heat treatment. Mater Sci Eng, A 2016;667:139–46.
[125] Kaufmann N, Imran M, Wischeropp TM, Emmelmann C, Siddique S, Walther F. Influence of process parameters on the quality of aluminium alloy EN AW 7075 using selective laser melting (SLM). Phys Proc 2016;83:918–26.
[126] Plomear IJ. Light alloys: metallurgy of the light metals. 3rd ed. London: Arnold; 1995. ISBN: 0340632070.
[127] The Aluminum Association, Aluminum 101. available at: http://www.aluminum.org/resources/industry-standards/aluminum-alloys-101 [accessed 01/05/2018].
[128] Granta Design. CES Edupack Software - Material Level 2 & 3, Granta Design; 2009.
[129] DebRoy T, Wei HL, Zuback JS, Mukherjee T, Elmer JW, Milewski JO, et al. Additive manufacturing of metallic components – process, structure and properties. Prog Mater Sci 2018;92:112–224.
[130] Takata N, Kodaira H, Sekizawa K, Suzuki A, Kobashi M. Change in microstructure of selectively laser melted AlSi10Mg alloy with heat treatments. Mater Sci Eng, A 2017;704:218–28.
[131] Lassance D, Fabrègue D, Delannay F, Pardoen T. Micromechanics of room and high temperature fracture in 6xxx Al alloys. Prog Mater Sci 2007;52:62–129.
[132] Asgari H, Baxter C, Hosseinkhani K, Mohammadi M. On microstructure and mechanical properties of additively manufactured AlSi10Mg_200C using recycled powder. Mater Sci Eng, A 2017;707:148–58.
[133] Zavala-Arredondo M, Boone N, Willmott J, Childs DTD, Ivanov P, Groom KM, et al. Laser diode area melting for high speed additive manufacturing of metallic components. Mater Des 2017;117:305–15.
[134] Zhang J, Song B, Wei Q, Bourell D, Shi Y. A review of selective laser melting of aluminum alloys: processing, microstructure, property and developing trends. J Mater Sci Technol 2019;35:270–84.
[135] Qi T, Zhu H, Zhang H, Yin J, Ke L, Zeng X. Selective laser melting of Al7050 powder: melting mode transition and comparison of the characteristics between the keyhole and conduction mode. Mater Des 2017;135:257–66.
[136] Airbus-Group. SCALMALLOY®RP Auminum-Magnesium-Scandium alloy powder.
[137] Griffiths S, Rossell MD, Croteau J, Vo NQ, Dunand DC, Leinenbach C. Effect of laser rescanning on the grain microstructure of a selective laser melted Al-Mg-Zr alloy. Mater Charact 2018;143:34–42.
[138] Schmidtke K, Palm F, Hawkins A, Emmelmann C. Process and mechanical properties: applicability of a scandium modified Al-alloy for laser additive manufacturing. Phys Proc 2011;12:369–74.
[139] Spierings AB, Dawson K, Voegtlin M, Palm F, Uggowitzer PJ. Microstructure and mechanical properties of as-processed scandium-modified aluminium using selective laser melting. CIRP Ann 2016;65:213–6.

[140] Gharbi O, Jiang D, Feenstra DR, Kairy SK, Wu Y, Hutchinson CR, et al. On the corrosion of additively manufactured aluminium alloy AA2024 prepared by selective laser melting. Corros Sci 2018;143:93–106.
[141] Karg M, Ahuja B, Wiesenmayer S, Kuryntsev S, Schmidt M. Effects of process conditions on the mechanical behavior of aluminium wrought alloy EN AW-2219 (AlCu6Mn) additively manufactured by laser beam melting in powder bed. Micromachines 2017;8:23.
[142] Casati R, Lemke JN, Alarcon AZ, Vedani M. Aging behavior of high-strength Al alloy 2618 produced by selective laser melting. Metall Mater Trans A 2017;48:575–9.
[143] Pantělejev LDK, Paloušek D, Kaiser J. Mechanical and microstructural properties of 2618 Al-alloy processed by SLM remelting strategy. Mater Sci Forum 2017;891:343–9.
[144] Siddique S, Wycisk E, Frieling G, Emmelmann C, Walther F. Microstructural and mechanical properties of selective laser melted Al 4047. Appl Mech Mater 2015;752–753:485–90.
[145] Louvis E, Fox P, Sutcliffe CJ. Selective laser melting of aluminium components. J Mater Process Technol 2011;211:275–84.
[146] Dadbakhsh S, Mertens R, Vanmeensel K, Vleugels J, Humbeeck JV, Kruth J-P. In situ alloying and reinforcing of Al6061 during selective laser melting. Proc CIRP 2018;74:39–43.
[147] Li Y, Zhou K, Tor SB, Chua CK, Leong KF. Heat transfer and phase transition in the selective laser melting process. Int J Heat Mass Transf 2017;108:2408–16.
[148] Carluccio D, Bermingham MJ, Zhang Y, StJohn DH, Yang K, Rometsch PA, et al. Grain refinement of laser remelted Al-7Si and 6061 aluminium alloys with Tibor® and scandium additions. J Manuf Processes 2018;35:715–20.
[149] Sun S, Liu P, Hu J, Hong C, Qiao X, Liu S, et al. Effect of solid solution plus double aging on microstructural characterization of 7075 Al alloys fabricated by selective laser melting (SLM). Opt Laser Technol 2019;114:158–63.
[150] Reschetnik W, Brüggemann JP, Aydinöz ME, Grydin O, Hoyer KP, Kullmer G, et al. Fatigue crack growth behavior and mechanical properties of additively processed EN AW-7075 aluminium alloy. Proc Struct Integr 2016;2:3040–8.
[151] Rao H, Giet S, Yang K, Wu XH, Davies CHJ. The influence of processing parameters on aluminium alloy A357 manufactured by Selective Laser Melting. Mater Des 2016;109:334–46.
[152] Yang KV, Rometsch P, Jarvis T, Rao J, Cao S, Davies C, et al. Porosity formation mechanisms and fatigue response in Al-Si-Mg alloys made by selective laser melting. Mater Sci Eng, A 2018;712:166–74.
[153] Wang M, Song B, Wei Q, Zhang Y, Shi Y. Effects of annealing on the microstructure and mechanical properties of selective laser melted AlSi7Mg alloy. Mater Sci Eng, A 2019;739:463–72.
[154] Rao JH, Zhang Y, Zhang K, Huang A, Davies CHJ, Wu X. Multiple precipitation pathways in an Al-7Si-0.6Mg alloy fabricated by selective laser melting. Scr Mater 2019;160:66–9.
[155] Kempen K, Thijs L, Van Humbeeck J, Kruth JP. Processing AlSi10Mg by selective laser melting: parameter optimisation and material characterisation. Mater Sci Technol 2014;31:917–23.
[156] Maskery I, Aboulkhair NT, Corfield MR, Tuck C, Clare AT, Leach RK, et al. Quantification and characterisation of porosity in selectively laser melted Al–Si10–Mg using X-ray computed tomography. Mater Charact 2016;111:193–204.
[157] Simonelli M, Tuck C, Aboulkhair NT, Maskery I, Ashcroft I, Wildman RD, et al. A Study on the laser spatter and the oxidation reactions during selective laser melting of 316L stainless steel, Al-Si10-Mg, and Ti-6Al-4V. Metall Mater Trans A 2015;46A:3842–51.
[158] Taheri Andani M, Dehghani R, Karamooz-Ravari MR, Mirzaeifar R, Ni J. Spatter formation in selective laser melting process using multi-laser technology. Mater Des 2017;131:460–9.
[159] Weingarten C, Buchbinder D, Pirch N, Meiners W, Wissenbach K, Poprawe R. Formation and reduction of hydrogen porosity during selective laser melting of AlSi10Mg. J Mater Process Technol 2015;221:112–20.
[160] Boschetto A, Bottini L, Veniali F. Roughness modeling of AlSi10Mg parts fabricated by selective laser melting. J Mater Process Technol 2017;241:154–63.
[161] Yang T, Liu T, Liao W, MacDonald E, Wei H, Chen X, et al. The influence of process parameters on vertical surface roughness of the AlSi10Mg parts fabricated by selective laser melting. J Mater Process Technol 2019;266:26–36.
[162] Aboulkhair NT, Tuck C, Ashcroft I, Maskery I, Everitt NM. On the Precipitation Hardening of Selective Laser Melted AlSi10Mg. Metall Mater Trans A 2015;46A:3337–41.
[163] Rosenthal I, Stern A, Frage N. Microstructure and mechanical properties of AlSi10Mg parts produced by the laser beam additive manufacturing (AM) technology. Metall Microstruct Anal 2014;3:448–53.
[164] Tang M, Pistorius PC, Narra S, Beuth JL. Rapid solidification: selective laser melting of AlSi10Mg. JOM-US 2016;68:960–6.
[165] Li W, Li S, Liu J, Zhang A, Zhou Y, Wei Q, et al. Effect of heat treatment on AlSi10Mg alloy fabricated by selective laser melting: microstructure evolution, mechanical properties and fracture mechanism. Mater Sci Eng, A 2016;663:116–25.
[166] Tradowsky U, White J, Ward RM, Read N, Reimers W, Attallah MM. Selective laser melting of AlSi10Mg: influence of post-processing on the microstructural and tensile properties development. Mater Des 2016;105:212–22.
[167] Zhuo L, Wang Z, Zhang H, Yin E, Wang Y, Xu T, et al. Effect of post-process heat treatment on microstructure and properties of selective laser melted AlSi10Mg alloy. Mater Lett 2019;234:196–200.
[168] Takata N, Kodaira H, Suzuki A, Kobashi M. Size dependence of microstructure of AlSi10Mg alloy fabricated by selective laser melting. Mater Charact 2018;143:18–26.
[169] Zhao X, Gu D, Ma C, Xi L, Zhang H. Microstructure characteristics and its formation mechanism of selective laser melting SiC reinforced Al-based composites. Vacuum 2019;160:189–96.
[170] Tang M, Pistorius PC. Oxides, porosity and fatigue performance of AlSi10Mg parts produced by selective laser melting. Int J Fatigue 2017;94:192–201.
[171] Everitt Nicola M, Aboulkhair Nesma T, Maskery Ian, Tuck Chris, Ashcroft I. Nanoindentation shows uniform local mechanical properties across melt pools and layers produced by selective laser melting of AlSi 10Mg alloy. Adv Mater Lett 2016;7:13–6.
[172] Brandl E, Heckenberger U, Holzinger V, Buchbinder D. Additive manufactured AlSi10Mg samples using Selective Laser Melting (SLM): microstructure, high cycle fatigue, and fracture behavior. Mater Des 2012;34:159–69.
[173] Rakesh ChS, Priyanka N, Jayaganthan R, Vasa NJ. Effect of build atmosphere on the mechanical properties of AlSi10Mg produced by selective laser melting. Mater Today: Proc 2018;5:17231–8.
[174] Uzan NE, Shneck R, Yeheskel O, Frage N. High-temperature mechanical properties of AlSi10Mg specimens fabricated by additive manufacturing using selective laser melting technologies (AM-SLM). Addit Manuf 2018;24:257–63.
[175] Olakanmi EO, Cochrane RF, Dalgarno KW. Densification mechanism and microstructural evolution in selective laser sintering of Al–12Si powders. J Mater Process Technol 2011;211:113–21.
[176] Wang XJ, Zhang LC, Fang MH, Sercombe TB. The effect of atmosphere on the structure and properties of a selective laser melted Al–12Si alloy. Mater Sci Eng, A 2014;597:370–5.
[177] Li XP, O'Donnell KM, Sercombe TB. Selective laser melting of Al-12Si alloy: enhanced densification via powder drying. Addit Manuf 2016;10:10–4.
[178] Kang N, Coddet P, Chen C, Wang Y, Liao H, Coddet C. Microstructure and wear behavior of in-situ hypereutectic Al–high Si alloys produced by selective laser melting. Mater Des 2016;99:120–6.
[179] Prashanth KG, Scudino S, Klauss HJ, Surreddi KB, Löber L, Wang Z, et al. Microstructure and mechanical properties of Al–12Si produced by selective laser melting: effect of heat treatment. Mater Sci Eng, A 2014;590:153–60.
[180] Xi L, Wang P, Prashanth KG, Li H, Prykhodko HV, Scudino S, et al. Effect of TiB2 particles on microstructure and crystallographic texture of Al-12Si fabricated by selective laser melting. J Alloy Compd 2019;786:551–6.
[181] Suryawanshi J, Prashanth KG, Scudino S, Eckert J, Prakash O, Ramamurty U. Simultaneous enhancements of strength and toughness in an Al-12Si alloy synthesized using selective laser melting. Acta Mater 2016;115:285–94.
[182] Siddique S, Imran M, Walther F. Very high cycle fatigue and fatigue crack propagation behavior of selective laser melted AlSi12 alloy. Int J Fatigue

2017;94:246–54.
[183] Kang N, Coddet P, Liao H, Baur T, Coddet C. Wear behavior and microstructure of hypereutectic Al-Si alloys prepared by selective laser melting. Appl Surf Sci 2016;378:142–9.
[184] Siddique S, Imran M, Rauer M, Kaloudis M, Wycisk E, Emmelmann C, et al. Computed tomography for characterization of fatigue performance of selective laser melted parts. Mater Des 2015;83:661–9.
[185] Siddique S, Imran M, Wycisk E, Emmelmann C, Walther F. Influence of process-induced microstructure and imperfections on mechanical properties of AlSi12 processed by selective laser melting. J Mater Process Technol 2015;221:205–13.
[186] Prashanth KG, Scudino S, Chatterjee RP, Salman OO, Eckert J. Additive manufacturing: reproducibility of metallic parts. Technologies 2017;5.
[187] Ma P, Prashanth KG, Scudino S, Jia YD, Wang HW, Zou CM, et al. Influence of annealing on mechanical properties of Al-20Si processed by selective laser melting. Metals 2014;4:28–36.
[188] Kang N, Coddet P, Ammar M-R, Liao H, Coddet C. Characterization of the microstructure of a selective laser melting processed Al-50Si alloy: effect of heat treatments. Mater Charact 2017;130:243–9.
[189] Ma P, Jia Y, Prashanth KG, Scudino S, Yu Z, Eckert J. Microstructure and phase formation in Al–20Si–5Fe–3Cu–1Mg synthesized by selective laser melting. J Alloy Compd 2016;657:430–5.
[190] Wang P, Li HC, Prashanth KG, Eckert J, Scudino S. Selective laser melting of Al-Zn-Mg-Cu: heat treatment, microstructure and mechanical properties. J Alloy Compd 2017;707:287–90.
[191] Zhang H, Zhu H, Qi T, Hu Z, Zeng X. Selective laser melting of high strength Al–Cu–Mg alloys: processing, microstructure and mechanical properties. Mater Sci Eng, A 2016;656:47–54.
[192] Prashanth KG, Shakur Shahabi H, Attar H, Srivastava VC, Ellendt N, Uhlenwinkel V, et al. Production of high strength Al85Nd8Ni5Co2 alloy by selective laser melting. Addit Manuf 2015;6:1–5.
[193] Li R, Wang M, Yuan T, Song B, Chen C, Zhou K, et al. Selective laser melting of a novel Sc and Zr modified Al-6.2Mg alloy: processing, microstructure, and properties. Powder Technol 2017;319:117–28.
[194] Shi Y, Yang K, Kairy SK, Palm F, Wu X, Rometsch PA. Effect of platform temperature on the porosity, microstructure and mechanical properties of an Al–Mg–Sc–Zr alloy fabricated by selective laser melting. Mater Sci Eng, A 2018;732:41–52.
[195] Zhang H, Gu D, Yang J, Dai D, Zhao T, Hong C, et al. Selective laser melting of rare earth element Sc modified aluminum alloy: thermodynamics of precipitation behavior and its influence on mechanical properties. Addit Manuf 2018;23:1–12.
[196] Nie X, Zhang H, Zhu H, Hu Z, Qi Y, Zeng X. On the role of Zr content into Portevin-Le Chatelier (PLC) effect of selective laser melted high strength Al-Cu-Mg-Mn alloy. Mater Lett 2019;248:5–7.
[197] Croteau JR, Griffiths S, Rossell MD, Leinenbach C, Kenel C, Jansen V, et al. Microstructure and mechanical properties of Al-Mg-Zr alloys processed by selective laser melting. Acta Mater 2018;153:35–44.
[198] Jia Q, Rometsch P, Cao S, Zhang K, Wu X. Towards a high strength aluminium alloy development methodology for selective laser melting. Mater Des 2019:107775.
[199] Zhou L, Pan H, Hyer H, Park S, Bai Y, McWilliams B, et al. Microstructure and tensile property of a novel AlZnMgScZr alloy additively manufactured by gas atomization and laser powder bed fusion. Scr Mater 2019;158:24–8.
[200] Yadroitsev I, Bertrand P, Smurov I. Parametric analysis of the selective laser melting process. Appl Surf Sci 2007;253:8064–9.
[201] Yang S, Evans JRG. Metering and dispensing of powder; the quest for new solid freeforming techniques. Powder Technol 2007;178:56–72.
[202] Li R, Shi Y, Wang Z, Wang L, Liu J, Jiang W. Densification behavior of gas and water atomized 316L stainless steel powder during selective laser melting. Appl Surf Sci 2010;256:4350–6.
[203] Kempen K, Thijs L, Yasa E, Badrossamay M, Verheecke W, Kruth J-P. Process optimization and microstructural analysis for selective laser melting of AlSi10Mg. Solid freeform fabrication symposium, Texas, Austin, USA. 2011. p. 484–95.
[204] Dai D, Gu D. Thermal behavior and densification mechanism during selective laser melting of copper matrix composites: simulation and experiments. Mater Des 2014;55:482–91.
[205] Yadroitsev I, Krakhmalev P, Yadroitsava I, Johansson S, Smurov I. Energy input effect on morphology and microstructure of selective laser melting single track from metallic powder. J Mater Process Technol 2013;213:606–13.
[206] Cooke A, Slotwinski J. Properties of metal powders for additive manufacturing: a review of the state of the art of metal powder property testing. Materials standards for additive manufacturing; 2012.
[207] Aboulkhair NT, Maskery I, Ashcroft I, Tuck C, Everitt NM. The role of powder properties on the processability of Aluminium alloys in selective laser melting. Lasers in manufacturing, Munich, Germany. 2015.
[208] Sachs M, Hentschel O, Schmidt J, Karg M, Schmidt M, Wirth K-E. Production of Al/Cu-particles and their potential for processing by laser beam melting (LBM). Phys Proc 2014;56:125–34.
[209] Liao H, Zhu H, Xue G, Zeng X. Alumina loss mechanism of Al2O3-AlSi10 Mg composites during selective laser melting. J Alloy Compd 2019;785:286–95.
[210] Bartkowiak K, Ullrich S, Frick T, Schmidt M. New developments of laser processing aluminium alloys via additive manufacturing technique. Phys Proc 2011;12(Part A):393–401.
[211] Wang P, Deng L, Prashanth KG, Pauly S, Eckert J, Scudino S. Microstructure and mechanical properties of Al-Cu alloys fabricated by selective laser melting of powder mixtures. J Alloy Compd 2018;735:2263–6.
[212] Dadbakhsh S, Hao L. Effect of layer thickness in selective laser melting on microstructure of Al/5 wt.%Fe2O3 powder consolidated parts. Sci World J 2014;2014:106129.
[213] Dadbakhsh S, Hao L, Jerrard PGE, Zhang DZ. Experimental investigation on selective laser melting behaviour and processing windows of in situ reacted Al/Fe2O3 powder mixture. Powder Technol 2012;231:112–21.
[214] Chang F, Gu D, Dai D, Yuan P. Selective laser melting of in-situ Al4SiC4 + SiC hybrid reinforced Al matrix composites: influence of starting SiC particle size. Surf Coat Technol 2015;272:15–24.
[215] Gu D, Chang F, Dai D. Selective laser melting additive manufacturing of novel aluminum based composites with multiple reinforcements. J Manuf Sci Eng 2014;137:021010-1–021010-11.
[216] Gu D, Wang H, Chang F, Dai D, Yuan P, Hagedorn Y-C, et al. Selective laser melting additive manufacturing of TiC/AlSi10Mg bulk-form nanocomposites with tailored microstructures and properties. Phys Proc 2014;56:108–16.
[217] Dadbakhsh S, Hao L. In situ formation of particle reinforced al matrix composite by selective laser melting of Al/Fe2O3 powder mixture. Adv Eng Mater 2012;14:45–8.
[218] Gu DD, Wang HQ, Dai DH, Yuan PP, Meiners W, Poprawe R. Rapid fabrication of Al-based bulk-form nanocomposites with novel reinforcement and enhanced performance by selective laser melting. Scr Mater 2015;96:25–8.
[219] Gu D, Wang Z, Shen Y, Li Q, Li Y. In-situ TiC particle reinforced Ti–Al matrix composites: powder preparation by mechanical alloying and Selective Laser Melting behavior. Appl Surf Sci 2009;255:9230–40.
[220] Ma Y, Ji G, Li XP, Chen CY, Tan ZQ, Addad A, et al. On the study of tailorable interface structure in a diamond/Al12Si composite processed by selective laser melting. Materialia 2019;5:100242.
[221] Wang L-z, Chen T, Wang S. Microstructural characteristics and mechanical properties of carbon nanotube reinforced AlSi10Mg composites fabricated by selective laser melting. Optik - Int J Light Electron Opt 2017;143:173–9.
[222] Vora P, Mumtaz K, Todd I, Hopkinson N. AlSi12 in-situ alloy formation and residual stress reduction using anchorless selective laser melting. Addit Manuf 2015;7:12–9.
[223] Ardila LC, Garciandia F, González-Díaz JB, Álvarez P, Echeverria A, Petite MM, et al. Effect of IN718 recycled powder reuse on properties of parts manufactured by means of selective laser melting. Phys Proc 2014;56:99–107.

[224] Maamoun AH, Elbestawi M, Dosbaeva GK, Veldhuis SC. Thermal post-processing of AlSi10Mg parts produced by Selective Laser Melting using recycled powder. Addit Manuf 2018;21:234–47.
[225] Jacob G, Brown C, Donmez A, Watson S, Slotwinski J. Effects of powder recycling on stainless steel powder and built material properties in metal powder bed fusion processes. NIST advanced manufacturing series; 2017.
[226] Sartin B, Pond T, Griffith B, Everhart W, Elder L, Wenski E, et al. 316L powder reuse for metal additive manufacturing. Solid freeform fabrication symposium – an additive manufacturing conference, Austin, TX, USA. 2017. p. 351–64.
[227] Grainger L. White paper: investigating the effects of multiple powder re-use in AM. Renishaw; 2016.
[228] O'Leary R, Setchi R, Prickett P, Hankins G, Jones N. An investigation into the recycling of Ti-6Al-4V powder used within SLM to improve sustainability. Sustain Des Manuf 2015:377–88.
[229] O'Neill CF. Method and apparatus for reconditioning oxidized powder. United States of America: United Technologies corporation; 2014.
[230] Totten GE, Mackenzie DS. Handbook of aluminum: physical metallurgy and processes. 1st ed. New York: CRC Press; 2003.
[231] Handbook of aluminum: volume 2: alloy production and materials manufacturing; 2003.
[232] Zhang B, Dembinski L, Coddet C. The study of the laser parameters and environment variables effect on mechanical properties of high compact parts elaborated by selective laser melting 316L powder. Mater Sci Eng, A 2013;584:21–31.
[233] Matthews MJ, Guss G, Khairallah SA, Rubenchik AM, Depond PJ, King WE. Denudation of metal powder layers in laser powder bed fusion processes. Acta Mater 2016;114:33–42.
[234] Ferrar B, Mullen L, Jones E, Stamp R, Sutcliffe CJ. Gas flow effects on selective laser melting (SLM) manufacturing performance. J Mater Process Technol 2012;212:355–64.
[235] Laakso P, Riipinen T, Laukkanen A, Andersson T, Jokinen A, Revuelta A, et al. Optimization and simulation of SLM process for high density H13 tool steel parts. Phys Proc 2016;83:26–35.
[236] Loh L-E, Chua C-K, Yeong W-Y, Song J, Mapar M, Sing S-L, et al. Numerical investigation and an effective modelling on the Selective Laser Melting (SLM) process with aluminium alloy 6061. Int J Heat Mass Transf 2015;80:288–300.
[237] Wei K, Wang Z, Zeng X. Preliminary investigation on selective laser melting of Ti-5Al-2.5Sn α-Ti alloy: from single tracks to bulk 3D components. J Mater Process Technol 2017;244:73–85.
[238] Yadroitsev I, Smurov I. Surface morphology in selective laser melting of metal powders. Phys Proc 2011;12(Part A):264–70.
[239] Frazier WE. Metal additive manufacturing: a review. J Mater Eng Perform 2014;23:12.
[240] Olakanmi EO. Selective laser sintering/melting (SLS/SLM) of pure Al, Al–Mg, and Al–Si powders: effect of processing conditions and powder properties. J Mater Process Technol 2013;213:1387–405.
[241] Leary M, Mazur M, Elambasseril J, McMillan M, Chirent T, Sun Y, et al. Selective laser melting (SLM) of AlSi12Mg lattice structures. Mater Des 2016;98:344–57.
[242] Kimura T, Nakamoto T. Microstructures and mechanical properties of A356 (AlSi7Mg0.3) aluminum alloy fabricated by selective laser melting. Mater Des 2016;89:1294–301.
[243] Haboudou A, Peyre P, Vannes AB, Peix G. Reduction of porosity content generated during Nd:YAG laser welding of A356 and AA5083 aluminium alloys. Mater Sci Eng, A 2003;363:40–52.
[244] King WE, Barth HD, Castillo VM, Gallegos GF, Gibbs JW, Hahn DE, et al. Observation of keyhole-mode laser melting in laser powder-bed fusion additive manufacturing. J Mater Process Technol 2014;214:2915–25.
[245] Awd M, Tenkamp J, Hirtler M, Siddique S, Bambach M, Walther F. Comparison of microstructure and mechanical properties of Scalmalloy((R)) produced by selective laser melting and laser metal deposition. Materials (Basel, Switzerland) 2017;11.
[246] Parry L, Ashcroft IA, Wildman RD. Understanding the effect of laser scan strategy on residual stress in selective laser melting through thermo-mechanical simulation. Addit Manuf 2016;12:1–15.
[247] Bidare P, Bitharas I, Ward RM, Attallah MM, Moore AJ. Fluid and particle dynamics in laser powder bed fusion. Acta Mater 2018;142:107–20.
[248] Ly S, Rubenchik AM, Khairallah SA, Guss G, Matthews MJ. Metal vapor micro-jet controls material redistribution in laser powder bed fusion additive manufacturing. Sci Rep 2017;7:4085.
[249] Mower TM, Long MJ. Mechanical behavior of additive manufactured, powder-bed laser-fused materials. Mater Sci Eng, A 2016;651:198–213.
[250] Wang L-z, Wang S, Wu J-J. Experimental investigation on densification behavior and surface roughness of AlSi10Mg powders produced by selective laser melting. Opt Laser Technol 2017;96:88–96.
[251] Park H-S, Nguyen D-S. Study on flaking behavior in selective laser melting process. Proc CIRP 2017;63:569–72.
[252] Tuck C, Maskery I, Simonelli M, Aboulkhair N, Ashcroft I, Everitt N, et al. Aspects of the process and material relationships in the selective laser melting of aluminium alloys. TMS Annual meeting and exhibition. 2015.
[253] Tammas-Williams S, Zhao H, Léonard F, Derguti F, Todd I, Prangnell PB. XCT analysis of the influence of melt strategies on defect population in Ti–6Al–4V components manufactured by Selective Electron Beam Melting. Mater Charact 2015;102:47–61.
[254] Kempen K, Thijs L, Van Humbeeck J, Kruth JP. Mechanical properties of AlSi10Mg produced by selective laser melting. Phys Proc 2012;39:439–46.
[255] Smith RJ, Hirsch M, Patel R, Li W, Clare AT, Sharples SD. Spatially resolved acoustic spectroscopy for selective laser melting. J Mater Process Technol 2016;236:93–102.
[256] Hirsch M, Catchpole-Smith S, Patel R, Marrow P, Li W, Tuck C, et al. Meso-scale defect evaluation of selective laser melting using spatially resolved acoustic spectroscopy. Proc Math Phys Eng Sci 2017;473:20170194.
[257] Spierings AB, Schneider M, Eggenberger R. Comparison of density measurement techniques for additive manufactured metallic parts. Rapid Prototyp J 2011;17:380–6.
[258] Palacio-Mancheno PE, Larriera AI, Doty SB, Cardoso L, Fritton SP. 3D assessment of cortical bone porosity and tissue mineral density using high-resolution microCT: effects of resolution and threshold method. J Bone Min Res Off J Am Soc Bone Min Res 2014;29:142–50.
[259] Saxena N, Hofmann R, Alpak FO, Dietderich J, Hunter S, Day-Stirrat RJ. Effect of image segmentation & voxel size on micro-CT computed effective transport & elastic properties. Mar Pet Geol 2017;86:972–90.
[260] Wong HS, Head MK, Buenfeld NR. Pore segmentation of cement-based materials from backscattered electron images. Cem Concr Res 2006;36:1083–90.
[261] Iassonov P, Gebrenegus T, Tuller M. Segmentation of X-ray computed tomography images of porous materials: a crucial step for characterization and quantitative analysis of pore structures. Water Resour Res 2009;45.
[262] Kasperovich G, Haubrich J, Gussone J, Requena G. Correlation between porosity and processing parameters in TiAl6V4 produced by selective laser melting. Mater Des 2016;105:160–70.
[263] Yusuf SM, Chen YF, Boardman R, Yang SF, Gao N. Investigation on porosity and microhardness of 316L stainless steel fabricated by selective laser melting. Metals 2017;7.
[264] Cunningham R, Narra SP, Ozturk T, Beuth J, Rollett AD. Evaluating the effect of processing parameters on porosity in electron beam melted Ti-6Al-4V via synchrotron X-ray microtomography. JOM-US 2016;68:765–71.
[265] Tammas-Williams S, Withers PJ, Todd I, Prangnell PB. The influence of porosity on fatigue crack initiation in additively manufactured titanium components. Sci Rep 2017;7:7308.
[266] Carlton HD, Haboub A, Gallegos GF, Parkinson DY, MacDowell AA. Damage evolution and failure mechanisms in additively manufactured stainless steel. Mater Sci Eng, A 2016;651:406–14.
[267] Hirsch M, Catchpole-Smith S, Patel R, Marrow P, Li W, Tuck C, et al. Meso-scale defect evaluation of selective laser melting using spatially resolved acoustic spectroscopy. Proc Roy Soc A: Math Phys Eng Sci 2017;473.
[268] Özel T, Altay A, Donmez A, Leach R. Surface topography investigations on nickel alloy 625 fabricated via laser powder bed fusion. Int J Adv Manuf Technol 2018;94:4451–8.
[269] Nicola S, Adam T, Richard L. Feature-based characterisation of signature topography in laser powder bed fusion of metals. Meas Sci Technol 2018;29:045009.

[270] Damon J, Dietrich S, Vollert F, Gibmeier J, Schulze V. Process dependent porosity and the influence of shot peening on porosity morphology regarding selective laser melted AlSi10Mg parts. Addit Manuf 2018;20:77–89.
[271] Cunningham R, Nicolas A, Madsen J, Fodran E, Anagnostou E, Sangid MD, et al. Analyzing the effects of powder and post-processing on porosity and properties of electron beam melted Ti-6Al-4V. Mater Res Lett 2017;5:516–25.
[272] Koutny D, Palousek D, Pantelejev L, Hoeller C, Pichler R, Tesicky L, et al. Influence of scanning strategies on processing of aluminum alloy EN AW 2618 using selective laser melting. Materials (Basel, Switzerland) 2018;11.
[273] Li XP, Wang XJ, Saunders M, Suvorova A, Zhang LC, Liu YJ, et al. A selective laser melting and solution heat treatment refined Al–12Si alloy with a controllable ultrafine eutectic microstructure and 25% tensile ductility. Acta Mater 2015;95:74–82.
[274] Aluminum: properties and physical metallurgy. Ohio: American society for metals; 1984.
[275] Uzan NE, Ramati S, Shneck R, Frage N, Yeheskel O. On the effect of shot-peening on fatigue resistance of AlSi10Mg specimens fabricated by additive manufacturing using selective laser melting (AM-SLM). Addit Manuf 2018;21:458–64.
[276] Zolotorevsky VS, Belov NA, Glazoff MV. Chapter one - alloying elements and dopants: phase diagrams. Casting aluminum alloys. Amsterdam: Elsevier; 2007. p. 1–93.
[277] Djurdjević MB, Manasijević S, Odanović Z, Dolić N. Calculation of liquidus temperature for aluminum and magnesium alloys applying method of equivalency. Adv Mater Sci Eng 2013;2013:1–8.
[278] Zhang H, Zhu H, Nie X, Yin J, Hu Z, Zeng X. Effect of Zirconium addition on crack, microstructure and mechanical behavior of selective laser melted Al-Cu-Mg alloy. Scr Mater 2017;134:6–10.
[279] Yang KV, Shi Y, Palm F, Wu X, Rometsch P. Columnar to equiaxed transition in Al-Mg(-Sc)-Zr alloys produced by selective laser melting. Scr Mater 2018;145:113–7.
[280] Dadbakhsh S, Hao L. Effect of Al alloys on selective laser melting behaviour and microstructure of in situ formed particle reinforced composites. J Alloy Compd 2012;541:328–34.
[281] Kanagarajah P, Brenne F, Niendorf T, Maier HJ. Inconel 939 processed by selective laser melting: effect of microstructure and temperature on the mechanical properties under static and cyclic loading. Mater Sci Eng, A 2013;588:188–95.
[282] Aboulkhair NT, Maskery I, Tuck C, Ashcroft I, Everitt N. Nano-hardness and microstructure of selective laser melted AlSi10Mg scan tracks. SPIE; 2015. p. 965702–7.
[283] Silbernagel C, Ashcroft I, Dickens P, Galea M. Electrical resistivity of additively manufactured AlSi10Mg for use in electric motors. Addit Manuf 2018;21:395–403.
[284] Chou R, Milligan J, Paliwal M, Brochu M. Additive manufacturing of Al-12Si alloy via pulsed selective laser melting. JOM-US 2015;67:590–6.
[285] Bai Y, Yang Y, Xiao Z, Zhang M, Wang D. Process optimization and mechanical property evolution of AlSiMg0.75 by selective laser melting. Mater Des 2018;140:257–66.
[286] Prashanth KG, Debalina B, Wang Z, Gostin PF, Gebert A, Calin M, et al. Tribological and corrosion properties of Al–12Si produced by selective laser melting. J Mater Res 2014;29:2044–54.
[287] Prashanth KG, Damodaram R, Scudino S, Wang Z, Prasad Rao K, Eckert J. Friction welding of Al–12Si parts produced by selective laser melting. Mater Des 2014;57:632–7.
[288] Gokuldoss Prashanth K, Scudino S, Eckert J. Tensile properties of Al-12Si fabricated via selective laser melting (SLM) at different temperatures. Technologies 2016;4.
[289] Xiong ZH, Liu SL, Li SF, Shi Y, Yang YF, Misra RDK. Role of melt pool boundary condition in determining the mechanical properties of selective laser melting AlSi10Mg alloy. Mater Sci Eng, A 2019;740–741:148–56.
[290] Uzan NE, Shneck R, Yeheskel O, Frage N. Fatigue of AlSi10Mg specimens fabricated by additive manufacturing selective laser melting (AM-SLM). Mater Sci Eng, A 2017;704:229–37.
[291] Fefelov AS, Merkushev AG, Chikova OA. Microstructure and mechanical properties of Al-12Si produced by selective laser melting. IOP conference series: earth and environmental science 2017;vol. 87:092011.
[292] Pozdniakov AV, Churyumov AY, Loginova IS, Daubarayte DK, Ryabov DK, Korolev VA. Microstructure and properties of novel AlSi11CuMn alloy manufactured by selective laser melting. Mater Lett 2018;225:33–6.
[293] Prashanth KG, Scudino S, Chaubey AK, Löber L, Wang P, Attar H, et al. Processing of Al–12Si–TNM composites by selective laser melting and evaluation of compressive and wear properties. J Mater Res 2015;31:55–65.
[294] Yadollahi A, Shamsaei N. Additive manufacturing of fatigue resistant materials: challenges and opportunities. Int J Fatigue 2017;98:14–31.
[295] Edwards P, Ramulu M. Fatigue performance evaluation of selective laser melted Ti–6Al–4V. Mater Sci Eng, A 2014;598:327–37.
[296] Riemer A, Leuders S, Thöne M, Richard HA, Tröster T, Niendorf T. On the fatigue crack growth behavior in 316L stainless steel manufactured by selective laser melting. Eng Fract Mech 2014;120:15–25.
[297] González R, González A, Talamantes-Silva J, Valtierra S, Mercado-Solís RD, Garza-Montes-de-Oca NF, et al. Fatigue of an aluminium cast alloy used in the manufacture of automotive engine blocks. Int J Fatigue 2013;54:118–26.
[298] Zahavi Eliahu, Torbilo V. Fatigue design - life expectancy of machine parts. CRC Press; 1996.
[299] Suresh S. Fatigue of materials. 2nd ed. Cambridge University Press; 1998.
[300] Kajima Y, Takaichi A, Nakamoto T, Kimura T, Kittikundecha N, Tsutsumi Y, et al. Effect of adding support structures for overhanging part on fatigue strength in selective laser melting. J Mech Behav Biomed Mater 2018;78:1–9.
[301] Bagherifard S, Beretta N, Monti S, Riccio M, Bandini M, Guagliano M. On the fatigue strength enhancement of additive manufactured AlSi10Mg parts by mechanical and thermal post-processing. Mater Des 2018;145:28–41.
[302] Hitzler L, Hirsch J, Schanz J, Heine B, Merkel M, Hall W, et al. Fracture toughness of selective laser melted AlSi10Mg. Proc Instit Mech Eng, Part L: J Mater: Des Appl 2017. 1464420716687337.
[303] Asgari H, Odeshi A, Hosseinkhani K, Mohammadi M. On dynamic mechanical behavior of additively manufactured AlSi10Mg_200C. Mater Lett 2018;211:187–90.
[304] Raus AA, Wahab MS, Shayfull Z, Kamarudin K, Ibrahim M. The influence of selective laser melting parameters on density and mechanical properties of AlSi10Mg. MATEC web conf 2016;vol. 78:01078.
[305] Zaretsky E, Stern A, Frage N. Dynamic response of AlSi10Mg alloy fabricated by selective laser melting. Mater Sci Eng, A 2017;688:364–70.
[306] Girelli L, Tocci M, Montesano L, Gelfi M, Pola A. Investigation of cavitation erosion resistance of AlSi10Mg alloy for additive manufacturing. Wear 2018;402–403:124–36.
[307] Yang Y, Chen Y, Zhang J, Gu X, Qin P, Dai N, et al. Improved corrosion behavior of ultrafine-grained eutectic Al-12Si alloy produced by selective laser melting. Mater Des 2018;146:239–48.
[308] Tang M. Inclusions porosity and fatigues of AlSi10Mg parts produced by selective laser melting. Carnegie Mellon University; 2017.
[309] Orlova TS, Mavlyutov AM, Bondarenko AS, Kasatkin IA, Murashkin MY, Valiev RZ. Influence of grain boundary state on electrical resistivity of ultrafine grained aluminium. Phil Mag 2016;96:2429–44.
[310] Zhao X, Song B, Fan W, Zhang Y, Shi Y. Selective laser melting of carbon/AlSi10Mg composites: microstructure, mechanical and electronical properties. J Alloy Compd 2016;665:271–81.